UNIVERSITÀ DEGLI STUDI DI PALERMO

Dottorato in Scienze Fisiche
Dipartimento di Fisica e Chimica (DiFC)
S.S.D. Astronomia e Astrofisica (FIS/05)

THE INTERACTION OF THE STELLAR HIGH ENERGY RADIATION WITH THE CIRCUMSTELLAR MEDIUM

IL DOTTORE
Daniele Locci

IL COORDINATORE
Prof. Gioacchino Massimo Palma

IL TUTOR
Prof.ssa Giuseppina Micela

CO TUTOR
Prof. Cesare Cecchi-Pestellini

CICLO XXX
2018

To my Father

Contents

Abstract

Since ancient times the human beings speculated on the possibility of the existence of other worlds similar to our home planet, the Earth. The discovery of the four largest moons of Jupiter, first seen by Galileo Galilei in January 1610, and recognized by him as satellites of Jupiter in March 1610, laid the foundations for a scientific answer to such a question. Indeed, the discovery of celestial bodies orbiting something other than Earth dealt a serious blow to the then accepted geocentric theory. About 350 years after that enormous step forward in the human knowledge, it was finally confirmed the existence of the long sought (perhaps dreamed) exoplanetary systems. In a few years the number of discovered exoplanets (as now planets orbiting other stars are called) grew rapidly, some of them similar to the Earth (at least in mass) orbiting around stars similar to the Sun, while others totally at odds with what we observe in the Solar System. In fact, the huge variety of exoplanets and their environments has been totally unexpected.

The purpose of this Thesis is to study how stellar high energy radiation affects exoplanetary atmospheres. High level of stellar high energy, X-rays and (vacuum end extreme) ultraviolet radiation may prevent planets' habitability and limit the width of the habitability zone. Such radiation may ionize a star surrounding, affecting the chemistry and thermal balance. The effects of X-rays can be wide ranging or relatively local. Soft X-rays are absorbed closer to the source than X-rays with energy greater than 1 keV. The absorption cross-section of hard X-rays are generally very small, so that such radiation may affect a whole galaxy to some extent. The product of photo-ionization is a cascade of fast photoelectrons, that in turn ionize and heat the medium through Coulomb collisions. Fast electrons may also excite the gas by means of non-thermal collisions, and thus populate high-lying rotational and vibrational levels of molecules such as e.g. H_2, enhancing their low frequency emission.

In chapter 1, I shall briefly introduce the current research on exoplanets. I shall discuss the physical and chemical properties of planetary atmospheres, the techniques to find exoplanets, and the ways to get information about their atmospheres. The chapter is completed

with a description of central stars, without whom we cannot understand the orbiting planets. The second chapter contains the description of a radiative-thermo-convective numerical code apt to the calculation of the downward and upward radiative flux at each atmospheric layer, and the temperature vertical profile. The code has been applied to the case of the rocky planet Kepler 12299b, to discuss the physical and chemical conditions conducive of liquid water at the planetary surface. Chapter 3 contains a detailed calculation of the ionization of a gaseous medium due to stellar X-rays. The stars I investigated are massive stars and pre-main sequence stars. The X-rays energy deposition is a multistep process in which primary photo-ionization is followed by a secondary electron cascade, whose energy loss events may be estimated considering all the possible energy degradation paths. The derived yields allow to determine the ionization, dissociation, excitation, and heating rates throughout the illuminated region. The secondary electron cascade is simulated by a means of a Monte Carlo method following the chain of discrete energy deposition events. This analysis provides the identification of the kind of star-forming regions in which X-rays dominate the local ionization of the gas. In the subsequent chapter, a study of the atmospheric mass loss induced by the heating of upper layers of the atmospheres of close-in planets by high energy photons is presented. Such investigation clarifies in what way and how much the high energy stellar radiation component affects the evolutionary history of the planetary mass, and to infer the currently observed mass-radius relationship of exoplanets, together with the statistical occurrence of giant planets during the early stages of star lifetimes. In chapter 5, I estimate the effects of the secondary electron cascade on the distribution of ro-vibrational levels of hydrogen molecules, deriving the infrared emission spectrum. I apply the results to the case of the extending atmosphere of the gaseous exoplanet HD 189733b. Finally, the last chapter contains a summary and the conclusions.

Chapter 1

A multitude of planets

The quest for other Earths out there in the cosmos, and in general for a new, less lonely vision of the Universe has been frequently raised during the human history. No answer has been possible to such a question until about the mid 1990s, when the first planets were found around nearby stars (e.g. Wolszczan & Frail 1992). Since then, the science of exoplanets advanced enormously with the discovery of thousands of planets, just looking at a very tiny fraction of our Galaxy. More importantly, we are going closer and closer to understand the composition of exoplanets' atmospheres, trying to learn how to unveil signs of life buried beneath the faint signals that reach our telescopes.

The purpose of this Thesis is to study how the high energy radiation affects exoplanetary atmospheres. High level of stellar high energy radiation may prevent planets' habitability and limit the width of the habitability zone. In the following sections of this first Chapter, I shall briefly discuss the techniques to search exoplanets, and discuss the current knowledge about their atmospheres.

1.1 Searching exoplanets

The number of exoplanets discovered and confirmed to date (november 2017) is about 3600 (Figure 1.1). The most surprising evidence is their huge variety. In the Solar System we have gaseous giants like Jupiter or Saturn, and much smaller rocky planets like Venus or Earth. Exosystems may show planets with masses up to ten times the mass of Jupiter. These giant planets may orbit so close to their host stars, and heated to very high temperatures to deserve the name of *hot Jupiters*. Typically their temperatures reach 3000 K (Crossfield

2015), similar to the temperatures of late M stars. The hottest known planet, Kelt-9b has a temperature of 4600 K (Gaudi et al. 2017). Such discoveries have changed our ideas about planet formation, as the extreme vicinity of a hot planet to the parent stars was totally unexpected.

Another class of exoplanets that doesn't have a counterpart in the Solar System is the one of *Super-Earths*, rocky planets with masses ranging from one mass to ten times the mass of the Earth. Furthermore, we expect also a huge variety of planets' chemical composition of both the atmosphere and the interiors. If you can imagine a kind of planet, as long as it falls under the laws of physics and chemistry, will probably exist out there (Seager 2009). Figure 1.1 evidences the continuity in the planetary and orbital parameters. Although it might seem that there are more planets with high mass and close to the host star than planets with low mass and far from the star, this is due to measurements biases introduced by the limits of our current techniques and instrumentation. In fact the most efficient methods for the detection of exoplanets, radial velocity and transit methods, are biased towards giant planets with orbits typically smaller than 5 AU: up to now, only 87 exoplanets have been found to orbit at distances greater than 5 AU, and among these only 24 planets have been detected through the radial velocity method (Bozza et al. 2016). Furthermore numerical simulations of planet occurrence around stars suggest (e.g. Fressin et al. 2013) that small planet are more frequent than gaseous giants.

The most important methods to search for exoplanets are based on measurements of radial velocity, transits, microlensing, and direct imaging (see Figure 1.2). The radial velocity technique measures the star motion and its tiny deviations as the planet and the star orbit around their common center of mass. When the star is moving away from us, its light is redshifted, while is blueshifted in the opposite case. Typically, such a technique is sensitive to high mass planets close to the host stars. The outcome of such measurements is the minimum mass of the planet derived by the projection $\mathrm{m} \cdot \sin(\mathrm{i})$, i being the inclination of the orbital plane on respect the line of sight. The radius, and thus the density remain unknown. In order to discover exoplanets we need high resolution and high stability. The spectrograph HARPS, installed on the ESO 3.6 m Telescope (La Silla, Chile) and its twin HARPS-N located at the Telescopio Nazionale Galileo (La Palma, Spain.) are ground-based facilities able to measure radial velocities with an accuracy of 1 m s^{-1}. This means that they can detect a planet like Jupiter orbiting around a star like the Sun at a distance of 5 AU (1 AU $= 1.5 \times 10^{11}$ m), causing star radial velocity perturbations of ~ 12.5 m s^{-1}. The Earth, orbiting at the distance of 1 AU from the Sun is still out of reach of such measurements,

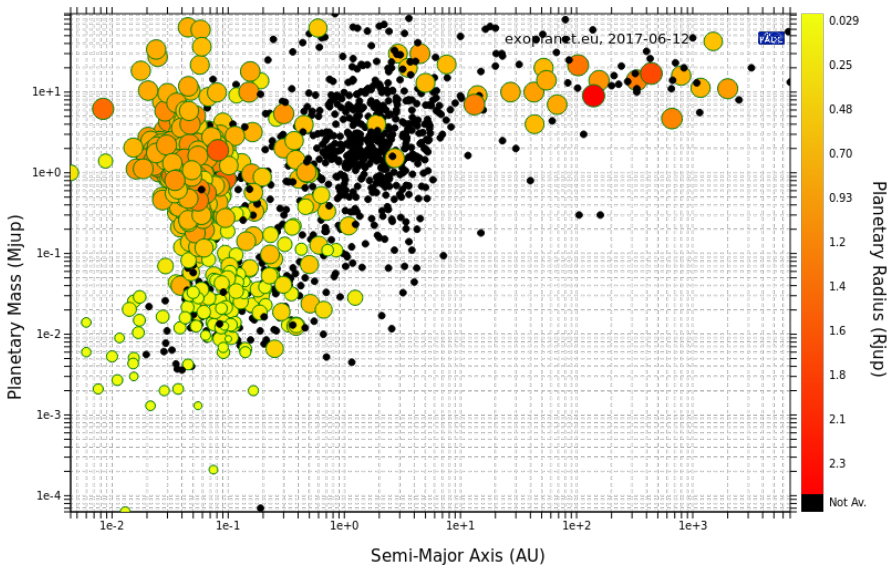

Figure 1.1: Planetary masses against orbital semi major-axes. Sizes and colors of the full circles are related to the dimensions of planets they represent. Reproduced from exoplanet.eu.

because the produced perturbations are less than 0.1 m s^{-1}. Moving the planet closer to the star, e.g. to 0.05 AU, velocity alterations increase to $\sim$ 1 m s^{-1} (Bozza et al. 2016). Among the various sources of error that can perturb radial velocity measurements (e.g. intermediate medium or instrumental errors), one of the most important is the noise due to the atmospheric phenomena of the host star. These phenomena include: pulsations, granulation noise and activity. The activity is one of the major sources of noise and for solar-like stars can produce parasitic signals in the time scale of the months and years with amplitude in the order of several m s^{-1} (Pepe & Lovis 2008) hiding planetary signals. Using this method Mayor & Queloz (1995) discovered the first exoplanet orbiting around a main sequence star.

The technique of transits consists in the measurement of the decrease of the stellar brightness due to the transit of an orbiting planet intercepting the line of sight. This is the so called primary eclipse; when the planet goes behind the star we have the secondary eclipse. Also the secondary eclipse produces a smaller decrease on the brightness, since we lose the planet's emission. From the decrease of the brightness during the primary eclipse, it is possible to infer the planet's size, but not its mass. Large planets are of course easier to detect, as well as those close to their parent stars, as the probability of transit increases with decreasing star-planet distance. The Kepler mission specifically designed for transits has

produced to date the largest number of planetary detections. It is important to notice that during the primary transit, part of the light of the star may pass through the atmosphere of the planet (see § 1.4), allowing (at least in principle) to detect its chemical composition.

The microlensing technique is based on the concept of gravitational lens. When a massive object in the foreground passes through the line of sight to some background source it tends to bend the light of such source, creating a magnified image. When the object in the background is a bright star and the one in the foreground is a star with a companion (e.g. a planet), the relative motion between the three object induces variations in the magnified light of the star in the background, allowing to infer the existence of the companion, the ratio of masses of the star and the companion and the angular separation (Brown 2014).

Direct imaging consists literally on taking a picture of the planet. Since a star can be billion times more bright than a planet, not surprisingly the major effort in such a technique must be posed in trying to block the light of the star. For instance the Earth seen from 10 parsec (1 parsec = 3.085×10^{16} m) is 10 billion of times less bright of the Sun in the visible band, and is "only" 10 millions of times less bright in the infrared band. In 1939 B. Lyot, in order to study the solar corona, invented the coronograph, a device that allows to block the sun light. Ground-based telescope using modern coronographs and adaptive optics (that allow to eliminate the interferences due atmosphere of the Earth) are able to detect exoplanets through direct imaging. With this technique it is possible to retrieve information about all components of a planetary system, orbital parameters and even the architecture of the system. We can also obtain information about the spectrum of the light, and thus infer properties of the atmosphere. The method of direct imaging is more effective in detecting bright planets far from their host star. Young planets are easier to detect because they are more luminous in the infrared band than older planets.

1.2 Formation and evolution of planetary atmospheres

The wide variety of exoplanets does not regard solely their radii or masses, but also the chemical composition of their atmospheres. Gaseous giant planets have typically a primitive atmosphere; thanks to their high mass they may retain their primordial atmosphere similar in composition to the parent nebula and disk. Therefore, giant planet atmospheres are close in composition to their host stars, i.e. dominated by H and He. Rocky planets follow different, more complicated evolutionary paths, whose understanding requires to follow the multiplicity of sources and sinks contributing to their formation (Lammer 2013). There are

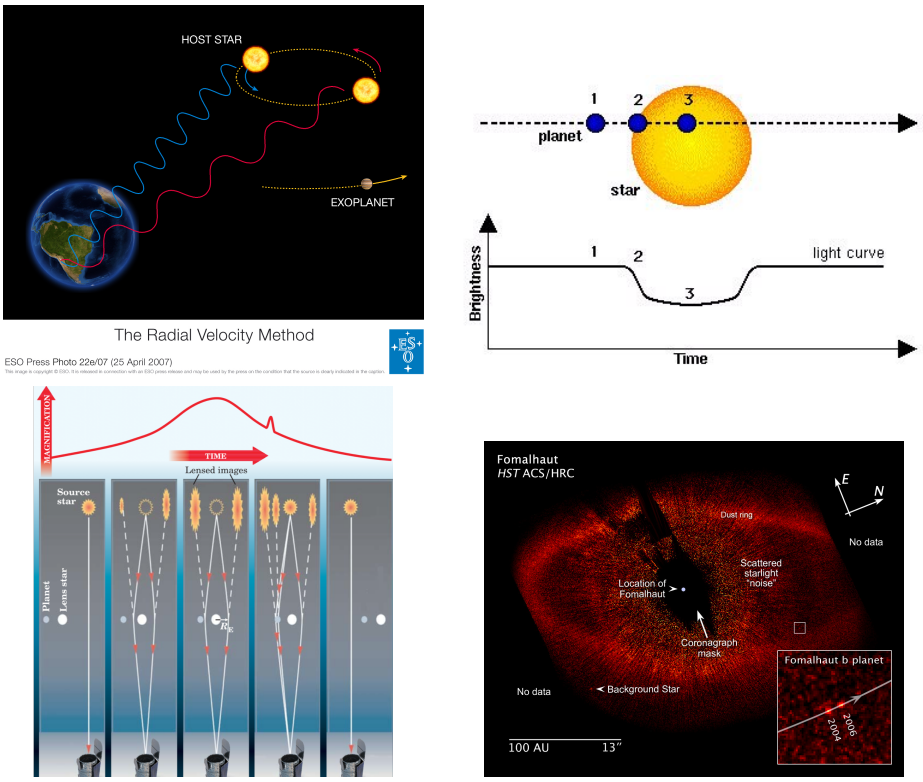

Figure 1.2: Schematic representation of the main techniques exploited in searching exoplanets. Top left panel: radial velocity; top right panel: transits; bottom left planet: micro-lensing; bottom right panel: a picture of the system Fomalhaut obtained by means the direct imaging (Kalas et al. 2009); the dark shadows is due to the coronograph.

three main channels through which they develop their early atmosphere:

- *Nebular gas and proto-atmospheres:* similarly to the case of giant planets, a rocky planet accretes its atmosphere from the protoplanetary disk, having thus its atmosphere dominated by hydrogen and helium. The protoplanetary disk after few million years is dispersed by stellar winds, but planetary embryos with mass at least of $0.1\,M_\oplus$ are still able to retain a substantial amount of gas from the nebula (Forget & Leconte 2014). In the extreme case in which the planetary embryo is massive enough, and the mass of its gaseous envelope is similar to the core mass, the so called core instability occurs, through which a giant planet may form. The critical mass above which the core instability can set in is $5-20\,M_\oplus$ at $0.1-1$ AU, and $20-60\,M_\oplus$ beyond 1 AU. The fate of a planet depends on the region where it forms, and on the mass of its

core. Under tsuitable conditions also Super-Earths can accrete an envelope dominated by H and He. Owen & Mohanty (2016) have recently argued that rocky planets form mainly with this kind atmosphere, that may be subsequently lost through atmospheric escape. The discovery of Kepler 11f (Lissauer et al. 2011), a low density Super-Earth (with mass $2 - 3\,M_{\oplus}$ supports this scenario. However, the capture of gases from the stellar nebula is a complex process that depends on various factors such as e.g. the time dispersion of the disk, and the protoplanet location in the disk.

- *Catastrophically outgassed H_2O/CO_2 atmospheres:* another source of volatiles for planetary atmospheres are planetesimals that accrete onto the protoplanet. These can be the major source of carbon compounds like CO_2, H_2O and in smaller quantities of N_2 and NH_3. The amount of water accreted depends on the disk region in which planet formed, if it located within or beyond the water snow line, i.e distance from the central star in a protoplanetary disk beyond which water molecules start to condense into ice grains. Beyond the snow line, planets can accrete a great quantity of water. In the early stage of the planet formation the energy produced by the impact of planetesimal is high enough to melt the outer mantle creating the so called *magma ocean*. In this phase the fraction of volatiles that cannot be trapped in the solid phase will be outgassed. The mass and the composition of the resulting atmosphere depend thus on the initial location in the protoplanetary disk and on composition of planetesimals and the metallicity of the parent star. The Earth for instance formed inside the snow line, therefore the amount of water available was low. Elkins-Tanton & Seager (2008) showed us that starting from different compositions of meteorites that compose the bulk of the planets, we can obtain different atmospheric compositions due to the degassing of hydrogen, water, and carbon compounds. Subsequently physical processes as atmospheric escape, chemistry and photochemistry determine the final composition of the atmosphere.

- *Volcanically degassed secondary atmospheres:* this process acts on every rocky planet, leading to the formation of secondary atmospheres. In geological times, the gase trapped in the planet mantle during the solidification phase are re-emitted into the atmosphere by volcanoes. Volcano activity produces H_2O and CO_2, other trace gases such as H_2S, SO_2, CH_4, NH_3, HF, H_2, CO, and noble gases (e.g. Ar and Xe). On Earth and Mars there are strong evidences that this process took place. In particular Mars presents a CO_2 dominated atmosphere, that is believed to be due to such scenario,

while the original planetary content of CO_2 was lost through atmospheric escape as a consequence of intense ultraviolet irradiation from the young Sun.

In general, we expect the atmosphere of an exoplanet to be due to a combination of the three scenarios described above, see Forget & Leconte (2014) and Lammer (2013) and references therein. The three scenarios are depicted schematically in Figure 1.3.

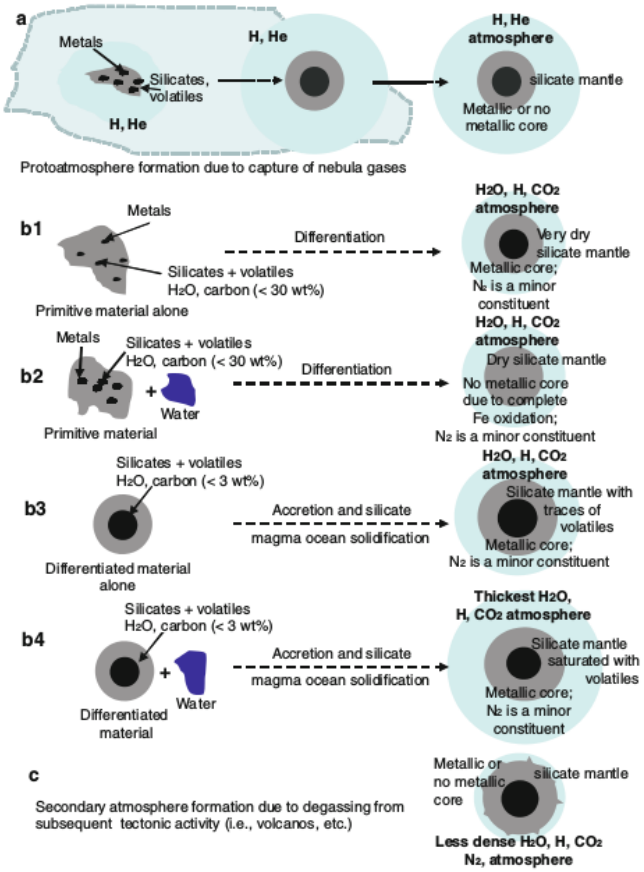

Figure 1.3: Schematically representation of the three atmosphere formation scenarios described in the text. **a**: the planet accretes its atmosphere directly from the star nebula; **b**: various possibilities for the case of catastrophically outgassed atmospheres: **b1** and **b2**: scenarios in which the gas of the nebula accretes and reacts with the primordial chondrites (undifferentiated material mainly composed of silicates with a matrix of small metals granules) and with primordial chondrites with additional delivered water respectively; **b3** and **b4** same as in b1 and b2, but with accretion on achondrites (differentiated material) poor and rich in water; **c**: a secondary atmosphere formed by volcanic outgassing. The picture is reproduced from Lammer (2013).

Until now I discussed how a planet may accrete its atmosphere. In the following, I shall briefly discuss about processes through which a planet can lose (at least in part) its envelope. The atmospheric escape typically refers to the loss of light elements from a planetary atmosphere, particularly during the early stages of their evolutionary history. In some cases, heavier elements may be involved. This can occur e.g. in terrestrial exoplanet orbiting very close to the parent star (Seager 2010). Basically, a molecule escapes from a planet when its velocity exceeds the escape velocity for the system. This typically occurs at the exobase, where molecular mean free paths are longer than the scale height of the atmosphere. At higher densities, deeper into the atmosphere, collisions prevents the escape. The atmospheric escape may be categorized into three main classes: thermal hydrostatic escape, thermal hydrodynamic escape and non-thermal escape. Photochemistry plays a key role in the thermal hydrostatic escape. Ultraviolet radiation and X-rays (hereafter called XUV radiation) ionize compounds of hydrogen, such as e.g. H_2 or H_2S. This process is more efficient in the early stages of planetary formation, when stars are young and more intense emitters of ionizing radiation. Although, hydrogen in the atmosphere is lost principally through atmospheric oxidation, a small fraction located in the exobase with velocities that lie in the tail of the Maxwell distribution will escape from the atmosphere. Such a process is frequently called *Jeans escape*, which effects particularly light elements as H and He. The thermal hydrodynamic escape corresponds to the blow-off regime in which the atmosphere exhibits an adiabatic expansion in response to radiative heating. In such a case the bulk of the particles in the thermosphere is lost (Lammer 2013). For this to occur extremely intense XUV irradiation is needed. Again, this process is favored during the early stages of planetary lives. In the blow-off regime heavy elements such as C, N and O can be transported outwards by the escaping flux of hydrogen and helium. Finally, non-thermal escape is due to energetic chemical reactions or interaction with the stellar winds (e.g. planetary pick-up, in this case atoms are ionized and accelerated by electric fields within the stellar winds). Typically collisional process enable the escape of heavier elements that hardly reach the velocity for the thermal escape (Seager 2010).

Another source of atmospheric sink is *weathering*. Under the right conditions some atmospheric constituent can chemically react with the rocky surface of the planet remaining trapped there. During geological times, such elements can be incorporated into the planetary mantle through subduction of the plate tectonics or through flows of lava. Subsequently this volatiles can be outgassed into the atmosphere by the volcanic activity. On the Earth, chemical weathering of the CO_2 is followed by the incorporation of CO_2 into liquid solution,

whose products, carbonic acid, reacts with the mineral silicate of the crust. This gives rise to the carbonate-silicate cycle

$$\mathrm{CaSiO_3(s) + CO_2(g) \rightleftarrows CaCO_3(s) + SiO_2(s).} \tag{1.1}$$

Another important factor in the evolution of planetary atmospheres is *migration*, during the early stages the planetary system, in fact tidal interactions between the planet and the protoplanetary disk can induce the phenomena of migration (e.g. see Kley & Nelson 2012). The first evident possible effect is the accretion of new material during the migration, for instance through pebble accretion that can modify atmospheric C/H, O/H and C/O ratios (Madhusudhan et al. 2017). Bruno et al. (2017) analyzed the atmospheres of two hot Jupiters, HAT-P-38b and WASP-67b, orbiting similar stars with similar periods. Nevertheless, the two planets have two very different atmospheres, with one covered by dense layers of clouds (WASP-67b), and the other one (HAT-P-38b) basically cloud free.

1.3 Types of planetary atmospheres

In the following I will discuss briefly the (expected) types of atmosphere, in light of the previous discussion. First of all we have solar-like atmospheres, typical in massive planets. In our Solar System in fact, only gaseous giant have retained the H and the He accreted from the original solar nebula. However it is thought that a mass of $2M_\oplus$, with the right conditions, is sufficient to retain a primitive envelope. A further kind of atmospheres are those dominated by $H_2O/CO_2/N_2$. These atmospheres form if the planet lose its primordial H and He envelope through the escape, while the temperatures are low enough to freeze the surface releasing H_2O and CO_2. In hot planets *runaway greenhouse* can occur, in which all the water content is vaporized into the atmosphere. In such a case H_2O may become the major constituent of the atmosphere. However for heavy irradiation water can be easily photodissociated producing atoms of H that can eventually escape, if the planet is not too massive. In this condition the absence of liquid water prevents the weathering of CO_2 that now can become the dominant element of the atmosphere. This may have been experienced by Venus in the Solar System. If runaway greenhouse is prevented water condenses on the surface, enhancing CO_2 weathering, Thus, element such as N_2 that initially was barely outgassed can now become the dominant constituent. If the planet has a low mass water may instead escape, and the final atmosphere will be dominated by CO_2 (e.g. Mars). However,

in cold planet CO_2 condense, leaving N_2 as the only stable species in the inventory of the atmosphere (Forget & Leconte 2014).

Molecular oxygen is a very reactive molecule. In the Earth atmosphere it is continually produced by life through photosynthetic processes. However, a early very moist atmosphere can lose H through photodissociation of water and hydrogen escape resulting in an abiotic O_2 dominate atmosphere. Alternatively in a very dry atmosphere O_2 can be a product of CO_2. We can finally expect also a thin silicate atmosphere. Such atmospheres can form in exotic environments, for instance in planets very close to the parent stars, that for some reason have lost volatiles elements, In this case the surface of the day side can reach temperatures sufficient to melt the crust releasing refractory element as Na, K, O_2, and SiO to form a thin silicate atmosphere (Forget & Leconte 2014).

If we detect an exoplanet through both transit radial velocity methods, we may measure the radius and mass, and thus the density. Starting from these data it is possible to (try to) infer the bulk composition of a planet. Rogers & Seager (2010) starting from different bulk compositions posed constrains on the possible atmosphere of the Super-Earth GJ 1214b ($M_p = 6.55 \pm 0.98\, M_\oplus$, $R_p = 2.678 \pm 0.13\, R_\oplus$). In Figure 1.4 we can see some of their results for a given density of the planet, and thermal structure of the atmosphere. The three axis represent the mass fraction of constituents of the core of the planet, of the mantle, and the mass fraction of the envelope components. The left side panel of Figure 1.4 illustrates the scenario in which the planet bulk incorporates an iron core, a silicate ($Mg_{0.9}Fe_{0.1}SiO_3$) mantle, and a water ice layer, while the gaseous envelope has solar composition. The core and the mantle are combined together into a single axis. In the right side panel is illustrated a scenario with an iron core, a silicate mantle and a vapor water dominated atmosphere. The gray shaded area represents the compositional mixtures that are consistent with the fiducial values for the mass and the radius; the red, yellow, and blue shaded areas denote compositions that are consistent within 1σ, 2σ and 3σ observational uncertainties respectively. It is evident that is impossible to infer a unique composition of atmosphere and the bulk knowing only radius, mass, and stellar irradiation. In the case of the solar-like composition (H + He), for any value of the mass fraction of the envelope it is possible to find a combination of the values of the mass fraction of the iron core and the silicate mantle that is consistent with the inferred density of the planet. On the contrary, when the atmosphere is composed of (mainly) water vapor, considering the uncertainties, for the mass of the water envelope, only with values lower than 60% of the total mass of the planet it is possible to obtain a combination of the values for the mass core and the mass mantle consistent with

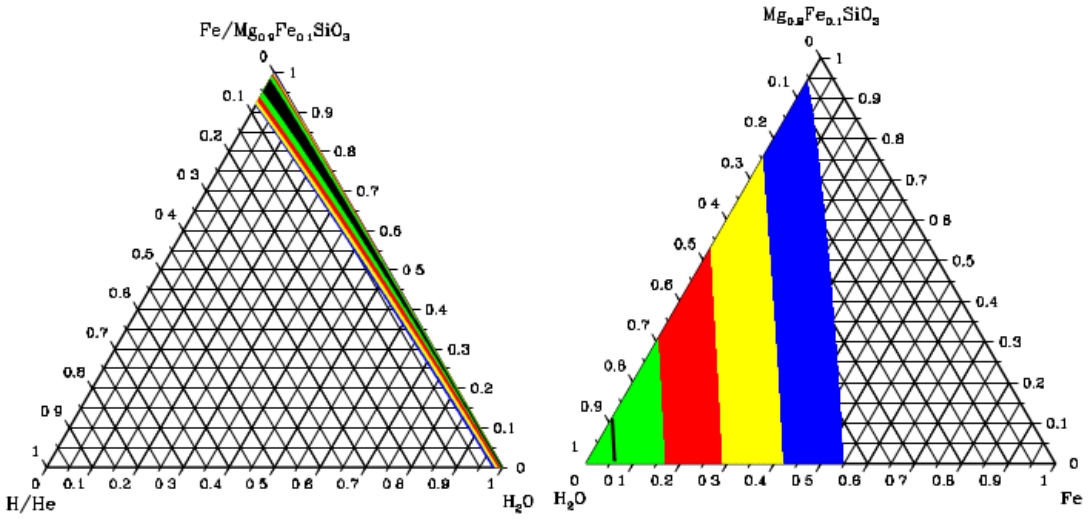

Figure 1.4: Ternary diagrams for two different combinations of both bulk and atmospheric compositions. For given radius, mass and thermal structure of the atmosphere, the diagrams show the effects of different proportions of mass fractions of the core, the mantle, and of the atmosphere. Such combinations are consistent with densities inferred for the planet. Left panel: The three axes represent the mass fraction of iron core and the silicate mantle combined together in a single axis, the mass fraction of a water ice layer, and third axis represent the mas fraction of the H/He dominated envelope; right panel: the three axes are the mass fraction of the iron core, the mass fraction of the silicate mantle an the mass fraction of the water vapor dominated atmosphere, respectively. The gray shaded area indicates the compositional mixtures consistent with the fiducial values for the mass and the radius; the red, yellow, and blue areas denote compositions consistent within 1σ, 2σ and 3σ observational uncertainties, respectively. The green area is the plausible interior compositions if a certain range of atmospheric parameter values are considered. The figure is reproduced from the work of (Rogers & Seager 2010).

the inferred density.

1.4 Observed atmospheres

In parallel with the advances in the techniques to detect exoplanets, in the last decade also techniques to observe and analyze planetary atmospheres have showed a substantial improvement. As I saw at the end of last section it is virtually impossible to retrieve uniquely the composition starting only from measures of mass and radius. The characterization of the atmosphere is the only way to get information on thermal structures, physical and chemical processes (equilibrium and non-equilibrium shuch as eddy and molecular diffusion and

photochemistry), presence or absence of thermal inversion, dynamics etc. (Crossfield 2015, Madhusudhan et al. 2014). Currently, the most effective methods to observe atmospheres and extract the necessary data for their characterization are:

- *Transits and eclipses:* The method of transits for the detection of exoplanets has been discussed In § 1.1. During the primary transit the star light passes through an atmospheric annulus (see Figure 1.5), whose opacity is wavelength dependent. Thus, observing at different wavelengths we can obtain different values for the planet size, with the radius appearing greater at wavelengths where the atmosphere is opaque. Measuring the wavelength dependent transit depth, $[R_P(\lambda)/R_\star]^2$, where R_P and $R_\star$ are the radii of the planet and the star respectively, we obtain the so called transmission spectrum (Crossfield 2015). In this spectrum, features have typically amplitudes proportional to $H \times R_P/R_\star^2$, where $H = k_B T/\mu g$ is the scale height, with k_B the Boltzmann's constant, T the temperature, μ the mean molecular weight, and g the surface gravity. As a consequence the amplitude of the signal depend also on the composition of the atmosphere through μ. This means that we can get information about chemical composition of the atmosphere thanks to the transmission spectrum. For example, observing hot Jupiters at the visible wavelengths, we can see the absorption features of Na and K, while in the infrared H_2O, CH_4, CO and CO_2 dominate the opacity. With this technique we can also infer the presence of high altitude clouds or hazes that mask the absorption features, acting as a gray opacity, flattening the spectrum, and ultimately revealing their presence (Madhusudhan et al. 2014, Heng & Showman 2015). When planets orbit around active stars, the presence of spots on the stellar surface can cause wavelength dependent variations in the transit depth.

  During secondary eclipses, we can observe and characterize thermal emission spectra through the measurement of the wavelength dependent decrease of the flux when the planet passes behind the star. At longer wavelength the emission spectrum is dominated by the thermal emission of the planet, whereas at shorter wavelength the spectrum also contain a contribution due to the scattered light depending on the planetary albedo. While the transmission spectrum allows us to characterize the part of the atmosphere near to the day night terminator, the emission spectrum allows us to study the day side of the planet, since just after (or before) the secondary eclipse the day side is facing the detectors. In addition to information about the chemical composition of the atmosphere the emission spectra may also provide hints on the thermal

structure.

Currently, observations of reflection spectra are extremely challenging since in the visible light the planet-star contrast ratio is much smaller than the case of infrared light. In Figure 1.5 we can see a "new version" of the more famous *pale blue dot* picture, showing the Earth seen from Saturn at 10 AU distance. The typical blue color, as in the case of the daylight, is due to the reflection of light by Rayleigh scattering. In transmission measurements our planet appears as *pale red dot* (Pallé et al. 2009), since in this case the optical path of the light inside the atmosphere in much greater and thus the short wavelengths are scattered away and we can see only the longer wavelengths, similar to what happens at the sunset.

- *Phase curves:* such kind of observations are complementary to emission measurements, that provide information only on the day side just after or before the ingress or the egress. Phase curves observations records the emission or the reflected spectrum at different orbital phases (Figure 1.5). For its nature this kind of observations contain information about the flux atmosphere convolved with the geometric projection to the observer. By deconvolving the phase curves we can get a longitudinal 1D map of brightness. In the special case in which the orbital plane of the star and the planet do not coincide, it is possible to retrieve latitudinal information about the atmosphere through high-cadence measurements, before and after the secondary eclipse, building now a 2D brightness map. Furthermore, measurements at different wavelengths provide informations relative to individual atmospheric layers, opening the way to 3D maps. Due to the instrumental biases, many of transit exoplanets found so far, are so close to their host stars that they are tidally locked, i.e. their orbital period is the same as the revolution period. In that case, as for the Moon always facing the same face to our planet, they show constantly the same face to the star. Therefore, the amplitude of the phase curve spectrum at the infrared wavelengths provides the night day temperature contrast. In absence of strong winds in the atmosphere, the hottest point is near to the sub-stellar point, and the coldest point is near to the anti sub-stellar point. As a consequence, if in the longitudinal maps the hottest point does not coincide with the sub-stellar point, we may infer that the atmospheric circulation redistributes efficiently the heat. On the contrary, if the sub-stellar point and the hottest point in the map coincide, then we can expect that strong winds are absent. Phase curve measurements provide more information than observations of secondary eclipse, but they require

much more observational time. These kind of measurements require very high signal to noise ratio.

- *High-Dispersion Spectroscopy:* this recent technique allows to obtain emission spectra for non-transiting planets through the measurement of high resolution ($\lambda/\Delta\lambda \geq 30,000$) near-infrared spectra, thanks to large effective area that can be achieved with large ground-based telescopes. In order to overcome the low signal-to-noise ratios this technique performs a cross-correlation between the measured spectrum and a theoretical template of a specific molecule that allows to determine or to exclude the presence of the molecule detecting the RV-shifted feature on the planet emission spectrum. The method provides tight constrains on the presence of molecules such CO or H_2O for some planet (see e.g. Brogi et al. 2014; Snellen et al. 2010).

For more details about these techniques for the characterization of atmospheres interested readers may refer to the works of Crossfield (2015), Madhusudhan et al. (2014), and Heng & Showman (2015) and (references therein).

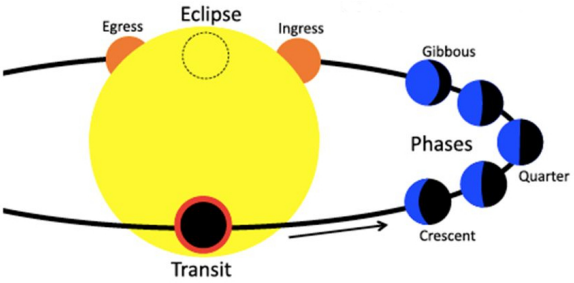

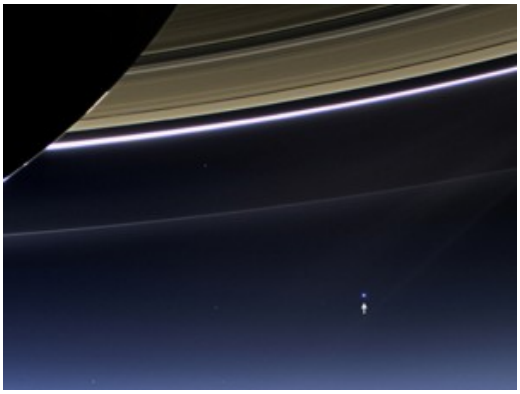

Figure 1.5: Left panel: primary and secondary transits: during the primary eclipse the light passes through the red annulus (atmosphere) generating the transmission spectrum; during the secondary eclipse, the ingress and the egress provide the emission and reflection spectra. The phases of the orbit are also showed, from them we can obtain emission spectra and create a 1D longitudinal map of temperatures. Right panel: "new" pale blue dot taken on July 2013 by the NASA's Cassini spacecraft from Saturn (visible in the image), at about 10 AU. The Earth is indicated by the arrow. The original picture of the pale blue dot was taken by Voyager spacecraft in the 1990 following an idea by Carl Sagan.

1.5 Modeling atmospheres

To get information on physical or chemical conditions within a planetary atmosphere from atmospheric spectra we need to incorporate in the retrieval technique a forward model. Last decade marked significant progress in the modeling techniques of planetary atmospheres and in the interpretation of their spectra. Models deal with a wide parameter space: sizes, particular locations in a system, variety in the composition of both bulk and atmosphere, and so on. The complexity of the models run from one-dimensional (1D) plane-parallel models to three-dimensional (3D) General Circulations Models (GCMs) (Madhusudhan et al. 2014). 1D models are able to provide global averaged quantities such as the temperature and chemical profiles. These models are useful to explore the range of possible climate, but are inadequate for instance to simulate the radiative impact of clouds or the local conditions at a given time. The later models instead are able to simulate the atmospheric dynamics and in principle the transport of energy by oceans (see §2.1). GCMs are particular useful for the interpretations of longitudinal maps of brightness derived by phase curve observations.

Plane parallel 1D models first of all solve the radiative transfer problem for the stellar radiation and the reprocessed thermal radiation. These models take into account different phenomena such as: the vertical transport of energy due to small scale turbulence and convection, the storage and exchange of heat with the surface, the change of phase of volatiles at the surface and into the atmosphere. 1D models can handle the chemical and photochemical processes that modify the composition of an atmosphere, that in turn it affects e.g. the vertical profiles of pressure and temperature ($P-T$ profile). In Figure 1.6 a schematic representation of the various process occurring within an atmosphere is showed.

Some kind of models generally work under assumption of radiative-convective equilibrium, hydrostatic equilibrium, chemical equilibrium, and local thermodynamic equilibrium (LTE). The first assumption allows the determination of the $P-T$ profile; the second relates the level pressure with the radial distance from the surface of the planet; finally, the third allows to constrain the elemental abundances that are the source of the opacity. With these assumptions the models can simulate atmospheres in which dynamical and non-equilibrium processes do not affect significantly the thermal and the chemical structure. Another class of models, called *parametric*, as the former ones, deal with the problem of the radiative transfer in a plane-parallel atmosphere under the assumption of hydrostatic equilibrium and LTE, but now $P-T$ profile and chemical abundances are free parameters in the computation.

3D models consist in a hydrodynamic core solving Navier-Stokes equations in order to

simulate large scale circulation induced by longitudinal or latitudinal gradients of temperature. They are able to deal large scale circulation induced by longitudinal or latitudinal gradients of temperature. Chemistry is generally solved using either equilibrium or kinetic approaches, the latter relying on extended reaction networks, which are frequently based on empirical estimates because of the lack of quantum calculations and laboratory experiments.

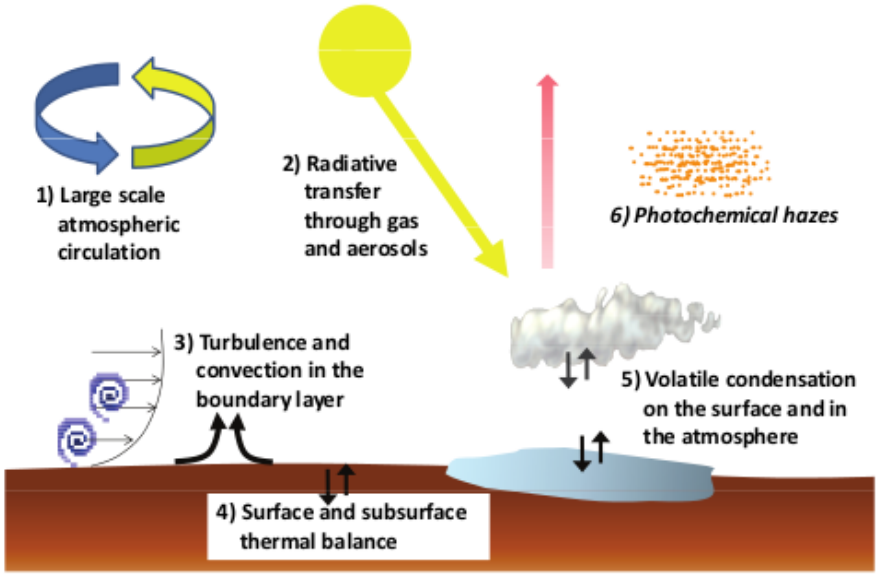

Figure 1.6: Schematic representation of the main processes at work within an atmosphere (reproduced from Forget & Leconte 2014).

1.6 Chemistry

In the former sections I discussed the physical processes that affect the elemental composition of planetary atmospheres, the techniques for observations and numerical models apt to the characterization of atmospheres. The abundance of elements in an atmosphere is governed by chemistry, and depends mainly on temperature and pressure gradients (Seager 2010). Chemical models may assume chemical equilibrium studying also departures from it. To investigate the chemical equilibrium some authors use the criterion of the minimization of the Gibbs free energy at a given pressure and temperature (Madhusudhan et al. 2014). Another approach consists in following the kinetics of the chemical system through the

resolution of the equation of continuity

$$\frac{\partial n_i(z)}{\partial t} + \frac{\partial \phi_i(z)}{\partial z} = P_i(z) - n_i(z)L_i(z) \tag{1.2}$$

where $n_i(z)$ is the number density of the species $i-$th at the altitude z, $\phi_i(z)$ is the vertical flux of particles, L_i and P_i are the loss and production rate terms of the $i-$th species. Their values depend on the local physical properties of the medium, such as temperature and pressure. The photochemical equations 1.2 are coupled through the loss and production rate terms. The number densities are also coupled at each altitude z through the flux of particles $\phi_i(z)$. Sometimes number densities can be replaced by mixing ratios.

Currently, atmospheric data are available mainly for gaseous planets, for which the most abundant elements are H and He. Assuming solar abundances (Asplund et al. 2009), the following more abundant elements are C and O with C/O ratio ~ 0.5. At the chemical equilibrium, the main carrier of oxygen is H_2O at any temperature, whereas the most important carbon bearing species are CO, CO_2 and CH_4, depending on the temperature regime (Madhusudhan et al. 2014). Moses et al. (2013) investigated how the C/O ratio affects the elemental abundances at the equilibrium (Figure 1.7). In the case of C/O = 0.5 for temperatures greater than $\sim$ 1000 K, H_2O and CO are the main carriers of O and C respectively; for lower 1000 K the main carrier of C becomes CH_4 and CO_2 increases its abundance depending on the metallicity. In the non-solar case of C/O = 1.1 there is a dramatic decrease in the water abundance, while the abundance of elements as C_2H_2 and HCN increases. At lower temperature elements as CH_4 and NH_3 are always prominent. The observations of atmospheres with C/O ratios greater than 1 are still controversial. The C/O ratio also controls the abundances of TiO and VO: C/O greater than 1 suggests a depletion of these two molecules. These molecules can be responsible for the inversion of temperature in the atmosphere of a giant planet, analogously to the mechanism shaping the ozone profile on the Earth. TiO and VO can absorb the optical light driving temperature inversions. Albeit there are not clear observation of TiO and VO, the absence of temperature inversion could indicate C/O$\geq$ 1 (Madhusudhan et al. 2014). For several hot Jupiters there is a no persuasive evidence of the thermal inversion, but this doesn't means necessarily a ratio C/O grater than 1, for instance some cold trap can act removing species Ti-bearing in the deeper atmosphere, this phenomenon removes TiO gas from the upper atmosphere, alternatively super-rotation can transport TiO gas from the hot day side to the cooler night side where Ti gas can condense into refractory grains, whereby the gas returns to the day side Ti-free

(Madhusudhan et al. 2014).

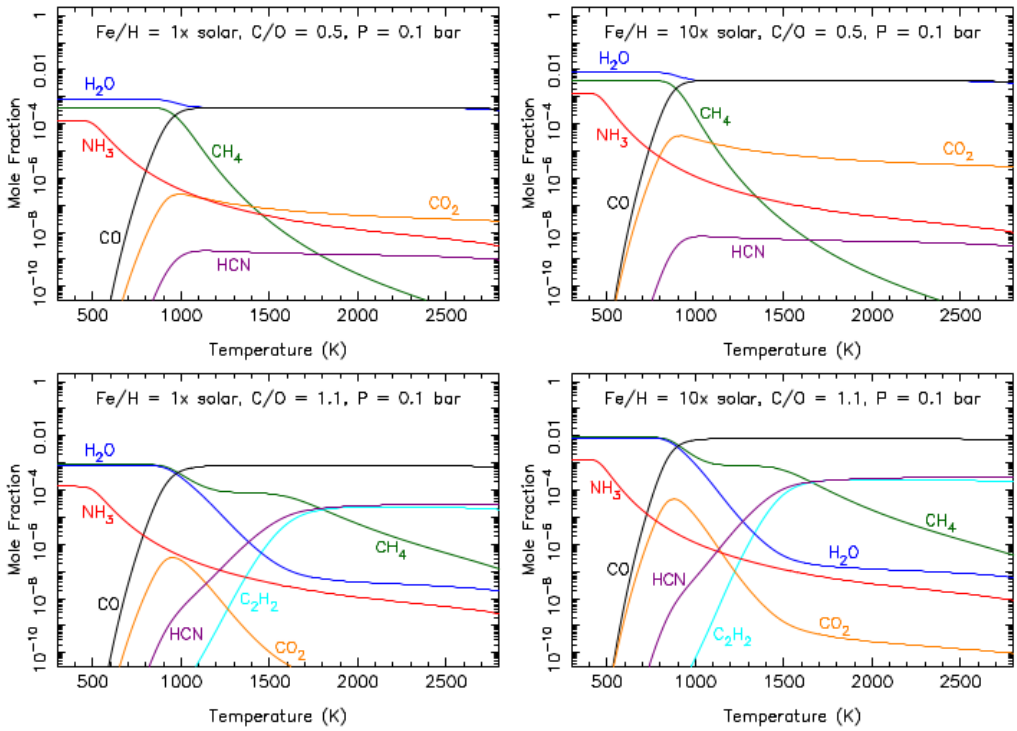

Figure 1.7: Mixing ratios of various elements as functions of the temperature. at a pressure $P = 0.1$ bar., with solar (top panels) and super solar $10\times$ (bottom panels) metallicities. Left panels: $C/O = 0.5$; right panels: $C/O = 1.1$. Reproduced from Moses et al. (2013).

Since non-equilibrium chemistry is ubiquitous in the Solar System, we expect it in action also in exosytems. However, in hot Jupiter atmospheres, where the temperature can be even higher than 3000 K, kinetic reactions are generally so fast that the system approaches rapidly chemical equilibrium. The main processes affecting chemical equilibrium are the vertical mixing of species due to either the turbulence (eddy diffusion) or molecular diffusion, and to photochemistry induced by incident stellar radiation. These processes typically become important in the upper layers of the atmosphere, where temperatures are lower and time scales of chemical reactions ($\tau_{\rm chem}$) are longer than the time scale of the vertical mixing ($\tau_{\rm mix}$). Deep into the atmosphere where $\tau_{\rm chem} < \tau_{\rm mix}$ the system has enough time to reach the chemical equilibrium, whereas the layer where $\tau_{\rm chem} = \tau_{\rm mix}$ is the so called quench level (Seager 2010), the quench level is different for each molecule.

One example of process of non-equilibrium chemistry, is the CO-CH_4 disequilibrium. In

Figure 1.7 we can see that for T $\leq$ 1300 K at the equilibrium, the principal bearing species of C is CH_4. The double bond of CO makes the conversion of CO into CH_4 slower than the reverse reaction. However, the vertical mixing removes CO molecules from the deep atmosphere, where the the condition are favourable for CO formation, and inject them into upper layers, thus perturbing chemical equilibrium. A similar process takes place for the pair N_2-NH_3 at lower temperatures. In the atmosphere of the Earth, incident high energy radiation is responsible for the presence of O_3 in the stratosphere via the photolysis of O_2.

1.7 Habitability and biosignatures

The final goal of the research on exoplanet is to find planets that can harbor life. To this aim the search must be restricted to rocky planets orbiting in the so called habitable zone (HZ) of their host star. The habitable zone is defined as the circumstellar region where a planet can have surface temperature that allows the presence of liquid water. The location of this region depend on the distance from the star, but also from the properties of the planetary atmosphere. Kopparapu et al. (2013) find for terrestrial-like planets with CO_2-H_2O-N_2 atmospheres that the HZ extends from 0.99 AU (inner edge) to 1.7 AU (outer edge). Thus, the "real" Earth appears to be very near to the inner edge of the HZ of the Sun. Since the climate of a planet depends mainly on the energy input from the star, HZs around small stars are inner than around brighter stars. However, climate depends significantly also on the composition of the atmosphere through the greenhouse effect and the albedo, e.g. the fraction of the solar radiation reflected back into the space. The first contributes to the heating of the planet, while the second one to the cooling. On the Earth, although the atmosphere is dominated by nitrogen (78%) and oxygen (21%), the main greenhouse gases are water and carbon dioxide. Since greenhouse effects produce on average an increase of temperature $\sim$ 30 K, from 258 K to 288 K, without greenhouse effect the Earth would be uninhabitable. On Venus, where the surface temperature is $\sim$ 730 K, the thick atmosphere mainly composed of CO_2 (96%) gives rise to a strong greenhouse effect that causes a temperature increase of $\sim$ 500 K. This is also due to its high albedo that in conjunction with the dense atmosphere allows only the 1% of the solar light to reach the surface of Venus. Without greenhouse effects the equilibrium temperature would be 233 K (Lacis 2012), less than the Earth one. It is thought that billions of years ago, Venus may have had liquid water on its surface. Because the high surface temperature, water evaporated, saturating the upper layers of the atmosphere, where the strong ultraviolet radiation photo-dissociated the water allowing H

to escape into the space. Furthermore, the increasing of water vapor into the atmosphere generated higher temperatures through the greenhouse mechanism, inducing a more intense evaporation. Such positive feedback, called runaway greenhouse, coupled with the escape determined the lose of planetary water content (Seager 2013). The runaway greenhouse effect is an important process in the estimate of the inner edge of the HZ, while the outer edge is controlled by the condensation of CO_2. Kopparapu et al. (2013) calculated for the Solar system an inner edge at 0.99 AU and a outer edge at 1.7 AU, (the Earth is very near to the inner boundary of the HZ of the Sun). Mars with a distance from the Sun of 1.5 AU is well inside the HZ of the Sun(see Figure 1.8). However, Mars is too small, and then it lost most of its atmosphere. Moreover, low pressures make CO_2 absorption lines narrow, producing a very weak greenhouse effect unable to sustain liquid water on the surface, with the possible exception of few sporadic seasonal episodes. This makes it clear that to find a planet into the star HZ does not automatically imply that this planet has liquid water on its surface. The Kopparapu et al. (2013) HZs can be enlarged, when considering planets with ratios ocean/land smaller than the Earth: in such cases the atmosphere will be drier than that of the Earth with a fainter greenhouse effect, so that the inner edge of the HZ moves to 0.5 AU for the Sun (Seager 2013). For the outer edge we can consider that, as discussed in § 1.2, Super-Earths can support H_2 dominated envelopes. Albeit H_2 is an homonuclear molecule (no dipole moment), at high pressure frequent collisions induce very broad absorption bands. Moreover, H_2 condense at temperatures much lower than CO_2 (tens of kelvin vs 190 K at 1 bar). For these reasons a Super-Earth with a thick H_2 dominated envelope can sustain liquid water up to 10 AU distances from a Sun-like star (Pierrehumbert & Gaidos 2011). In Figure 1.8 the *extended* HZs for different types of stars are shown.

A search for life in the Universe requires consideration of how life may be detected. This gives rise to the notion of (astronomical) biosignature, i.e. of "what constitutes evidence for life". The detection of liquid water is impossible, but water vapour can indicate the presence of liquid water on the surface making the planet potentially habitable. In the Earth the most relevant biosegnature gases are O_2 and ozone, a product of O_2 photolysis. Oxygen is produced by plants through photosynthesis and by bacteria. The detection of oxygen is not a robust biosignature since O_2 may be also produced by abiotic processes (Wordsworth & Pierrehumbert 2014). Other interesting terrestrial biomarkes are N_2O produced by microbial redox reaction, and CH_4 produced by bacteria. There are many other gases as N_2, NO, NO_2, H_2S and SO_2, that can indicate the presence of life, but also in this case they can have abiotic origins, e.g. N_2 that on Earth is the dominant species. From the above discussion it follows

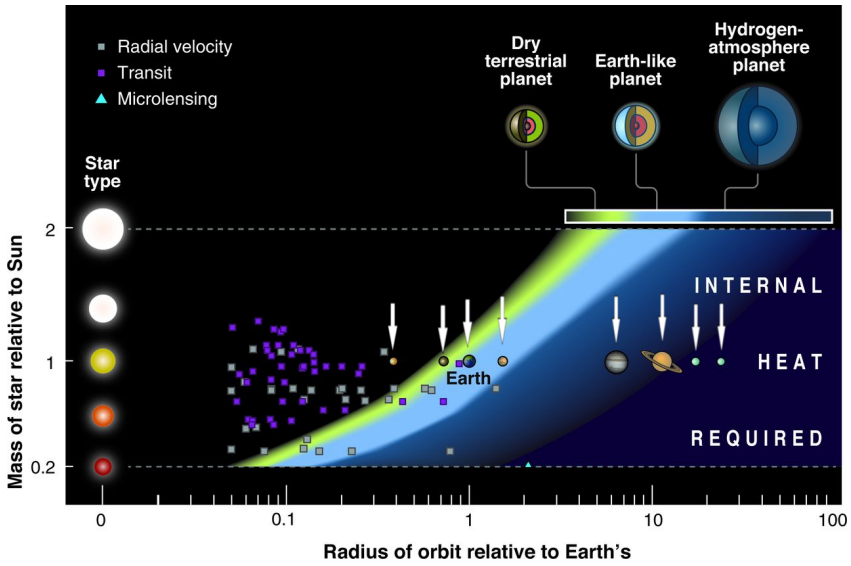

Figure 1.8: Habitable zone for stars of different spectral types. The light blue region represent the HZ for N_2-CO_2-H_2O atmospheres as calculated by Kopparapu et al. (2013), where the inner edge is determined by the runaway greenhouse effect and the outer edge by the CO_2 condensation, while yellow and dark blue regions represent the extended HZ . In the picture are also shown the planet of the solar system indicated by the arrows. Reprinted from Seager (2013).

that detection of a biosignature does not imply presence of some kind of vital processes. An interesting bio-feature, the so called *red edge* is due the to presence of the vegetation. The red edge is due to a strong increase of the albedo around 750 nm produced by the vegetation that has developed this characteristic to avoid overheating of chlorophyll. A critical point in such an approach is the validity of the extrapolation of local, terrestrial structures to alien environments.

1.8 Stars

In this section I shall briefly describe stars as central objects of stellar systems. Since this work is focused on the study of the impact of X-rays on the medium, I shall describe more in detail the behaviour of stars in the X-ray spectral band. The study and the characterization of the central star is crucial for our understanding of exoplanetary systems: if you do not know the star, you cannot understand the orbiting planets. For instance, when we detect a planet with the method of transits or through radial velocity measurements, we can infer the radius and the mass of the planet, but only if we know the radius and the mass of the

host star. Planetary climates are governed by stellar radiation, and high energy can directly influence prebiotic processes. Given an atmospheric chemical composition, stellar radiation can induce either greenhouse or anti-greenhouse effects.

Main sequence stars, i.e. stars in which the fusion of hydrogen into helium is on going, are classified depending on the properties of their spectrum. The most massive and hotter stars are the O and B stars, they are characterized by strong emission in the ultraviolet band (that is completely incompatible with the life as we know it). Because of their high masses, they have very short lifetime (from 10 to 100 millions of years) not enough to allow the establishment of vital mechanisms. Massive stars are also copious X-ray emitters, with the X-ray luminosity that run in range $10^{-4} - 10^{-7} L_{\rm X}/L_{\rm bol}$. In massive stars X-rays are produced by supersonic shocks in the stellar winds (e.g. Favata & Micela 2003). Due to their short lifetime and their high luminosity, it is very hard to find planets around these kind of stars. However a planet with mass $M =\sim 2.5 M_{\odot}$ has been found around a B star, making them as currently the most massive stars possessing orbiting planets (Carson et al. 2013). A and F stars are less massive and hot than O and B stars, having thus longer lifetimes, up to few billions of years. The theory of stellar structure predicts that an A star does not develop convective zones if its mass is higher than $\sim 1.8 M_{\odot}$ (e.g. Favata & Micela 2003). Therefore, A-type stars (more massive than F) do not present convective zones (see Table 1.1). Convective zones are a necessary ingredient to light the stellar dynamo, and thus to establish a magnetic field able to confine the stellar corona, responsible for the emission of X-rays. For this kind of stars there are several detections of planets, in particular for F stars, for instance the two A stars Fomalhaut (Kalas et al. 2009) and β Pictoris (Lagrange et al. 2009) have an exoplanet detected with the method of direct imaging.

G stars, as the Sun, can live for about 10 billions of years and are X-ray emitters, they typically show a X-ray luminosity of $L_{\rm X}/L_{\rm bol} \simeq 10^{-6}$ but since the luminosity of high energy radiation tends to drop with the time, young G stars can present an X-ray luminosity level up two order of magnitude higher. These stars in many cases host exoplanets.

The more common stars in the Galaxy are M stars and K stars, due their low mass they have very long lifetimes: they can live for few tens or hundreds of billion of years. The X-ray luminosity of K stars is similar to that of G stars, whereas the median of the emission of M star is about on order of magnitude lower than the one of K stars (Favata & Micela 2003). However M stars may be very active stars, showing very energetic periodic flares, during which the X-ray luminosity can increase up to several order of magnitude. Due to their low mass, typically the planets orbit close to the host stars, thus flares can strongly affect the

planetary atmospheres via ionization and hydrodynamic escape. In Table 1.1 some of the main physical parameters for main sequence stars are showed.

Young stellar objects (YSOs) are remarkable X-ray emitters, as their name immediately identifies these objects are in their early evolutionary stages. Since they are not burn hydrogen into helium yet, we often refer to this pre-main sequence star as T Tauri stars. These stars are fully convective and are fast rotators with a strong magnetic field. Thus, they are very active and exhibit a very strong X-ray emission in the range $L_{\rm X} = 10^{28.5} - 10^{31}$ erg s^{-1} (Feigelson & Montmerle 1999). T Tauri stars are therefore also brighter than their main sequence counterparts. For instance the young Sun in the X band is estimated to have been 3 order of magnitude more luminous than today. This high emission level persists at least 10 millions of years, a period in which protoplanetary disks are still present. Therefore, the formation and the early evolutionary stages of planets can be strongly affected by such high energy emission from the star.

Table 1.1: Physical characteristics of stellar classes.

Class	Effective temperature (K)	Mass ($M_\odot$)	Radius ($R_\odot$)	Luminosity ($L_\odot$)	X-ray Luminosity erg s^{-1}
O	$\geq$ 33000	$\geq$ 16	$\geq$ 6.6	$\geq$ 30000	$10^{30} - 10^{32}$
B	10000- 33000	2.1- 16	1.8- 6.6	25- 30000	$10^{27} - 10^{31}$
A	7500-10000	1.4-2.1	1.4- 1.8	5-25	$10^{25} - 10^{30}$
F	6000- 7500	1.04-1.4	1.15-1.4	1.5-5	$10^{27} - 10^{30}$
G	5200-6000	0.8-1.04	0.96-1.15	0.6-1.5	$10^{26} - 10^{27}$
K	3700-5200	0.45-0.8	0.7-0.96	0.08- 0.6	$10^{26} - 10^{27}$
M	$\leq$ 3700	0.08-0.45	$\leq$ 0.7	$\leq$ 0.08	$\sim 10^{26}$

Chapter 2

1D models of primordial Earth-like exoplanets

2.1 Introduction

As we have seen in the Chapter 1, in the past two decades there was a major improvement in our knowledge of exoplanet properties. In particular rocky, terrestrial exoplanets such as the one orbiting around Proxima Centauri (Anglada-Éscudé et al. 2016) are found at an ever growing rate. It is estimated that approximately 30% of stars in the solar neighbourhood have planet with sizes within two times Earth's radius and orbital periods within 85 days (Fressin et al. 2013).

A further step is to study potential habitability of these planets. In the last few years, the quest for habitability has been supported by increasing detections of traces of atmospheric signatures in exoplanets (e.g., Brogi et al. 2014), through photometric and spectroscopic methods using either space-borne and/or ground-based observational facilities. Such observations provide constraints on pressure and temperature profiles, energy circulation, along with prescriptions for non-equilibrium molecular composition, and presence of clouds and hazes (e.g., Sing et al. 2016).

Radiative-Thermo-Convective (RTC) models have been exploited to investigate exoplanet habitability either defining a general habitable zone for $N_2/CO_2/H_2O$ planets (Kopparapu et al. 2013), or focusing to single planets such as e.g., in the case of Gliese 581d (von Paris et al. 2010; Wordsworth et al. 2010; Hu & Ding 2011). Those studies suggest that RTC models give useful general indications of the impact on the planetary surface temperature

of parameters such as e.g., ground pressure and CO2 mixing ratio.

The minimal set of observables to be derived by modeling efforts are pressure and temperature profiles, abundances and chemistry, and atmospheric dynamics. However, even in such limited configuration, model complexity increases rapidly if models should end up doing a reasonable job in representing the real world. In addition, for rocky planets the number of unknowns goes up because of uncertain initial conditions, the interactions between the surface, the interior and the atmosphere, and the possible impact of biological processes.

In this chapter we will describe a new numerical code, developed in Aresu, Locci et al., in preparation, my contribution focus on the calculation of line shape of the water, that performs 1D radiative transfer, and couples the results with a RTC technique. Although 1D models are unable to capture the mean vertical structure of planetary atmospheres, in particular in the case of terrestrial planets in the habitable zone of low-mass stars, they are very useful to test the effects of some processes or to explore a parameter space too broad for heavy 3D modeling. Like, for instance in the study by Yang et al. (2016), that compares the radiative transfer in H_2O-rich atmospheres. In other studies, 1D models are used to study the validity of k-distribution (see section 2.2.4) when the stellar spectrum is correlated with the atmosphere absorption (H_2O also shapes the spectrum of cool stars), or e.g., the effect of different Collisional Induced Absorption (CIA) parametrizations, foreign broadening (i.e. broadening induced by collision with molecules of other species), and various isotopologues ratios.

In this work we focus on the atmospheric composition and its interaction with the planet radiation environment, i.e. the spectrum of the illuminating star.

The steps adopted in our modeling are:

- Since the amount of green-house gases plays a fundamental role in shaping the habitable zone around a given star, in order to explore the boundaries of the HZ, we perform various models for Earth-like exoplanets with different atmospheric chemical profiles, blending CO_2, N_2, and H_2O in general, albeit reasonable mixing ratios.

- We generate line by line spectra, and subsequently transform them through a $k-$distribution technique creating look up tables for the absorption coefficients of these species. To minimize the impact of interpolation errors in the radiative fluxes we pre-calculate spectra also accounting for different CO_2 mixing ratios.

- We solve the radiative transfer in 1D plane parallel atmospheres exploiting such $k-$distributed

optical depths within the discrete-ordinate method solver DISORT (Stamnes et al. 1988).

- Finally, to derive equilibrium temperature profiles of terrestrial-like planets around arbitrary stars for habitability study purposes, we use the RTC technique.

The RTC approach allows to handle in a relatively simple way the complex dynamical processes that take place into the atmospheric gases. Neglecting the conductions; energy in a planetary atmosphere may be transported by either radiative and convective mechanisms. The dominant process will be the one that follows the path of lower "resistence". Above the troposphere where the density is low, and so the opacity, radiative transport dominates over the convection. On the contrary in the lower atmosphere where the opacity strongly increases, the heat is transported from the ground atmospheric layers to the higher ones by convective motions. To handle such a scenario the so called convective adjustment (CA) technique is frequently assumed. The method consists in adjusting the lapse rate, i.e. the rate at which the temperature decreases with height, to a Critical Lapse Rate (CLR) ∂T_z (z being the vertical coordinate) corresponding to the case of a moist adiabatic atmosphere (see section 2.4.2) . In other words, during the numerical simulation each time the lapse rate exceeds ∂T_z, it is is forced to this latter.

In §2.2 we describe the techniques used to compute and process the absorption coefficients. In §2.3 we present the model validation, and in §2.4 illustrative results using varying amounts of CO_2. In §2.4 the model is also discussed, and applied to the case of the exoplanet Kepler 1229b. §2.5 contains a discussion of the results.

2.2 The radiative transfer model

RTC To describe the history of a photon during its journey inside the atmosphere, the absorption and scattering coefficients are crucial quantities, They depend on the temperature and the density of the medium. Since the radiation is efficiently reprocessed and remitted in the thermal band, it is also necessary to know of the emission coefficient, that as scattering and absorption coefficients depends on the temperature and density. As stated in the introduction we assume a 1D plane-parallel atmosphere. Each layers are homogeneous and characterized by temperature (T), pressure (p), and density ρ. The radiative transfer

of monochromatic radiation at frequency ν results

$$\mu \frac{dI_\nu(\tau_\nu, \mu, \phi)}{d\tau_\nu} = I_\nu(\tau_\nu, \mu, \phi) - S_\nu(\tau_\nu, \mu, \phi) \tag{2.1}$$

where $I_\nu(\tau_\nu, \mu, \phi)$ is the specific intensity at the optical depth τ_ν along the direction (μ, ϕ), μ being the cosine of the polar angle and ϕ the azimuthal angle. The optical depth is defined as follows

$$\tau_\nu = -\int_0^z \alpha(\nu, z')dz' \tag{2.2}$$

with $\alpha(\nu, z')$ the extinction coefficient, given by the sum of absorption and scattering coefficients, and $S_\nu(\tau_\nu, \mu, \phi)$ the source function, the ratio between the emission and extinction coefficients. equation (2.1) is solved by means of the discrete ordinate method (see Appendix B.

The atmosphere we consider is the one of a terrestrial-sized planet composed of N_2, CO_2 and H_2O in varying mixing ratios. Within the parameter space that we have chosen, we may construct a synthetic atmosphere dominated by N_2 with traces of CO_2 and H_2O, mimicking the Earth primordial atmosphere before the appearance of the cyanobacteria that caused the so-called *great oxygenation event* (Holland 2002), or a CO_2 dominated atmosphere to study CO_2-rich atmospheres such as e.g., Martian-like environments.

Many definitions of habitability can be found in the literature. In this work we aim at modeling a planet in principle capable of forming life and sustaining it. Such requirement identifies a fiducial range of atmospheric pressures and temperatures which naturally includes and extend the current terrestrial atmospheric physical properties. In Table 2.1 we summarize the choice of pressure p, temperature T, and CO_2 and H_2O volume mixing ratios.

Table 2.1: Parameter space exploited in spectral calculations

Parameter	Values	N Models
Pressure [atm]	from $\log(p) = -3$ to 1.8, step of 0.5	10
Temperature [K]	from $T = 100$ to 500 K. step of 20 K	21
CO_2 [ppm]	0,100,200,500,1000,2000,10000,20000,50000,100000,200000,500000,950000	13
H_2O [ppm]	0,1,10,100,1000,10000,50000,100000,200000,500000,900000	11

2.2.1 Absorption coefficient and spectral shapes

Since monochromatic emission is an abstraction, the absorption coefficient k_{lu} at the frequency ν for a transition between the two levels l (lower) and u (upper) is characterized by a (normalized) line shape function f_{lu}

$$k_{lu}(T,p) = n\mathcal{S}_{lu}(T) f_{lu}(\nu - \nu_{lu}, T, p) \tag{2.3}$$

where $\mathcal{S}_{lu}$ is the transition line strength, ν_{lu} the central frequency, and n the number density of the absorbing particles (cm^{-3}), f_{lu} is the line shape function. Line strengths are tabulated at a reference temperature T_{ref}

$$\mathcal{S}_{lu}(T) = \mathcal{S}_{lu}(T_{\mathrm{ref}}) \times \frac{Q(T_{\mathrm{ref}})}{Q(T)} \times \frac{e^{-c_2 E_l/T}}{e^{-c_2 E_l/T_{\mathrm{ref}}}} \times \frac{1 - e^{-c_2 \nu_{lu}/T}}{1 - e^{-c_2 \nu_{lu}/T_{\mathrm{ref}}}}. \tag{2.4}$$

where E_l is the energy of the lower level involved in the transition, and c_2 is the second radiation constant (see e.g. Liou 1980). In the right hand side of the equation the second term is the ratio of the equipartition functions Q at the temperatures T and T_{ref} , respectively; the third term is the ratio of Boltzmann distributions, while the fourth accounts for stimulated emission.

We assembled absorption coefficients exploiting the molecular spectroscopic database HITRAN 2012 (Rothman & et al. 2013) in the interval $0.24-1,000$ μm ($0.24-42,000$ cm^{-1}), relevant to planetary studies. The spectra were calculated for all the possible combinations of the parameters described in Table 2.1, for a total of $\sim 30,000$ absorption spectra. In each model N_2 acts as a filling gas. In a planetary atmosphere sources of broadening are the natural width, Doppler shifts, and collisions (pressure). The first broadening is due to the Heisenberg uncertainty principle, since we don't know exactly the frequency of a photon, it will appear us different each time. The line shape in this case is a Lorentzian profile. The natural broadening is always negligible when compared to the broadening due to Doppler or pressure effects. The Zeeman broadening at planetary temperatures and pressures in negligible. Doppler broadening is due to the different thermal (or for instance to the turbulent velocities in convective regions) velocities of atoms and molecules. Assuming a Maxwellian velocity distribution, we obtain the following Gaussian line shape

$$f_D(\nu - \nu_0) = \frac{1}{\alpha_D \sqrt{\pi}} e^{-\left(\frac{\nu-\nu_0}{\alpha_D}\right)^2} \tag{2.5}$$

with the width α_D given by

$$\alpha_D = \frac{\nu_0}{c}\sqrt{\frac{2k_BT}{m_i}} \tag{2.6}$$

where ν_0 is the natural wavenumber of the transition, m_i the mass of the $i-$th species, c the speed of light, and k_B the Boltzmann constant. Pressure broadening is produced by random phase interruptions induced by collisions. If we assume a Poissonian distribution for the phases we obtain a Lorentzian profile

$$f_L(\nu - \nu_0) = \frac{1}{\pi}\frac{\alpha_L}{(\nu - \nu_0)^2 + \alpha_L^2} \tag{2.7}$$

where α_L is given by

$$\alpha_L = \left[(1-\epsilon_i)\alpha_f^{(i)}p + \epsilon_i^{(i)}\alpha_s^{(i)}p\right]\left(\frac{T_{\rm ref}}{T}\right)^{n_i} \tag{2.8}$$

In equation (2.8) ϵ_i is the volume mixing ratio, $\alpha_f^{(i)}$, $\alpha_s^{(i)}$ and n_i are the foreign (atoms or molecules of other species) broadening , self (atoms or molecules of the same species) broadening and temperature exponent for the $i-$th species. These quantities are provided by the HITRAN database at the reference temperature $T_{\rm ref} = 296$ K and pressure $p_{\rm ref} = 1$ atm. At high pressures the pressure broadening is dominant, while at lower pressures the line broadening is due to a combination to the effects of the pressure and the Doppler widths. The resulting line profiles are the so-called Voigt line profiles, given by the convolution of thermal and pressure effects. For the physical conditions described by the parameters listed in Table 2.1 these two broadening mechanisms are the major processes affecting line shapes. The convolved Voigt profile characterized by a thermal line centroid and Lorentzian wings reads as

$$V(\nu) = \frac{1}{\pi^{-1/2}\alpha_D}H(a,u) \tag{2.9}$$

with

$$H(a,u) = \frac{a}{\pi}\int_{-\infty}^{+\infty}\frac{e^{-y}}{a^2 + (u-y)^2}dy \tag{2.10}$$

where $u = (\nu - \nu_0)/\alpha_D$, and $a = \Gamma/4\pi\alpha_D$, Γ being the damping rate. The calculation of the Voigt profile is typically the most time consuming step while building absorption spectra from molecular databases. To maximize the quality to calculation-time ratio we use the fast and accurate algorithm designed by Wells (1999).

Due to their peculiar characteristics some molecules show deviations from the Voigt profile. Being carbon dioxide and water among them, they need the separate treatment

discussed in the next Section.

2.2.2 Line modifications and continuum description

CO_2 line profiles are observed to be sub-lorentzian away from the line center (Burch et al. 1969). We use the scaling factor suggested by Perrin & Hartmann (1989) beyond 3 cm^{-1} from the line center. Moreover, to adjust for the asymmetry of the line profile we applied the normalized correction factor given in van Vleck & Huber (1977) given by:

$$\phi(\nu, \nu_0) = \left(\frac{\nu}{\nu_0}\right) \times \frac{\tanh(h\nu/2k_BT)}{\tanh(h\nu_0/2k_BT)} \tag{2.11}$$

In Figure 2.1 it is shown how such modifications impact on the line shape The CO_2 contin-

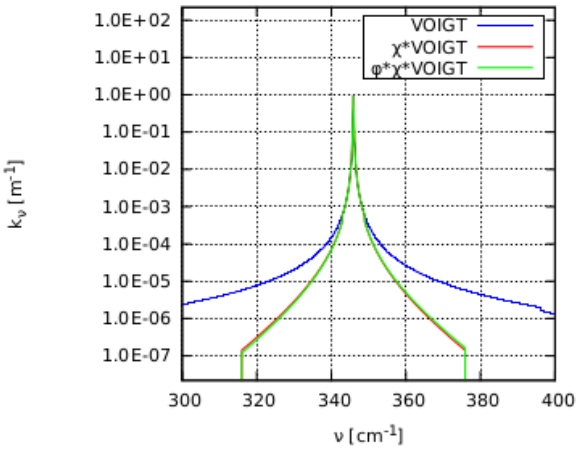

Figure 2.1: Line shapes of CO_2 as functions of the frequency. The Voigt profile (blue line) is corrected by means the sublorentzian factor (red line) and the factor of asymmetry (green line).

uum is calculated using the (semi-empirical) MT_CKD model, which provides the foreign continuum from 1 to 1000 μm ($0-10000$ cm^{-1}) (Mlawer et al. 2012). The CO_2 molecule also experiences CIA due to encounters with other CO_2 molecules, that generates line absorption into bands otherwise empty (see appendix C). CIA differs from the broadening due to the pressure because in this case we have incoherent collisions. We account for these effects using the theoretical results of Gruszka & Borysow (1997) in the interval $33 - 1000$ μm ($10 - 300$ cm^{-1}) and interpolating the experimental results of Baranov et al. (2004) in the interval $5 - 9$ μm ($1100 - 2000$ cm^{-1}). The spectrum obtained with the line calculation is

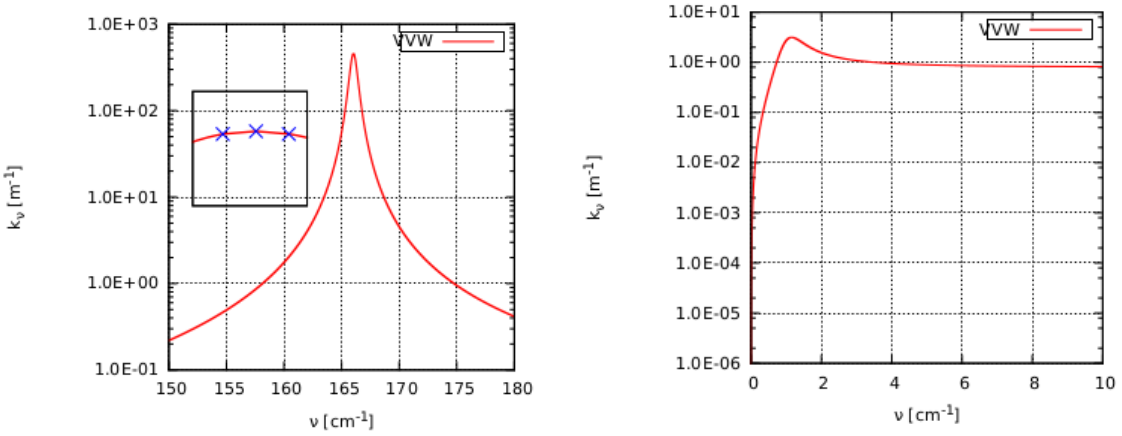

Figure 2.2: Left panel: Van Vleck-Wisskopf profile at high frequencies of H_2O; the zoom shows the three points of the line center belonging to the Voigt profile. Right panel: the strong asymmetry in the Van Vleck-Weisskopf profile at low frequencies.

ultimately added to the continuum calculations: to avoid an overestimate of the absorption, each CO_2 line is calculated out to 25 cm^{-1} from the line center, hence following Mlawer et al. (2012) we consider continuum all the absorption produced further.

In the case of H_2O we follow the prescriptions of Halevy et al. (2009) and Mischna et al. (2012). We calculate a Voigt profile within 40 times the Doppler width from the line center, and a Van Vleck-Weisskopf (VVW) profile out to 25 cm^{-1} from the natural wavenumber of the transition ν_0. The VVW profile is given by

$$f_{VVW}(\nu, \nu_0) = \left(\frac{\nu}{\nu_0}\right)^2 \left(f_L(\nu, \nu_0) + f_L(\nu, -\nu_0)\right) \tag{2.12}$$

where f_L is a pure Lorentzian profile (see appendix D) . In order to avoid to underestimate the absorption, the Voigt profile is computed in (at least) three points, specifically at the line center, and where the Voigt profile is replaced by the VVW profile. As a consequence at high frequencies the profile tends to be Lorentzian, while at low frequencies become strongly asymmetrical (see Figure 2.2). Also for H_2O we use the MT_CKD model, which provides both foreign and self continuum from 0.5 to 1000 μm (0 to 20000 cm^{-1}). The MT_CKD model derives water line shapes by fitting the continuum in spectral regions where it is best constrained by measurements. The same line shape is extended to spectral regions where the continuum is not well constrained or simply never been measured.

2.2.3 Synthetic spectra

The absorption spectrum is built as follows

$$
\begin{aligned}
k_\nu &= k_{\mathrm{CO_2}} + k_{\mathrm{H_2O}} + k_{\mathrm{N_2}} \\
&= \epsilon_{\mathrm{CO_2}} \left[\sum_{\delta_{\nu_0} < 25\,\mathrm{cm^{-1}}} k_\nu^{\mathrm{CO_2}} + (1 - \epsilon_{\mathrm{CO_2}}) \left(\frac{p}{p_{\mathrm{ref}}} \right) \left(\frac{T_{\mathrm{ref}}}{T} \right) k_f^{\mathrm{CO_2}} + k_\nu^\star \right] \\
&+ \epsilon_{\mathrm{H_2O}} \left[\sum_{\delta_{\nu_0} < 25\,\mathrm{cm^{-1}}} k_\nu^{\mathrm{H_2O}} + (1 - \epsilon_{\mathrm{H_2O}}) \left(\frac{p}{p_{\mathrm{ref}}} \right) \left(\frac{T_{\mathrm{ref}}}{T} \right) k_f^{\mathrm{H_2O}} + \epsilon_{\mathrm{H_2O}} \left(\frac{p}{p_{\mathrm{ref}}} \right) \left(\frac{T_{\mathrm{ref}}}{T} \right) k_s^{\mathrm{H_2O}} \right] \\
&+ \epsilon_{\mathrm{N_2}} \sum_{\delta_{\nu_0} < 25\,\mathrm{cm^{-1}}} k_\nu^{\mathrm{N_2}}
\end{aligned}
\tag{2.13}
$$

where $\delta_{\nu_0} = |\nu - \nu_0|$, $k_\nu^\star$ indicates the CO_2 self collision induced absorption, and subscripts f and s stand for foreign- and self-continuum, respectively. The volume mixing ratio of the i-th species is ϵ_i.

For each model listed in Table 2.1 we compute equation (2.13) within the interval $0.24 - 100$ μm ($10 < \nu < 42000$ cm^{-1}). Similarly to Mischna et al. (2012), we first divide the full spectrum in 14 reference spectral bands (Table 2.2), then for each band we identify the narrowest line among all the species composing the atmosphere. Using as resolution $\mathcal{R}$, one fifth of the narrowest line width we compose the spectra in each band. In this way we have at least 5 points describing the narrower lines and the resulting raw spectrum is at moderate to high resolution. In Table 2.3 we report four different indicative cases. All the absorption spectra are at this stage naturally calculated with different resolutions and one spectrum can be formed by millions of points, especially at low pressures.

Two important requirements in radiative transfer calculations are the speed of execution and accuracy. Thus, spectra must be constructed at low resolution, but at the same time the optical depths at a degraded resolution, with respect to the raw spectra should be such that the final fluxes are still precise enough (usually within few %). One of the most popular method to describe spectra without losing precision is the so-called $k-$correlation method.

2.2.4 The $k-$distribution prescription

The $k-$distribution method for a homogeneous atmosphere is based on the ordering of gaseous spectral transmittances, since in this case, for a given spectral interval, the spectral

Table 2.2: spectral regions in which detailed calculations are performed.

band ID	wavenumber (cm^{-1})	wavelength (μm)	band
1	$10 - 166$	$60.24 - 100$	IR†
2	$166 - 416$	$24.04 - 60.24$	"
3	$416 - 625$	$16.00 - 24.04$	"
4	$625 - 710$	$14.00 - 16.00$	"
5	$710 - 833$	$12.00 - 14.00$	"
6	$833 - 1250$	$8.00 - 12.00$	"
7	$1250 - 2222$	$4.5 - 8.00$	"
8	$2222 - 3087$	$3.24 - 4.5$	SOLAR
9	$3087 - 4030$	$2.48 - 3.24$	"
10	$4030 - 5370$	$1.86 - 2.48$	"
11	$5370 - 7651$	$1.30 - 1.86$	"
12	$7651 - 12500$	$0.80 - 1.30$	"
13	$12500 - 24960$	$0.40 - 0.80$	"
14	$24960 - 41666$	$0.24 - 0.40$	"

† As customary, we label SOLAR the flux between 0.24 and 4.5 μm, and infrared the portion between 4.5 and 100 μm.

Table 2.3: Resolution of the raw spectra for models† at low and standard pressure, and at low and high temperature.

p (atm)	T (K)	$\mathcal{R}$ at 100 cm^{-1}	$\mathcal{R}$ at 20000 cm^{-1}
0.001	220	5×10^6	8×10^6
0.001	340	5×10^6	7×10^6
1	220	1×10^5	4×10^6
1	340	1×10^5	4×10^6

† The abundances of H_2O and CO_2 are 100 and 1000 ppm, respectively.

transmittance is independent of the ordering of k with respect ot the wavenumber. Hence, wavenumber integration may be replaced by an integration over the k space (Fu & Liou 1992). For a given spectral band we can write the average transmission throughout a homogeneous path of length z, as follows

$$\overline{T} = \frac{1}{\Delta\nu} \int_{\Delta\nu} e^{-k_\nu z} d\nu \tag{2.14}$$

Such formulation of the transmission is not optimal when handled by a radiative transport module of general nature. In fact, each frequency sub-interval will likely contain up to few million points. This will unavoidably cause the computational time to be exceedingly long, if we want to obtain the solution of the radiative transfer problem through several atmospheric layers.

Workarounds have been proposed already in the 1930s; further study of such ideas ended up in the development of the $k-$correlated method (Lacis & Oinas 1991). An absorption spectra such as the one depicted in the left panel of Figure 2.3 is partitioned in M intervals of width Δk_j, while the wavenumber band $\Delta\nu$ is sub-divided in N intervals of width $\Delta\nu_l$. For a given $\Delta\nu$ we sum sub-intervals $\Delta\nu_j$ which have absorption coefficients included in the

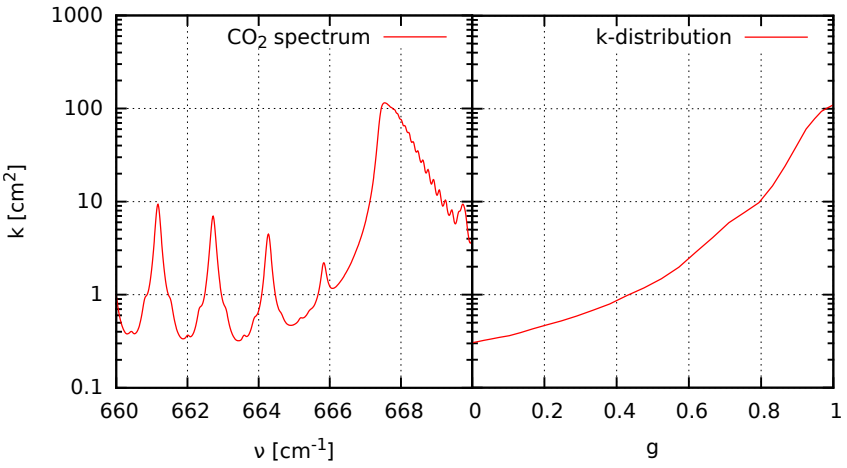

Figure 2.3: Left panel: CO_2 spectrum in the $660-670$ cm^{-1} interval for a gas at pressure $p = 1$ atm and temperature $T = 296$ K. Right panel: derived $k-$distribution.

range $[k_j, k_j + \Delta k_j]$. This leads to the definition of the probability distribution function

$$f(k_j) = \frac{1}{\Delta\nu} \sum_{l=1}^{N} \frac{\Delta\nu_l}{\Delta k_j} W(k_j, k_j + \Delta k_j) \tag{2.15}$$

where Δk_j is the absorption coefficient interval that includes the k_ν associated with a given $\Delta\nu$, and W is a window function equal to one when k_ν belongs to interval Δk_j and 0 otherwise. Integrating $f(k)$ over k, the cumulative probability function takes the form

$$g(k) = \int f(k)dk \tag{2.16}$$

Its inverse $g^{-1} = k(g)$, is the so-called $k-$distribution. Basically $k(g)$ represents the ranking of k depending on its contribution to the total absorption in that same band (Figure 2.3, right panel). The transmission can then be written as follows

$$\overline{T}(z) = \int_0^1 e^{-k(g)z} dg \tag{2.17}$$

The advantage in using this formulation is evident considering that its integral is smooth and can then be approximated through Gaussian quadratures as follows

$$\overline{T}(z) = \sum_{i=1}^{N_p} \omega_i e^{-k_i z} \tag{2.18}$$

where ω_i are the weights associated to each k_i values. To achieve enough precision on the overall radiative transfer it is sufficient to choose $N_p = 32$ (see e.g., Mischna et al. 2012). The transmission, which before such transformation could only be calculated iterating through millions of spectral points, is now condensed in a few tens of points for each band, making the storage of absorption coefficients and their use for the radiative transfer calculation faster and simpler. A second fundamental benefit of this formulation is that spectra at largely different temperature and pressure are now degraded at the same resolution, still keeping the precise information on the value of the transmission. Radiative transfer is then solved for each of the quadrature intervals in equation (2.18) from the top of the atmosphere (TOA) to the lowest layer (typically the ground). In each layer the flux of a given quadrature interval F_i is transported using the optical depth τ_i corresponding to the transmission calculated at the same quadrature interval.

The method implicitly assumes that throughout the atmosphere in each band where the $k-$distribution is calculated, spectra are correlated. This means that absorption at, e.g., low g in the upper atmosphere and in the lower atmosphere should fall in the same regions of the original spectra, i.e. at the same wavelengths. The correlation is automatically ensured along a homogeneous path, while it is much more difficult to preserve if the line of sight crosses varying pressure and temperature layers or regions where chemically inhomogeneities are present. In the latter case the presence of different absorbers might affect the absorption spectra, especially for distant layers, destroying the mapping between the absorption at a given wavelength and the $g-$space. This issue has been investigated by Fu & Liou (1992) comparing the results of a line by line code with the $k-$correlated method for different species. These authors, using 12 bands in the infrared, found that the errors in the fluxes for CO_2 and H_2O molecules are less than 0.2%. Such results enable the use of $k-$correlated techniques in computing radiation transport in a 1D atmosphere composed of variable amounts of CO_2 and H_2O like the one discussed in this work.

Once the $i-$th absorption coefficient k_i has been derived, the optical depth for the $i-$th layer and the $j-$th quadrature point is obtained in the hydrostatic equilibrium approximation as

$$\tau_i^j(\nu) = \frac{k_i^j(\nu)}{g_P \mu} \Delta p_i \tag{2.19}$$

where g_P is the planetary gravitational acceleration, μ the mean molecular mass of the atmosphere, and Δp_i the pressure difference between the $i-$th layer and the layer above.

The optical depths are given in input to the DISORT module (Stamnes et al. 1988), which solves the radiative transfer problem through the discrete ordinate method. Once the radiative transfer has been solved in each of the quadrature intervals the flux at each layer i is reconstructed using the same quadrature weights

$$F_i = \sum_{j=1}^{N_p} \omega_j F_{ij} \tag{2.20}$$

2.2.5 $k-$distribution resolution

The spectra are processed through the method described above in the 14 bands listed in Table 2.2. Each band is then divided in 10 sub-bands, which is the spacing where we perform the $k-$distribution (see Figure 2.6). Hence, we use 140 bands in the range $0 - 42000$ cm^{-1}. The $k-$distributed values are initially stored, and then read and interpolated from the main

program depending on the required values of pressure, temperature, and CO_2 and H_2O abundances.

2.3 Code validation

We compare the present model results with those obtained using a similar 1D $k-$distribution radiative transfer model developed at NASA Ames (Toon et al. 1989). We also incorporate the absorption coefficients calculated from Mischna et al. (2012), the so-called $k-$distribution radiative transfer Model (KDM), into our radiative transfer module, and include the resulting outcomes in the validation procedure. The AMES $k-$distribution is calculated using 7 bands in the visible range and 5 in the infrared, while the KDM $k-$distribution uses the same 14 bands described in column 2 of Table 2.2.

We aim at reproducing the upward and downward fluxes in the SOLAR and infrared bands for a Mars-like planet with a wet 0.5 atm cloud and clear sky atmosphere composed of CO_2 (95%) and N_2 (5%). The only scattering process is Rayleigh scattering. The solar constant is set to 220 W m^{-2}, which is the expected illumination for Mars at its early evolutionary stage, from a 5778 K star. This also includes a 0.5 factor for the incoming flux to account for the the day/night variation. The validation setup is summarized in Table 2.5. The input atmosphere for the martian validation is the one listed in Table 2.4 and in Figure 2.5 a plot is showed, applying a factor 0.5 at each layer for the pressure and a shift of -50 K at each layer for the temperature.

As noted above 1D radiative transfer codes, especially when they serve as proxies for energy balance models or GCMs are required to be fast, therefore the use of very low resolution $k-$correlated absorption cross-sections is frequent. For the very nature of the $k-$correlation method the input spectrum for such wide band models should be smooth, such as e.g., a black body integrated in the same bands, or a binned real stellar spectrum.

In Figure 2.4 we show the integrated fluxes between 0.24 and 4.5 μm (SOLAR band) and between 4.5 and 1000 μm (infrared band). The different cross-sections and the different radiative transfer module do not introduce important differences in the downward fluxes, while there is a 2.5 W/m^2 difference in the upward visible flux, where Rayleigh scattering dominates. This is a straightforward consequence of the different resolutions at which calculations are performed by the different models. As in AMES or KDM\DISORT models, we compute the Rayleigh scattering cross-section for our spectral ranges at the center of the band. Because the Rayleigh scattering depends steeply on wavelengths, in this way, low

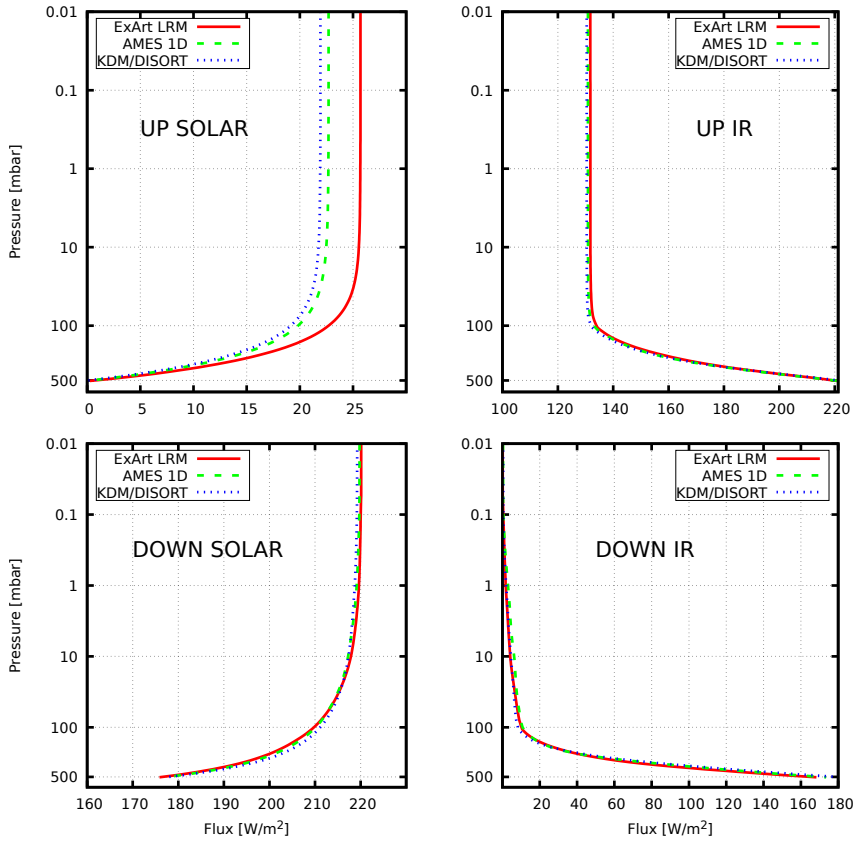

Figure 2.4: Comparison of model results with the AMES 1D code for the upward and downward fluxes in the infrared and SOLAR bands. This work: red solid lines; AMES: green dashed lines; KDM absorption coefficients into the present code: blue dotted lines.

resolution calculations tend to underestimate the cross-sections. Increasing the number of bands (i.e. increasing the resolution), it is possible to reduce the error in the calculation of the Rayleigh cross-section.

2.4 Results

2.4.1 Fluxes for the benchmark case

We setup a benchmark case to study early Earth-like exoplanets using an atmosphere with ground pressure of 1 atm, tropospheric water at 60% ground relative humidity and well mixed

Table 2.4: Benchmark atmosphere for a model with $p_0 = 1$ atm and $T_0 = 300$ K.

LAYERS 1-50		LAYERS 51-100	
Pressure [atm]	Temperature [K]	Pressure [atm]	Temperature [K]
0.000107	217.0000	0.042001	217.0000
0.000123	217.0000	0.046003	217.0000
0.000143	217.0000	0.050332	217.0000
0.000166	217.0000	0.055003	217.0000
0.000192	217.0000	0.060045	217.0000
0.000220	217.0000	0.065472	217.0000
0.000255	217.0000	0.071314	217.0000
0.000293	217.0000	0.077588	217.0000
0.000336	217.0000	0.084322	217.0000
0.000385	217.0000	0.091539	217.0000
0.000443	217.0000	0.099260	217.0000
0.000506	217.0000	0.107518	217.0000
0.000579	217.0000	0.116327	217.0000
0.000662	217.0000	0.125722	217.0000
0.000755	217.0000	0.135725	217.0000
0.000861	217.0000	0.146358	217.0000
0.000982	217.0000	0.157650	217.2700
0.001116	217.0000	0.169626	217.9200
0.001268	217.0000	0.182308	218.5800
0.001440	217.0000	0.195719	219.2200
0.001633	217.0000	0.209880	219.8700
0.001848	217.0000	0.224818	223.0200
0.002091	217.0000	0.240554	226.1600
0.002364	217.0000	0.257108	229.3000
0.002668	217.0000	0.274504	232.4200
0.003007	217.0000	0.292734	235.5200
0.003386	217.0000	0.311826	238.6100
0.003809	217.0000	0.331816	241.6900
0.004282	217.0000	0.352664	244.7400
0.004804	217.0000	0.374430	247.7600
0.005386	217.0000	0.397096	250.7700
0.006032	217.0000	0.420660	253.7400
0.006748	217.0000	0.445122	256.6900
0.007542	217.0000	0.470484	259.6000
0.008418	217.0000	0.496746	262.4800
0.009386	217.0000	0.523884	265.3200
0.010452	217.0000	0.551880	268.1200
0.011628	217.0000	0.580756	270.8700
0.012923	217.0000	0.610432	273.5700
0.014343	217.0000	0.640926	276.2200
0.015904	217.0000	0.672198	278.8200
0.017612	217.0000	0.704210	281.3500
0.019484	217.0000	0.736924	283.8200
0.021531	217.0000	0.770315	286.2300
0.023768	217.0000	0.804298	288.5600
0.026206	217.0000	0.838866	290.8100
0.028863	217.0000	0.873932	292.9900
0.031753	217.0000	0.909476	295.0900
0.034896	217.0000	0.945402	297.1100
0.038307	217.0000	1.000000	300.0100

CO_2 at 1% in each layer. The humidity profile upwards follows the Manabe & Wetherald (1967) profile.

The temperatures are kept fixed in each layer, while the water abundance is calculated

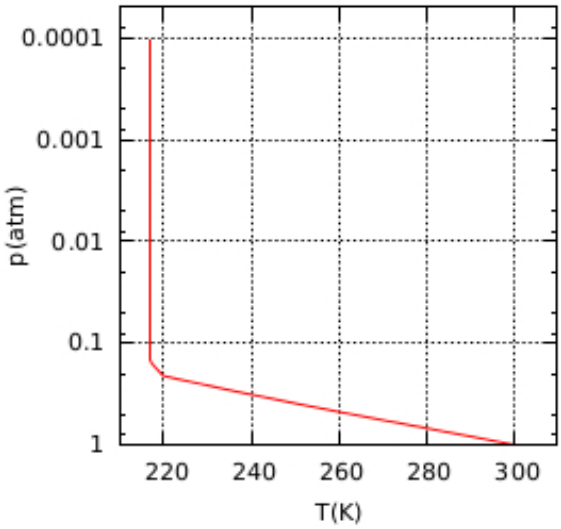

Figure 2.5: Benchmark atmosphere (see Table 2.4).

according to the assumed ground humidity propagated to the other layers by means of the Manabe & Wetherald (1967) model.

We explored the whole CO_2 parameter space investigating the effect of variable CO_2 abundance on the downward flux at the ground and on the outgoing long wave radiation. We run models using CO_2 abundance with values 100 ppm, 1000 ppm, 10000 ppm, 100000 ppm and 950000 ppm at three different ground N_2 pressures (0.1 atm, 1 atm and 10 atm). To highlight the role of CO_2 concentration the temperature profile is kept fixed. The right panel of Figure 2.6 shows the impact on the fluxes of CO_2 abundance and atmospheric pressure both for the downward and upward fluxes. Here the full range of CO_2 mixing ratio

Table 2.5: Atmospheric parameters used in the model validation.

Parameter	Label	Value
ground pressure	p_0	0.5 atm
ground temperature	T_0	250 K
Bond albedo	A_B	0.0
irradiation zenith angle	$\cos(\varphi)$	1.0
Day/Night factor		0.5
integrated incident flux	S	220 W m^{-2}
stellar temperature	$T_\star$	5778 K

CO_2	Dry CLR [K/km]	Wet CLR [K/km]
0.0001	28.93	28.93
0.001	28.93	28.93
0.01	28.99	28.99
0.10	29.55	29.49
0.95	35.20	32.94

is explored, for a dense (10 bar), moderate (1 bar) and thin atmosphere (0.1 bar). The computation of absorption coefficients at high pressure is key to obtain accurate fluxes in this regime, especially for low resolution models. Running a model that would interpolate a too coarse grid (e.g., $\Delta p = 1$ dex in pressure or $\Delta T = 40$ K in temperature) could cause errors in the flux.

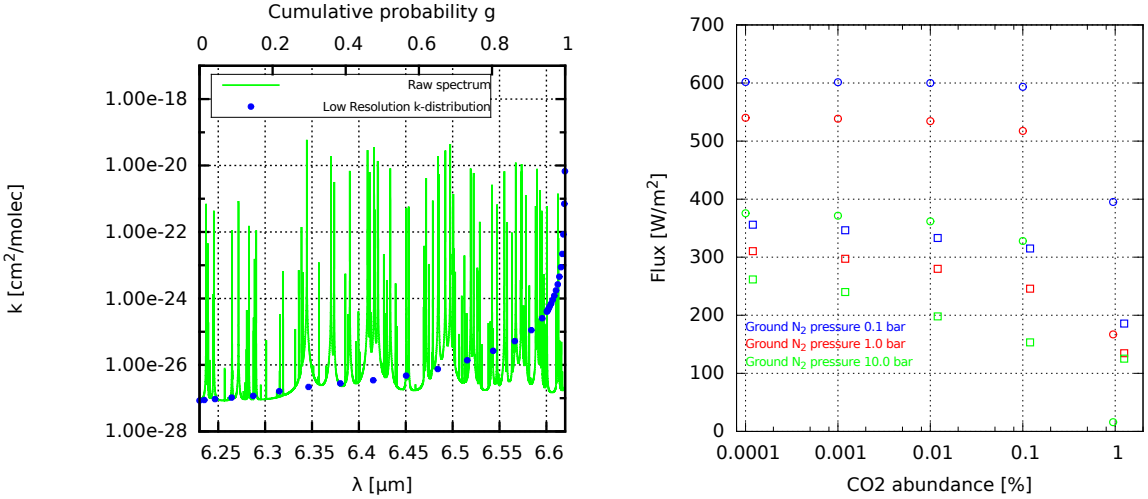

Figure 2.6: Left panel: in green the raw spectrum (k_ν vs λ), in blue the correspondent k-distributed spectrum (k_ν vs g). Right panel: empty circles (squares) are solar (infrared) fluxes at the ground (TOA) for atmospheres with 0.1, 1 and 10 atm of N_2 (blu, red and green colours respectively).

2.4.2 RTC model

To study the thermal evolution of the atmospheres described previously, and with the final intent of studying exoplanets habitability, we developed a RTC model. The backbone radiative transfer model has been detailed above. It gives heating rates at each atmospheric layer. The RTC model is based on the (CLR) ∂T_z (see §2.1), i.e. the critical temperature

difference between two contiguous layers that marks the passage from the radiative to the convective regime. Whenever the CLR is exceeded we perform convective adjustment as prescribed in Manabe & Wetherald (1967). The CLR in the wet case is calculated in the moist adiabatic regime:

$$\partial T_z^{\rm wet} = \partial T_z^{\rm dry} \times \left(1 + \frac{L_{\rm vap} W_s}{RT}\right) / \left(\frac{1 + W_s L_{\rm vap}^2}{c_p R_{\rm w} T^2}\right) \tag{2.21}$$

where c_p is the specific heat at constant pressure of the atmosphere, $L_{\rm vap}$ the latent heat of vapourization for water, W_s the water mass mixing ratio, R the gas constant, and $R_{\rm w}$ the water vapour gas constant. $\Gamma_{\rm dry} = g_P/c_p$ is the dry CLR. equation (2.21) assumes water saturation. Since in our models the troposphere is usually under-saturated (i.e. the relative humidity ϕ is set at 60%), we weight the CLR as follows

$$\partial T_z = (1 - \phi)\partial T_z^{\rm dry} + \phi \partial T_z^{\rm wet} \tag{2.22}$$

In the next section we apply the model to the case of planet Kepler 1229b, whose known orbital and physical parameters are listed in Table 2.6. To model the variety of possible scenarios we assume a range of values for unknown parameters (also listed in Table 2.6), calculating a RTC model for each combination for a total of 120 models. In each of these models the initial temperature is set to 200 K, as the new temperature is calculated using the heating rates computed by the radiative transfer module, the water mixing ratio is calculated accordingly using the given humidity value and its dependence with height from Manabe & Wetherald (1967) formulation.

Within the 120 models, since the greenhouse effect have a critical role in the control of the planetary climate we decided to examine the full range of CO_2 abundance. Similarly to what has been done for Gliese 581d by von Paris et al. (2010), Wordsworth et al. (2010) and Hu & Ding (2011), we also investigate different ground pressures. Two values, 2 and 6 M_E, have been selected for the planetary mass, which following Seager et al. (2007) represent a planet with an iron core and a magnesium silicate mantle, either water rich and water poor. Similar arguments may be applied for the choice of the bond albedo A_B in the visible: $A_B = 0.1$ represents a water rich planet, while $A_B = 0.3$ a drier planet. The illumination zenith angle is generally chosen to be 45 degrees. For a small number of models we run simulations using 30 and 60 degrees. Finally we chose to use a dry atmospheric model and a wet model with 60% humidity at the ground.

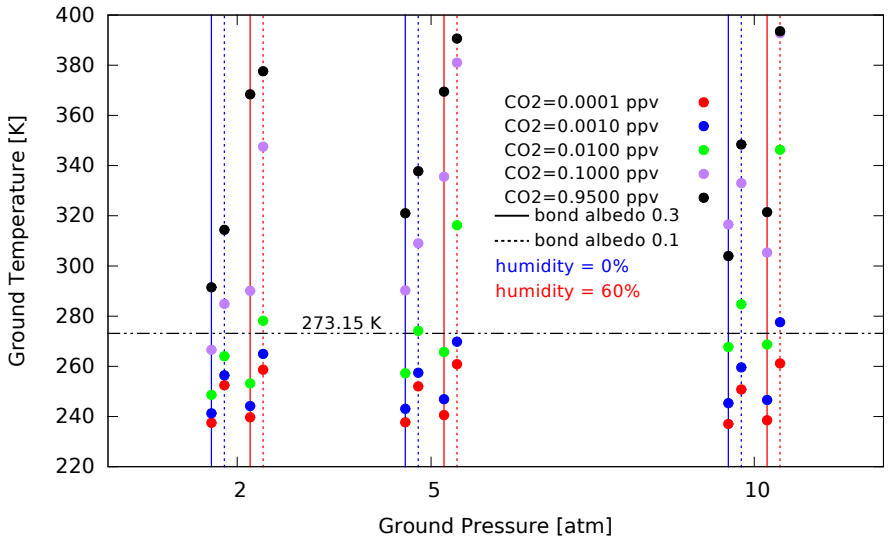

Figure 2.7: Ground temperature vs ground pressure for the 60 models with M_{pl}= 6 M_E. Red, blue, green, purple and black points indicate models with 0.01%,0.1%,1%,10% and 95% of CO2 respectively. Models atop the solid (dashed) lines have bond albedo 0.3 (0.1) while models atop the red (blue) lines are wet with humidity at 60% (dry).

2.4.3 Habitability of Kepler 1229b

In Figure 2.7 we show results for the 60 model runs corresponding to the choice of 6 M_E for the mass of Kepler 1229b. Within the parameter space under investigation, we find that 55 models out of 120 ($\sim$ 46%) allow a ground temperature higher than 273 K. Almost all the 55 successful models have a concentration of CO_2 comparable or less than 0.1% (blue dots), and the number of successful models increase with the humidity, then, albeit Kepler 1229b orbits very close to its parent star, basically due to the relative low temperature of the star, the greenhouse effect is crucial to allow superficial temperature grater than 273 K. For comparison on the Earth and Venus the concentration of CO_2 is about 0.04% and 95% respectively. We stress that the models are cloudy free, the presence of clouds can drastically modify the climate. We extract 5 models with relative humidity at 60% and show their temperature profile in Figure 2.8, (left panel). The convective layer of the planet is higher as the temperature raises due to higher concentrations of CO_2 (see Table 2.3). The CLR for these models goes from $\sim$ 29 to $\sim$ 33 K/km as CO_2 volume mixing ratio increases from 0.0001 to 0.95. In the right panel of the same figure we show the numerical history of the ground temperature towards equilibrium as the number of iterations grows.

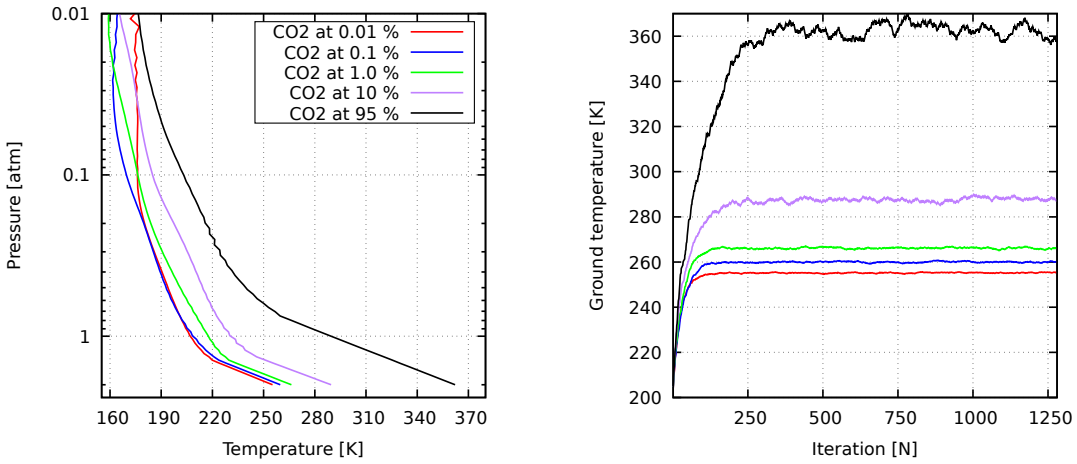

Figure 2.8: Left panel: Temperature profile for a subset of models with albedo 0.1, ground pressure 2 atm and planet mass of 6 Earth masses. Right panel: Behaviour of the ground temperature vs iteration number for the same models.

Table 2.6: Known parameters for the Kepler 1229 system, and assumed parameters for the planet Kepler 1229b.

Known	Assumed
$M_\star = 0.54\ M_\odot$	$M_P = 2,6\ M_\oplus$
$R_\star = 0.51\ R_\odot$	$p_0 = 2,\ 10,\ 20$ atm
$T_\star = 3784$ K	$[CO_2] = 0.01,\ 0.1,\ 1,\ 10,\ 95$ %
$R_P = 1.4\ R_\oplus$	$A_B = 0.1,\ 0.3$
$D_P = 0.282$ AU	$\phi = 0.0,\ 0.6$
	Zenith Angle $= 30,\ 45,\ 60$ deg

2.5 Discussion

The importance of radiative transfer codes for remote sensing science constitutes the major reason for their development and validation, in particular in the light of the emerging field of exoplanet identification and analysis. In this work we have constructed a flexible, efficient, and simple, yet accurate enough tool to study exoplanet atmospheres. The code has been designed to solve direct problems, but it can be easily incorporated in retrieval codes. It assumes a stratified atmosphere in plane-parallel geometry. Different atmospheric characteristics, such as temperature, pressure, and atmospheric species concentrations, need to be specified at the boundaries of each layer. The DISORT code is used as a subroutine in the radiative transfer module to enable the azimuth dependence of multiple scattering. We evaluated the accuracy of our model in several realistic atmospheric scenarios, and by comparing the results of simulations with those produced by two well-known existing codes.

We used a broad 4D parameter space because coarse interpolation must be avoided. The low resolution code version is faster (approximately two orders of magnitude) and guarantees good precision in the fluxes calculation for arbitrary concentrations of CO_2 and H_2O, provided a suitable computational grid (e.g., the one used here). Using a coarser grid for the pre-calculation of the spectra (e.g. a temperature step of 50 K) would introduce differences in the fluxes of the order of $1 - 2\%$.

While 1D radiative transfer models are better suited to deal with clear atmospheres, hazes, clouds and aerosols can be important factors in transmission spectroscopy. However, the lack of suitable 3D input data is a good argument (in addition to the by-far smaller computational time) for using models of limited dimensionality. In this work we do not present models of cloudy atmospheres, but they can be easily implemented, impacting weakly on the handling of radiative transfer calculations (e.g., see Ricchiazzi et al. 1998).

As an application of the present radiative transfer code we study the habitability of the planet Kepler 1229b. We approach the problem performing a grid of models to investigate those parameters that as of today are yet unknown (e.g., planetary mass or albedo). Although a 1D approach can not be considered complete for many reasons (see e.g., Godolt et al. 2016), such a study may place general, necessary constraints for the habitability. In fact, Kepler 1229b sits well within the habitable zone according to Kopparapu et al. (2013), but our analysis allows to quantify the range of ideal properties the planet should possess in order to ensure liquid water on its surface.

A common caveat of these class of models is that they assume a complete redistribution

of energy in the atmosphere within a complete orbit of the planet around its star. Hence, they fail when applied to tidally locked planets. A simple way to estimate whether Kepler 1229b is tidally locked (following e.g. Kasting et al. (1993)) is to calculate the tidal locking radius R_T, as follows (Murray & Dermott 2000)

$$R_T = \left(\frac{3Gk_2}{2\alpha_P\Omega_P}\right)^{1/6}\left(\frac{M_\star^2}{M_P}\right)^{1/6} R_P^{1/2}\left(\frac{\tau}{Q_P}\right)^{1/6} \tag{2.23}$$

where G is the gravitational constant, k_2 the tidal Love number, i.e. the amplitude of the tidal distortion of the planet interior, α_P a parameter that accounts for the moment of inertia of a sphere, Ω_P the initial planet rotation rate, M_P and R_P the planetary mass and radius, τ the age of the system, Q_P the tidal dissipation factor, and $M_\star$ the stellar mass.

Many of these quantities need to be assumed, as only the planet radius, stellar mass and the age of the system are supposed to be reasonably known. Assuming a mass of 6 Earth masses, a tidal dissipation factor $Q_P = 100$ and a tidal Love number of $k_2 = 0.3$, Kepler 1229b is slightly within the tidally locked radius, while using tidal Love number $k_2 = 0.2$ – for a planet denser than the Earth – the planet would be slightly out of the tidal radius. A more detailed tidal and evolutionary analysis of the system, which is beyond the scope of this work, may clarify this aspect, e.g. see Bolmont et al. (2015). Nevertheless according to Driscoll & Barnes (2015) the planet should be well out of the tidal zone where the tidal dissipation would be dominant, hence affecting the planet habitability. This ensures that radiation dominates the energetic budget in the habitable zone of Kepler 1229.

Assuming that Kepler 1229b is not tidally locked, our analysis predicts that the planet has a habitable surface provided that the atmosphere has a ground pressure $p_0 \gtrsim 5$ atm , and a composition of 10% CO_2 in volume mixing ratio.

Finally, we note that 1D radiative transfer should be used with care. Climate and atmospheric properties are extremely sensitive to processes that cannot be reproduced in 1D models. Clouds is also a phenomenon that cannot be treated quantitatively in 1D models and that can affect dramatically the surface temperature, and the distribution of the atmospheric species (see e.g., Sing et al. 2016).

Chapter 3

Röntgen spheres around active stars

3.1 The influence of stellar X-rays on the star environment

X-rays may be an important component in the energy balance of (exo-)planetary atmospheres, in particular for hydrogen-rich close-in planets (Cecchi-Pestellini et al. 2009; Shematovich et al. 2014). Such energy source can induce temperatures of around 10,000 K, conducive of planetary mass loss (e.g., Lammer et al. 2003). Close-in exoplanets are thus expected to harbour extended atmospheres and in some cases lose mass with estimated atmospheric evaporation rates as high as $\sim 4.5 \times 10^{12}$ g s^{-1} (Schröter et al. 2011). High energy stellar irradiation may be also relevant for the chemistry – and the related question of potential prebiotic evolution – in possibly habitable planets embedded in a highly energetic radiation environment (e.g., Smith et al. 2004).

Furthermore, the understanding of physical processes in the circumstellar environment of protostars and young stars provides crucial information on how disks and planets form and survive (e.g., Williams & Viti 2014). These processes and star formation itself are regulated by a variety of feedback mechanisms, such as direct and dust reprocessed radiation pressure, photo-ionization flows, stellar wind, and supernova explosions. The response of gas gives rise to complicated chemistry and dynamics, as well as radiation fields, that in turn perturb the behavior of the molecular gas, affecting the chemistry (e.g., Bradford et al. 2011), and impacting the efficiency of star formation (e.g., Dale & Bonnell 2011). Since a tremendous number of stars are observed to be X-ray emitters in nearby star-forming regions (Feigelson 2010), an important question is whether and how X-ray radiation participates in the process

of star, disk, and planet formation and in their evolution. Although X-ray luminosity is relatively small fractions of the bolometric luminosity, such radiation effectively penetrates and ionizes otherwise neutral molecular gases and may even melt solid dust particles.

X-ray emission has been detected in the most massive Wolf-Rayet and OB stars as well as in low-mass M dwarf stars, in compact objects and even in some sub-stellar mass brown dwarfs. X-ray luminosities range from 10^{25} up to 10^{35} erg s^{-1} (e.g., in Eta Carina, Hamaguchi et al. 2014). In low-mass stars X-ray emission is produced by the violent heating of the stellar corona through magnetic dynamo and magnetic reconnection, while in high-mass O and early B-type stars, supersonic shocks in the stellar winds generate X-rays on both stellar and parsec scales. In young solar-like stars, X-ray flares with luminosities orders of magnitude more powerful than seen in the contemporary Sun are frequently observed.

In fact, studies of stellar proxies for the Sun have shown that young solar-type stars emit X-rays at a level three to four orders of magnitude higher than the present-day Sun, both during the pre-main sequence phase when the emission is dominated by intense daily or weekly flares (Favata et al. 2005), and during the first phases of the main-sequence. From studies of stellar proxies for the Sun, e.g., Ribas et al. (2005), it appears that for a 100 Myr star the integrated fluxes in the extreme ultraviolet are lower than X-rays. The ratio of these fluxes remains within a factor of 2 for stars as old as 1 Gyr, while in the Sun is about 4. Moreover the star luminosity seems to be characterized by evolutionary time-scales that are different in different spectral bands (Micela 2002). The X-ray luminosity evolution of M stars is slower than that of G stars, and may present frequent flaring activity. Even if the ratio between X-ray and bolometric luminosities is typically larger in M stars than in solar-type stars, the absolute value of the X-ray luminosity is lower at each age.

The effects of X-rays can be wide ranging or relatively local. Soft X-rays are absorbed closer to the source than X-rays with energy greater than 1 keV. The absorption cross-section of hard X-rays are generally very small, so that such radiation may affect a whole galaxy to some extent. The interaction of X-rays with gas clouds has been widely studied in the literature. The first detailed studies of X-ray illuminated regions were performed by Tarter et al. (1969) and Tarter & Salpeter (1969) for optically thin and thick media, respectively. These authors assumed the spectral shape of thermal bremsstrahlung. It soon become apparent that high energy flat spectra would induce ionization profiles significantly smoother than the sharp boundary between HII and HI regions (Strömgren sphere) produced by standard stellar black body-like emission (see Bahcall et al. 1971). Since then, following the opening of the X-ray Universe the modeling of regions exposed to X-rays was extended

to molecular gas in a variety of sources such as active galactic nuclei, and molecular clouds with embedded among others massive and pre-main sequence (PMS) stars (e.g., Maloney et al. 1996). Depending on specific effects X-ray illuminated regions have been termed X-ray dominated regions when the thermo-chemical balance of the gas is involved (e.g., Tiné et al. 1997), or Röntgen spheres (Lorenzani & Palla 2001) to indicate the extent of the X-ray "sphere of influence" on the ionization balance around a source.

As most star formation in our galaxy occurs within embedded clusters, the radiative and mechanical energy injections produced by cluster members can shape the background environment and thereby provide a feedback mechanism. There is now a wealth of information on embedded clusters coming from multi-wavelength observations, such as far- and extreme-ultraviolet (Hollenbach & Gorti 2009; Holden et al. 2011), and X-rays (Adams et al. 2012). In the first case a significant fraction of the luminosity is produced by the most massive members of the cluster (e.g., Fatuzzo & Adams 2008), while in the X-ray band the total luminosity may be globally contributed by the totality of stars. Frequently, background radiation fields in the ultraviolet can dominate even locally, leading as a result to the evaporation of circumstellar disks, thus decreasing the planet-forming rate within a cluster. On the contrary, mass loss due to X-rays is dominated by the radiation flux from the central star, with the exception of the outer regions in geometrically thin and optically thick disks where background cluster dominates (see Adams et al. 2012). In addition there is a diffuse background ionization level generally exceeding the one generated by cosmic-ray energy deposition (Lorenzani & Palla 2001). These elevated ionization rates deriving from the merging of individual Röntgen spheres, suggest that X-rays can affect ionization, chemistry, and heating in the material between young stellar objects.

In this chapter we study the X-ray environment of stars of different spectral types and age either isolated and clustered, we consider two representative environments, the Cygnus OB2 association, among the most massive clusters in our Galaxy, containing over 1000 OB stars and 3 Wolf-Rayet (Wright et al. 2015a and citations therein), has motived the recent 1.08 Msec Chandra Legacy Project (Drake et al., in preparation) identifying over 7500 members down to low mass with an incomplete census at both high and low mass (Guarcello et al. 2013; Wright et al. 2014, Kashyap et al. 2018, submitted), and the Orion Nebula Cluster (ONC) that was the first cluster of PMS stars to be detected in the X-ray band (Giacconi et al. 1972). The *Chandra Orion Ultradeep Project* (COUP, Getman et al. 2005) has shown that ONC contains more than 1600 X-ray sources, approximately 1400 of which are young stellar objects.

In the next section we solve the appropriate radiative transfer problem, and we derive equations for the ionization rates considering photo-ionization, the Auger effect, and the production of secondary electrons through electronic impacts. In §3.3 we revise the concept of Röntgen sphere, while in §3.4 we modify the description of the ionization balance in circumstellar regions allowing for the presence of stellar ultraviolet irradiation. Results for massive stars are reported in §3.5, while an analysis of the effects on circumstellar gas around low mass stars is in §3.6.

3.2 X-ray transfer and energy deposition

X-rays impinging upon a cloud of gas and dust of solar-like composition photo-ionizes the gas producing a flux of high energy photo-electrons, which deposit their energy into the gas, and to some extent in the interior of dust particles. In a partially neutral medium, electrons ionize, excite, and dissociate atomic and molecular species, as well as heat the gas through Coulomb collisions. Such energy deposition events may be estimated considering all the possible degradation histories of the energetic electron cascade. The derived yields allow to determine the ionization, dissociation, excitation, and heating rates throughout the illuminated region (Dalgarno et al. 1999).

3.2.1 Radiative transfer

We consider 1D geometry in which a stratified cloud consisting of gas and dust is illuminated by a radially incident X-ray photon flux. This flux at distance r from the stellar source is given by the solution to the radiative transfer problem

$$\mathcal{F}_{\rm X}(E,r) = \frac{\mathcal{L}_{\rm X}(E)}{4\pi r^2} \times e^{-\tau(E,r)} \tag{3.1}$$

where $\mathcal{L}_{\rm X}$ is the stellar X-ray spectral luminosity (in ergs s^{-1} eV^{-1}), and $\tau(E,r)$ the optical depth that depends on the total photo-ionization cross-section.

We adopt relativistic photo-ionization cross-sections of individual elements ($Z \leq 30$) and their ions computed by Verner & Yakovlev (1995). In the case of molecular hydrogen we fit the laboratory measurements reported in Samson & Haddad (1994), while for H_2^+ we adopt the calculations by Morita & Yabushita (2008). For heavy elements bound in molecules or molecular ions, the X-ray absorption cross-sections can be obtained approximately by

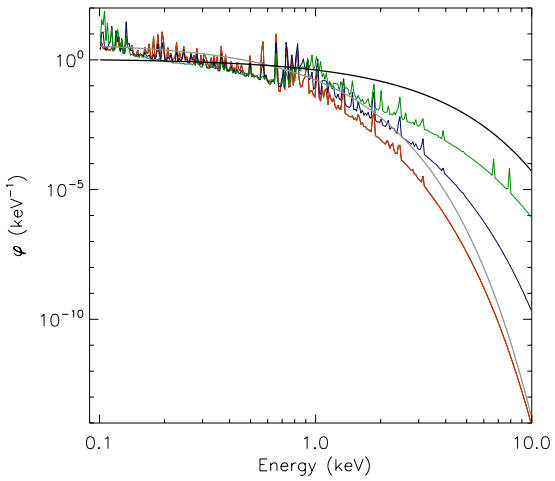

Figure 3.1: Spectral shapes as functions of the photon energy. Thermal plasma models: red (P03), blue (P05), and green (P10) lines. Thermal bremsstrahlung models: grey (B03), and black (B10) lines. For energies lower than ~ 0.1 keV all the fields are assumed to rapidly fade.

adding the atomic cross-sections. As far as the computation of the photoelectric cross-section is concerned we may construct the total cross-section by weighting the individual cross-sections σ_k with element abundances, Y_k, subtracted by the fractions of those elements locked into dust, δ_k

$$\sigma_{\rm h}^{\rm (g)}(E) = \sum_k Y_k \, (1 - \delta_k) \, \sigma_k(E) \tag{3.2}$$

where

$$\sigma_k(E) = \sum_i \sigma_{k,i}(E) \tag{3.3}$$

is the sum of the contributions of the various shells in the atoms. In computing $\sigma_k(E)$ we should take into account that the $k-$th element is in various ionization stages. In practice we consider only neutral atoms, and at most double-charged ions because highly charged ions undergo fast charge exchange reactions

$$Y_k \sigma_{k,i}(E) = Y_{k^0} \sigma_{k^0,i}(E) + Y_{k^+} \sigma_{k^+,i}(E) + Y_{k^{2+}} \sigma_{k^{2+},i}(E) \tag{3.4}$$

with $Y_k = Y_{k^0} + Y_{k^+} + Y_{k^{2+}}$. Heavy elements composing dust grains provide a similar

contribution

$$\sigma_{\rm h}^{\rm (d)}(E) = \sum_k Y_k \delta_k \sigma_k(E) \tag{3.5}$$

To the aim of computing the optical depth the separation in gas- and solid-phase elements is immaterial, while it is not for the calculation of the total ionization rate, because a fraction of the electrons is not ejected into the gas-phase after being released in the interior of a dust grain (see §3.2.2).

For $E \gtrsim 5$ keV Compton ionization is more efficient than photo-ionization (Yan et al. 1998). Unlike photo-ionization or fast charged particle scattering, total cross-sections for single ionization via Compton scattering (also termed incoherent scattering) are usually largely independent of atomic properties, such as geometric sizes of atoms, and electron correlation. In Compton ionization, the photon is not absorbed but scattered, and it shares energy and momentum with the ejected electron. At high energies the binding energies of electrons in atoms or molecules can be ignored, and the cross-sections are those for scattering by free electrons. For energies higher than 1 keV the incoherent cross-section for atomic hydrogen is approximately the same as the free electron Klein-Nishina cross-section, $\sigma_{\rm KN}$. Moreover, scattering cross-sections are very small, in fact of the order of the electron Thomson scattering cross-section, $\sigma_{\rm Th}$ ($\sim 1\,{\rm b} = 10^{-24}$ cm^2). Thus, in the computation of the optical depth we use for all species the Klein-Nishina scattering formula (Rybicki & Lightman 1985) in the non-relativistic regime ($E \ll mc^2$)

$$\sigma_{\rm C}(E) = \mathcal{Z} \times \sigma_{\rm Th}\left[1 - \frac{E}{mc^2} + \frac{26}{5}\left(\frac{E}{mc^2}\right)^2\right] = \mathcal{Z} \times \sigma_{\rm KN} \tag{3.6}$$

where

$$\mathcal{Z} = 1 + 2Y_{\rm He} + \sum_k Z_k Y_k \tag{3.7}$$

$Y_{\rm He}$ being the fractional total helium concentration, and Z_k the number of electrons in the $k-$th species. In equation (3.7) we implicitly assume that the incoherent cross-section of molecular hydrogen is twice the one for atomic hydrogen (cf. equation 3.8), and all the elements are in neutral form. The correct formulation of non relativistic Compton ionization cross-sections for H, H_2, and He (Jackson 1975) is included in the calculation of the total ionization rate of the gas. Here, we report the expression

$$\sigma_{\rm C}^{(i)}(E) = \frac{3n_e^{(i)}}{8}\sigma_{\rm Th}\left(4/3 + t + t^3/3\right) \tag{3.8}$$

where $t = 1 - mc^2/E \times x^{(i)}/(1 - x^{(i)})$, $x^{(i)} = \mathcal{I}^{(i)}/E$. In the previous expression $i = 1$, 2 and 3 for H, H_2, and He, respectively; $n_e^{(i)}$ is the number of electrons equal to 1, 2, and 2, and $\mathcal{I}^{(i)} = 13.6$, 15.4, and 24.6 eV, the ionization potential. Finally, the cross-section thresholds are 1.87, 1.99, and 2.51 keV.

The energy-dependent optical depth results

$$\tau(E) = \sigma_{\rm T}(E)\, N_{\rm H} = (f_1\sigma_{\rm H} + f_2\sigma_{\rm H_2} + Y_{\rm He}\sigma_{\rm He} + \\ + Y_{\rm He^+}\sigma_{\rm He^+} + \sigma_{\rm h} + \sigma_{\rm C}) \times N_{\rm H} \tag{3.9}$$

in which $\sigma_{\rm h} = \sigma_{\rm h}^{\rm (g)} + \sigma_{\rm h}^{\rm (d)}$, $N_{\rm H}$ is the total hydrogen column density, and f_1 and f_2 are the fractional abundances of atomic and molecular hydrogen, respectively ($f_1 + 2 \times f_2 \sim 1$).

In Figure 3.2 we compare the approximate cross-section given in Lorenzani & Palla (2001)

$$\sigma_{\rm A}(E) = \overline{\sigma} \times (\nu/\nu_{\rm X})^{-n} = 2.16 \times 10^{-4} (E/1{\rm keV})^{-2.51}\,{\rm Mb} \tag{3.10}$$

with our computed $\sigma_{\rm T}$ in various configurations, and the contribution due to Compton ionization plotted separately. We adopt the solar abundances reported in Asplund et al. (2009), and we set $Y_{\rm He} = 0.085$.

3.2.2 X-ray ionization

Primary X-ray ionization is given by the following relation

$$\varsigma'_{\rm X} = \sum_k \sum_i \int_{E_{k,i}}^{E_{k,i+1}} \frac{\mathcal{F}_{\rm X}(E,r)}{E} \left[Y_k \sigma_{k,i}(E) + \sigma_{\rm C}(E)\right] dE \tag{3.11}$$

where $E_{k,i}$ is the energy threshold, $i = 1$, 2, and 3 identifies M, L, and K shell, respectively, and $E_{k,4} = \infty$. Here the sum over k includes H, He, He^+, H_2, and H_2^+ in addition to heavy elements. Furthermore, the Compton contribution has been modified to incorporate the non approximate cross-sections given in equation (3.8)

$$\sigma_{\rm C} = \sum_{j=1}^{3} f_j \sigma_{\rm C}^{(j)}(E) + (\mathcal{Z} - 1 - 2Y_{\rm He}) \times \sigma_{\rm KN} \tag{3.12}$$

where $f_3 = Y_{\rm He}$ is the total helium abundance with respect to hydrogen.

The product of a primary ionization is one fast photo-electron, or more if the Auger

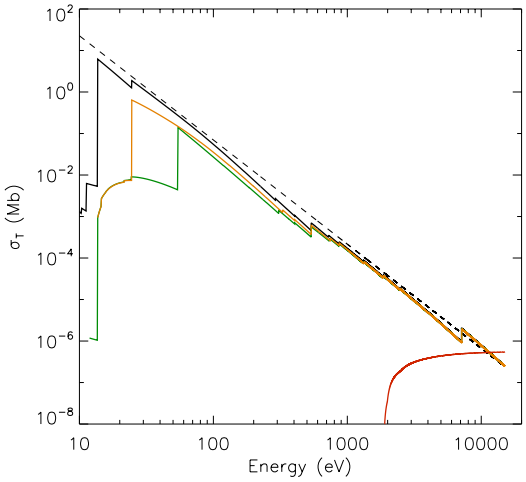

Figure 3.2: Total photo-ionization cross-section in Mb (1 Mb $= 1 \times 10^{-18}$ cm^2) as a function of the energy of the incoming photon in eV, for a gas with solar abundances (Asplund et al. 2009). Black solid line: neutrals; yellow line: singly-ionized species; green line: double charged ions. The red solid line represents the Compton ionization cross-section, equation (3.12), the thin dashed line the approximate photo-ionization cross-section given in Lorenzani & Palla (2001), equation (3.10).

effect occurs, that gives rise to a cascade of secondary ionizations. The energy of the fast photo-electron is given by the difference of the energy of the incident photon and the energy threshold $E_{k,i}$ of the ejected electron. The rate of secondary ionization of the $k-$th element due to photo-electrons is given by the relation

$$\varsigma_k'' = \int n_{\rm sec}(E) v(E) \sigma_k^{(e)}(E) dE \tag{3.13}$$

(e.g., Ádámkovics et al. 2011) where $v(E)$ is the electron speed, $n_{\rm sec}(E)$ the absolute number distribution of secondary electrons, and $\sigma_k^{(e)}$ the electron impact ionization cross-section. We estimate equation (3.13) by means of the semi-empirical relation

$$\varsigma_k'' = \sum_i \int_{E_{k,i}}^{E_{k,i+1}} \frac{\mathcal{F}_{\rm X}(E,r)}{E} Y_k \sigma_{k,i}(E) \frac{(E - E_{k,i})}{W} dE \tag{3.14}$$

with W the mean energy per ion pair (e.g., Dalgarno et al. 1999), which is the initial energy of the photo-electron divided by the number of secondary ionizations produced as the particle

comes to rest. To include Auger ionization, we have to supplement equation (3.14) with

$$\varsigma_k^A = \sum_i \int_{E_{k,i}}^{E_{k,i+1}} \frac{\mathcal{F}_{\rm X}(E,r)}{E} Y_k \sigma_{k,i}(E) \frac{\mathcal{E}_{k,i}}{W} dE \tag{3.15}$$

where $\mathcal{E}_{k,i}$ is the energy of the Auger electron emitted by the $i-$th shell of the $k-$th element. However, assuming that the Auger electrons contribute to the ionization with an energy $\mathcal{E}_{k,i}$ comparable with the energy $E_{k,i}$ (Maloney et al. 1996), the total secondary ionization reads as

$$\varsigma''_{\rm X} = \sum_k \sum_i \int_{E_{k,i}}^{E_{k,i+1}} \mathcal{F}_{\rm X}(E,r) \left(\frac{Y_k \sigma_{k,i}(E)}{W} \right) dE \tag{3.16}$$

To take into account heavy elements locked into dust grains we slightly modify the fraction in the integrand in equation (3.16) as follows

$$\begin{aligned} \frac{Y_k \sigma_{k,i}(E)}{W} \rightarrow \frac{Y_k (1-\delta_k) \sigma_{k,i}(E)}{W} + \\ + \frac{Y_k \delta_k \sigma_{k,i}(E)}{W} \times \frac{H(E-E_g, E_{k,i})}{E} \end{aligned} \tag{3.17}$$

where E_g is the energy loss within the grain, that depends on the grain size and materials, and $H(x,y) = 0$ when $x \leq y$, and equal to x $(= E - E_g)$ oherwise. We compute E_g using the range of electrons in silicate and carbon materials taken in the NIST *ESTAR* database[I].

equation (3.16) is supplemented by Compton ionization as

$$\varsigma''_{\rm X,C} = \int_{E_i}^{\infty} \frac{\mathcal{F}_{\rm X}(E,r)}{E} \times \frac{\sigma_{\rm C}(E)\, E_{\rm C}(E)}{W} dE \tag{3.18}$$

with $E_i = 1.87$ keV, and $E_{\rm C}(E)$ the energy of the released Compton electron. In the Compton energy domain an emitted photon will scatter until, in a finite medium it escapes completely. The number of scattering acts is approximately $\mathcal{N}_s \approx \max(\tau_{\rm C}, \tau_{\rm C}^2)$ (Rybicki & Lightman 1985) with $\tau_{\rm C}$ the Compton optical depth. The Compton parameter $y_{\rm C}$ is defined as the number of scattering events times the average fractional change of energy per scattering $y_{\rm C} \sim \mathcal{N}_s \times (E/mc^2)$. We thus approximate the energy of the released Compton

[I] http://physics.nist.gov/PhysRefData/Star/Text/ESTAR.html

electron as

$$E_{\rm C}(E) = \begin{cases} y_{\rm C} E & y_{\rm C} < 1 \\ E & y_{\rm C} > 1 \end{cases} \tag{3.19}$$

For the calculation of secondary ionization, we compute W as a function of the energy of the primary photo-electron for a mixture of H, He and H_2 exploiting the numerical code described in Cecchi-Pestellini et al. (2006). We follow the chain of discrete energy deposition events using the method put forward by Cravens et al. (1975). We adopt the electron impact cross-sections for excitation, ionization, dissociation, and elastic collisions listed in Dalgarno et al. (1999). To include the contribution of the heavy elements that are not traced by equation (3.16) we rely on an approximate treatment that makes use of the relative rather than the absolute secondary energy distribution (Maloney et al. 1996). Following Ádámkovics et al. (2011) we estimate the secondary ionization rates for the individual heavy elements using the ratio of the peaks of the ionization cross-sections for electronic impact $\sigma^{(e)}$

$$\varsigma''_k = \frac{\sigma^{(e)}_k}{\sigma^{(e)}_{\rm H}} \varsigma''_{\rm X} \tag{3.20}$$

where k counts heavy elements, and $\varsigma''_{\rm X}$ is the rate given in equation (3.16). Values of the cross-section ratios for neutral atoms are taken in Bartlett & Stelbovics (2004), and reported in Table 3.1. Unfortunately, these authors do not include ions. Although double charged atomic ions have in general negligible abundances because of rapid charge exchange with atomic and molecular hydrogen and other species, singly-ionized atoms may be abundant. We estimate the cross-section ratios for these species exploiting the data reported in Ádámkovics et al. (2011), that have been derived using much older data by Tarawa & Kato (1987). We perform a linear fit of the relation between $\hat{R}_1$ and the geometrical mean $\sqrt{\hat{R}_1 \times R_2}$ in which $R_1 = \sigma^{(e)}_k / \sigma^{(e)}_{\rm H}$ for neutrals, $\hat{R}_1$ the normalization to its maximum value, and $R_2 = \sigma^{(e)}_{k^+} / \sigma^{(e)}_{\rm H}$ the ratio for ions. While the overall fit is not particularly good, it is difficult to evaluate the accuracy of the approximate formula, equation (3.20), in the absence of a direct calculation of the secondary electron distribution.

If the gas has a significant molecular component the previous treatment is invalid. Electron impact ionization cross-sections for simple molecules such as water or carbon monoxide have a threshold around 20 eV, they show a broad maximum at approximately 100 eV, and then they decline to reach roughly their values at the threshold around 1 keV (e.g., Hudson et al. 2004). Such a description needs to be included above and beyond the ionization front.

Table 3.1: Peak Electronic Ionization Cross-sections in Mb

element	$\sigma_k^{(e)\S}$	$R_1^\dagger$	$R_2\ddagger$	$R_1^\star$	$R_2^\star$
H	88.7	1.0			
C	211.3	2.38	0.89	3.4	0.82
N	146.9	1.66	0.84	2.2	0.75
O	143.0	1.61	0.84	2.2	0.67
Ne	73.10	0.82	0.89	1.1	0.48
Na	490.6	5.53	1.29	7.3	0.40
Mg	529.1	5.96	1.36	7.91	0.64
Al	827.1	9.32	1.27		
Si	715.0	8.06	1.66	10.0	2.3
S	541.3	6.10	1.38	6.7	2.1
Cl	420.5	4.74	0.93		
Ar	327.8	3.69	1.05	3.7	1.8
K	852.1	9.6	1.88	13	1.5
Ca	873.3	9.85	1.31		
Fe	494.1	5.57	1.30	8.0	1.6

§ peak of the electron impact ionization cross-section for $k-$th species, Bartlett & Stelbovics (2004); † $R_1 = \sigma_k^{(e)}/\sigma_{\rm H}^{(e)}$, Bartlett & Stelbovics (2004); ‡ $R_2 = \sigma_{k^+}^{(e)}/\sigma_{\rm H}^{(e)}$, this work; ⋆ Ádámkovics et al. (2011);.

The presence of free electrons in the gas with a fractional content exceeding 1% impacts substantially on the ionization, excitation, and dissociation rates because of energy loss by Coulomb collisions. As the fractional ionization increases the mean energy for ion couple increases as well, and eventually all the initial electron energy is converted into heat, with negligible residual inelastic rates.

Finally, the total ionization rate is found by adding primary and secondary ionizations

$$\varsigma_{\rm X} = \varsigma'_{\rm X} + \left(1 + \sum_k Y_k \frac{\sigma_k^{(e)}}{\sigma_{\rm H}^{(e)}}\right) \times \left(\varsigma''_{\rm X} + \varsigma''_{\rm X,C}\right) \tag{3.21}$$

where the sum includes only the contribution of heavy elements, and $Y_k\sigma_k^{(e)}(E) = Y_{k^0}\sigma_{k^0}^{(e)}(E) + Y_{k^+}\sigma_{k^+}^{(e)}(E)$.

3.3 The Röntgen sphere

As first application of the formalism developed in the preceding Sections we revisit the concept of Röntgen sphere. According to Lorenzani & Palla (2001) these environments are defined as circumstellar regions in which the ionization rate due to X-rays exceeds the background level provided by cosmic rays, $\varsigma_{\rm cr}$. Generally, in molecular clouds the ionization impact of cosmic rays is quantified by the number of H_2 ionization per second produced by cosmic ray impacts. Such a quantity has been through the years observationally estimate to range from a few 10^{-18} s^{-1} to a few 10^{-16} s^{-1} in diffuse and dense interstellar clouds (Galli & Padovani 2015, and references therein). Here, we assume for the total cosmic ray ionization rate the approximately median value $\varsigma_{\rm cr} = 1 \times 10^{-16}$ s^{-1} per hydrogen nucleus.

The size of the region is called Röntgen radius, $R_{\rm X}$, and in the original formulation it is derived using the approximate relation

$$\varsigma_{\rm cr} = \frac{1.7\,\overline{\sigma}}{\langle W \rangle} \int_{E_0}^{\infty} \mathcal{F}_{\rm X}(E, R_{\rm X}) \times (E/E_{\rm X})^{-n}\, dE \tag{3.22}$$

where $\langle W \rangle = 0.035$ keV is a reasonable representative value for the mean energy for ion couple in a slightly ionized gas with solar abundances (see Dalgarno et al. 1999), $E_0 = 0.1$ keV, $E_{\rm X} = 1$ keV, and the factor 1.7 accounts for the ionization due to secondary electrons. $R_{\rm X}$ is thus weakly dependent on the ratio between the X-ray luminosity defined as

$$L_{\rm X} = \int_{E_0}^{\infty} \mathcal{L}_{\rm X}(E) dE \tag{3.23}$$

and the cosmic-ray ionization rate $\varsigma_{\rm cr}$, $R_{\rm X} \propto \ln(L_{\rm X}/\langle W \rangle \varsigma_{\rm cr})$, for $R_{\rm X} \leq (1.7\sigma_{\rm A}(E_0)/4\pi\langle W \rangle \times L_{\rm X}/\varsigma_{\rm cr})^{1/2}$. Thus, any increase of the cosmic-ray ionization rate, even above and beyond its characteristic figure in the cold neutral medium, $\varsigma_{\rm cr} = 1 \times 10^{-16}$ s^{-1}, results in just a modest decrease in $R_{\rm X}$.

$R_{\rm X}$ is weakly sensitive to the actual shape of the X-ray spectrum, and directly dependent on the total X-ray luminosity. In the optically thin regime it does not vary with density, while decreases with increasing density otherwise. To simulate spectra differing significantly in shape, we adopt models for the thermal emission of hot plasmas with energies 0.3 (P03), 0.5 (P05), and 1 keV (P10) derived by Raymond & Smith (1977). These spectra are largely dominated by lines, and over-sampled with respect to the scope of this work. Thus, we bin them and derive the average number of photons in each bin. Defining the original spectrum

as $s(E)$ (photons s^{-1}), and integrating it over the $j-$th energy bin of the set $\{\Delta E_k\}$ we get

$$\mathcal{S}_j = \frac{1}{\Delta E_j} \int_{\Delta E_j} s(E) \mathrm{d}E \quad \text{photons}\,\mathrm{s}^{-1} \tag{3.24}$$

corresponding to the mean energy E_j (e.g., in eV) falling in the middle of ΔE_j. As consequence the energies are related through the expression $E_{j+1} = E_j + (\Delta E_j + \Delta E_{j+1})/2$. In the following we indicate the binned spectrum as $\mathcal{S}(E)$. The X-ray spectral luminosity results

$$\mathcal{L}_{\mathrm{X}}(E) = L_{\mathrm{X}} \times \frac{\mathcal{S}(E)}{\displaystyle\int_{\Delta E} \mathcal{S}(E) \mathrm{d}E} = L_{\mathrm{X}} \times \varphi(E) \tag{3.25}$$

where $\varphi(E)$ is the spectral shape. For comparison with the original calculation by Lorenzani & Palla (2001), in the following we shall also consider thermal bremsstrahlung spectra at different plasma temperatures, 0.3 (B03) and 1 kEV (B10). Spectral shapes are shown in Figure 3.1 assuming single temperature thin thermal plasma models. All the fields are assumed to decrease sharply below $E_0 = 0.1$ keV (e.g., Nomura et al. 2007).

In Figure 3.3 we show R_{X} as a function of the ratio $L_{\mathrm{X}}/\varsigma_{\mathrm{cr}}$, for some choice of the hydrogen number density. The Röntgen radius has been derived through the use of the relation $\varsigma_{\mathrm{X}}(R_{\mathrm{X}}) = \varsigma_{\mathrm{cr}}$, with ς_{X} defined in equation (3.21). When $L_{\mathrm{X}}/\varsigma_{\mathrm{cr}} \geq 1 \times 10^{46}$ erg, R_{X} differs from that derived following the prescription of Lorenzani & Palla (2001), equation (3.22), by a factor around 2, corresponding to about one order of magnitude in volume. Increasing the gas density Röntgen radii decline roughly as $n_{\mathrm{H}}^{1/2}$. Optical depth effects tend to remove rapidly the soft component of the spectrum as soon as $n_{\mathrm{H}} \geq 10^6$ cm^{-3}. As a consequence the hardest spectral shapes (P10 and especially B10 models) produces more extended Röntgen radii than softer spectral profiles, although averaging over the volume ionization rates may results lower (see §3.6). Finally, in partially ionized regions R_{X} does not vary appreciably with the electron concentration n_e as long as the fractional ionization n_e/n_{H} lays below 1%. For higher values the degree of ionization falls rapidly as Coulomb dissipation dominates the energy loss of the secondary electron cascade.

3.4 Ionization Structure

Until now we considered X-rays impacting on a neutral gas. However, around hot stars the environment is also subjected to intense ultraviolet irradiation. We therefore extend our

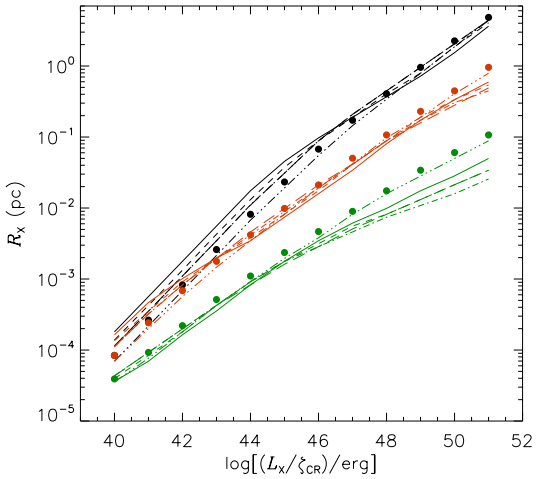

Figure 3.3: The Röntgen radius R_X as a function of the ratio of the X-ray luminosity L_X and the cosmic-ray ionization rate ς_{cr}, for three values of the gas density $n_H = 10^2$ (black), 10^4 (red), and 10^6 cm^{-3} (green). For each density we have used the spectral shapes described in Figure 3.1: B03 (long dashed), B10 (dot-dot-dot-dashed), P03 (dot-dashed), P05 (short-dashed), and P10 (solid). Filled circles indicates values of the Röntgen radius obtained using the approximate relation derived by Lorenzani & Palla 2001, equation (3.22).

description of radiative transfer to include such spectral range.

Since the region is clearly overpressurized due to photo-ionization, an ionized nebula cannot exist in static equilibrium with its shape and density strongly dependent on the initial distribution of the circumstellar neutral gas. In many cases the energetics is dominated by radiation fields with negligible mechanical energy conversion into radiation, and the size of the region is determined in all cases by the balance between ionizations and recombinations to the ground state of atomic hydrogen. However, the dynamical time-scales are much longer than those associated with microscopic processes, so that it is reasonable to assume the region as static. For the sake of simplicity we also assume spherical envelopes in thermal and ionization equilibrium. This latter usually applies, although there may be cases in which departures from equilibrium are expected such as e.g., in the impact of ionization fronts on turbulent clouds (Tremblin et al. 2012). This occurs because of mixing of some ionized gas into the shadow of dense neutral gas in the transition zone.

Since the 1960s (e.g., Hummer & Seaton 1963), the ionized structure of circumstellar gas has been extensively studied. As usual we split the radiation field into two components, the attenuated direct stellar radiation and the diffuse component, and we exploit the so-called

on-the-spot approximation in a dusty plasma, that consists in imposing that the hydrogen diffuse radiation field is locally absorbed only by hydrogen and dust and the helium radiation field only by helium and dust. This removes the transfer problem for diffuse radiation, and the ionization structure is thus determined by a single integration step, while the complete solution would require an iterative procedure. The equations of ionization equilibrium can be cast in a differential form for the column densities of neutral hydrogen, $j = 1$, and neutral, $j = 2$ and singly-ionized helium, $j = 3$

$$\frac{1}{Y_j n_{\rm H}} \frac{dN_j}{dr} = \frac{n_e K_j}{n_e R_j + \int_{m_j \mathcal{I}^{(1)}}^{\infty} \sigma_j(E) \left[\mathcal{F}(E,r)/E\right] dE} \tag{3.26}$$

where $Y_1 = 1$, $Y_2 = Y_3 = Y_{\rm He}$, n_e is the electron number density, K_j the total recombination coefficient for the $j-$th species, $\mathcal{F}(E,r)$ the total radiation field including the diffuse component, and $m_j = 1$, 1.807, and 4 for $j = 1$, 2, and 3 respectively. Using the notation introduced in §3.2.2 equations (3.26) read as

$$\frac{dN_j}{dr} = \frac{Y_j n_{\rm H}}{1 + (\varsigma_j / K_j n_e)} \tag{3.27}$$

where $\varsigma_j = \varsigma_{\rm UV}^{(j)} + \varsigma_{\rm X}^{(j)}$ is the ionization rate per species j including both (extreme) ultraviolet and X-ray photo-ionization processes. Equations (3.27) are complemented by the closure relation for the number densities of charged species

$$n_e = n_{\rm H^+} + n_{\rm He^+} + 2 n_{\rm He^{2+}} \tag{3.28}$$

Such equations are coupled through the optical depth, equation (3.9), extended to lower frequencies to include the ultraviolet portion of the spectrum.

The dust contribution to the optical depth in the ultraviolet range is computed by means of the cross-section

$$\sigma_{\rm d}(\nu) = \frac{\delta_{\rm d} R_V}{1.086} \frac{E_{B-V}}{N_{\rm H}} \left(\frac{A_\nu}{A_V}\right) \sim 4.65 \times 10^{-4} \delta_{\rm d} \left(\frac{A_\nu}{A_V}\right) \text{ Mb} \tag{3.29}$$

where $\delta_{\rm d}$ is the depletion factor, $R_V = A_V / E_{B-V}$ the total to selective extinction, and E_{B-V} the color excess related to the total hydrogen column density $N_{\rm H}$ through the gas-to-dust ratio $N_{\rm H} = \mathcal{R}_{\rm gd} \times E_{B-V}$. In the calculation we used as fiducial value $\mathcal{R}_{\rm gd} = 6.12 \times 10^{21}$ cm^{-2} mag^{-1} (Gudennavar et al. 2012), and we set $R_V = 3.1$; $\delta_{\rm d} = 1$ corresponds to

Table 3.2: Stellar properties

star type	$Q_{\rm H}$ (ph s^{-1})	$T_\star$ (K)	$R_\star$ ($R_\odot$)	$L_{\rm bol}$ ($L_\odot$)	$M_\star$ ($M_\odot$)
B	1.3×10^{48}	30,500	7.47	2.0×10^4	15.8
O	8.9×10^{49}	47,000	17.2	5.0×10^5	39.8
WR	1.1×10^{49}	160,000	0.57	2.0×10^5	8.8

the average Galactic gas-to-dust mass ratio ~ 100 (e.g., Draine 2003). Dust extinction in the extreme ultraviolet cannot be measured directly. However, we can reasonably estimate dust attenuation by extrapolating the extinction in the far-ultraviolet (see the discussion in Tielens 2005). In our computed models the visual extinction adds to $A_V \sim 1$ mag over the ionized region, corresponding to an optical thickness in the extreme ultraviolet of $\sim 3 - 4$ (see e.g., Cecchi-Pestellini et al. 2010).

The coupled equations are integrated using standard techniques (i.e. the Bulirsh-Stoer method). At each radial integration step, we follow the time evolution of the number densities up to the steady state, solving a non-linear algebraic system for the three diffuse fields as in Tielens & de Jong (1979).

3.5 Ionization profiles around massive stars

We consider three representative massive stars (see Table 3.2), as show in Table 1.1, B stars with an effective temperature of about 31000 K have a X-ray luminosity of about 10^{31} erg s^{-1}, while the brighter known X-ray source have a X-ray luminosity of 10^{35} erg s^{-1}, then we run models with X-ray luminosity in the range $L_{\rm X} = 10^{30} - 10^{35}$ erg s^{-1}. For the gas number density in the circumstellar region we choose three values: $n_{\rm H} = 10^2$, 10^4 and 10^6 cm^{-3}. The ultraviolet field is approximated by a black body of temperature $T_\star$, while X-ray fields have been described in §3.3. From now on we shall exploit as reference the P05 spectral shape (see Figure 3.1) unless otherwise stated. Each source is then characterized by three parameters, $Q_{\rm H}$, the number of Lyman continuum photons per second emitted by the star, $T_\star$ the radiation temperature, and $L_{\rm X}$ the X-ray luminosity. We assume that without X-ray radiation the circumstellar region is ionization bounded. The labels O and B indicate two synthetic stars whose properties are reported in Mihalas & Binney (1981), that show

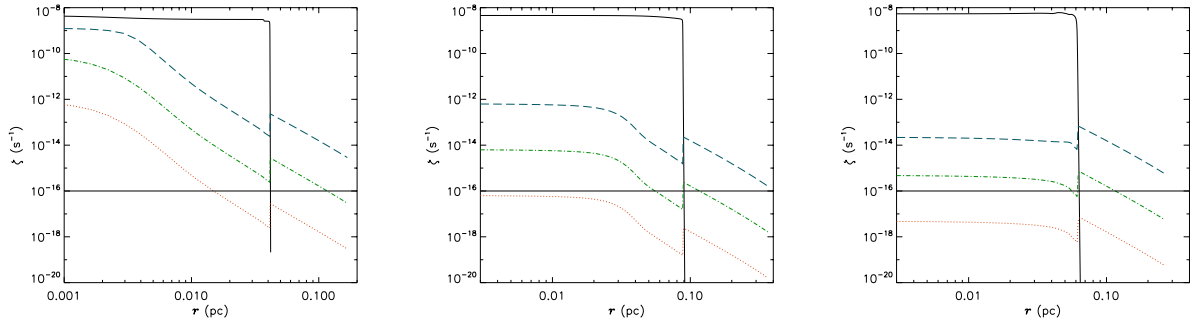

Figure 3.4: Photo-ionization rates as functions of the distance r from the ionizing source in a gas with number density $n_{\rm H} = 10^4$ cm^{-3}. Extreme ultraviolet: solid (black) line; X-rays: $L_{\rm X}$ (erg s^{-1}) = 1×10^{31}, dotted (red) line, 1×10^{33}, dot-dashed (blue) lines, and 1×10^{35}, dashed (purple) lines. The thin black horizontal line indicates the level of the background cosmic-ray ionization rate $\varsigma_{\rm cr} = 1 \times 10^{-16}$ s^{-1}. Left panel: B star; middle panel: O star; right panel: WR star.

approximately characteristics in between O3V and O5V (see e.g., the primary star of the system HD 150136), and B0V stellar types, respectively. The star labelled WR is WR93b, an oxygen sequence Wolf-Rayet star, spectral type WO3, discovered by Drew et al. (2004) in the Scutum-Crux arm of the inner Galaxy. This kind of stars constitute a final stage in massive star evolution, and should conclude their lives as type Ic supernovae. The initial masses have been estimated to be in the range $40 - 60$ $M_{\odot}$ (Tramper et al. 2015). Since WR93b is a rather hot star we include it in our sample to highlight the role of radiation temperature.

In all considered cases the ionization is initially dominated by the ultraviolet field with X-rays taking control in the proximity of the transition zone in which both H^+ and He^+ abundances fall sharply marking the onset of the photon-dominated region, the so-called Strömgren radius $R_{\rm S}$ (Osterbrock & Ferland 2006). When X-ray illumination is included, in the transition region the gas ionization does not follow the sharp fall of the ultraviolet ionization, declining much less steeply as X-rays propagate into the cloud volume creating a Röntgen region, whose extent is determined by the relative weights of the ultraviolet, X-ray, and fast particle components. In the proximity of the Strömgren radius, where hydrogen recombines, the electron fraction drops abruptly, and the X-ray ionization increases in response to the closing of the Coulomb dissipation channel (Figure 3.4). Thus, within the Strömgren region the photo-electron effect is the primary X-ray ionization source.

As it is clear from the results shown in Figure 3.4 in some cases the Röntgen radius is

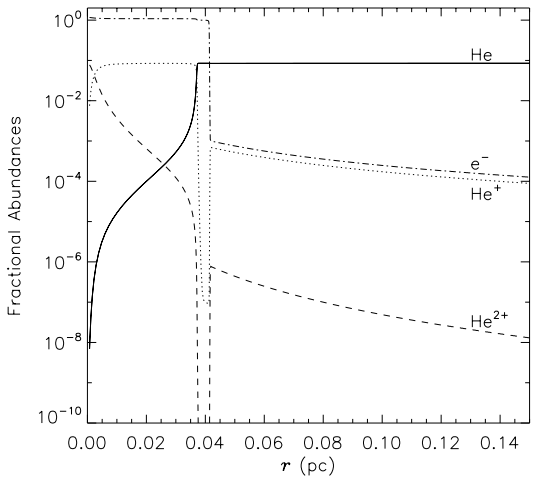

Figure 3.5: Fractional abundances of some members of the Helium family (and electrons) as functions of the distance r from the B star whose properties are reported in Table 3.2. The gas density is $n_{\rm H} = 10^4$ cm^{-3}, and the X-ray luminosity $L_{\rm X} = 1 \times 10^{33}$ erg s^{-1}.

not defined, being lower than the size of the Strömgren region. It is however worthwhile to recall that the Röntgen radius is not an absolute quantity, and it depends on the assumed level of the background cosmic-ray ionization rate.

In the case of O and WR stars for which H recombines before He, ionizations provided by X-rays inflate smoothly the ionized regions of hydrogen, helium, and He^+. In the B star case where the Strömgren radius of the hydrogen is greater than that of the helium, the extra-ionization source affects He only when hydrogen turns neutral. The net effect is a sharp increase of several orders of magnitude in the fractional abundances of He^+ and He^{2+} beyond the Strömgren radius (Figure 3.5).

In Figure 3.6 we plot $R_{\rm eq}$ the distance from the source for which the X-ray ionization rate matches the extreme ultraviolet one ($\sim R_{\rm S}$) against the Röntgen radius for a representative sample of models. In about two thirds of models the stars give origin to Röntgen regions, whose presence depends mainly on the density of the circumstellar medium. When $n_{\rm H} = 10^2$ cm^{-3} only B and WR stars develop Röntgen regions at the highest X-ray luminosity. Increasing the circumstellar gas density, the number of successful models increase but the absolute values of $R_{\rm X}$ decrease. Such behaviour is a clear indication that the increase in the gas density impacts more effectively the extent of the HII region than $R_{\rm X}$. These results upgrade the interpretation of Figure 3.3 in the case of massive stars, as they show that in real

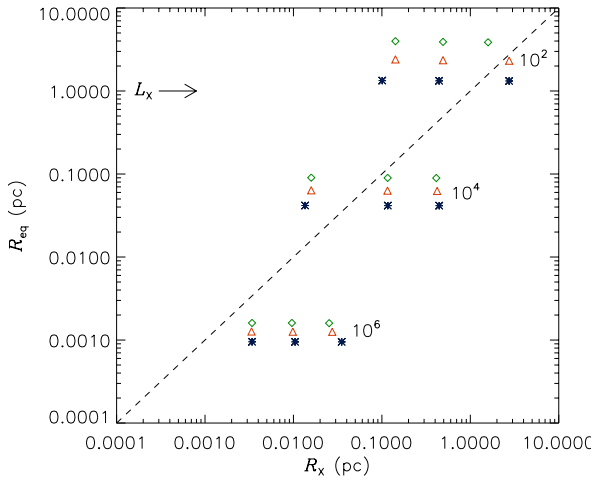

Figure 3.6: $R_{\rm eq}$, the distance from the source for which the extreme ultraviolet and X-ray ionizations are the same, plotted versus the Röntgen radius, $R_{\rm X}$, for B (blue $*$), O (green $\diamond$), and WR (red $\triangle$) stars. Numerical labels indicate the gas number density in cm^{-3}; the selected X-ray luminosities – increasing for each star in the direction of the arrow – are 1×10^{31}, 10^{33}, and 10^{35} erg s^{-1}.

cases although low densities induce large values of the Röntgen radius, $R_{\rm X}$ may be actually indefinite.

The volume averaged ionization rate $\langle \varsigma_{\rm X} \rangle$ increases with the gas number density for all kind of stars, and generally with increasing $R_{\rm X}$ (or $L_{\rm X}/\varsigma_{\rm cr}$). For a gas with $n_{\rm H} = 100$ cm^{-3}, corresponding to the mean number density of a giant molecular cloud at 100 pc scale, there are no relevant effects beyond the Strömgren radius $R_{\rm S}$. In embedding volumes with densities characteristic of clumps $n_{\rm H} = 10^3 - 10^4$ cm^{-3}, the volume averaged ionizations are approximately 10 times the background cosmic-ray ionization when $L_{\rm X} \geq 10^{35}$ erg s^{-1}. These effects occur on spatial ranges $R_{\rm X} \sim 0.5$ pc ($R_{\rm X}/R_{\rm S} \sim 5 - 10$). Increasing further the gas densities within the range characteristic of dense cores the effects may be important, $\langle \varsigma_{\rm X} \rangle \geq 100\ \varsigma_{\rm cr}$, but the size of the interested region is very small, few percent of parsec. Ultimately, the impact of X-rays on the environments of massive stars appears to be rather limited, with the exception of high density regions, such as hot cores.

The above results have been derived using solar metallicities and average Galactic depletions. However, the ionization level depends on the metallicity and the depletion factor $\delta_{\rm d}$ of the star embedding region. These two quantities are related, but for clarity we vary them independently. Their variations impact the results similarly but for different reasons:

X-rays are principally absorbed by metals, while the depletion factor tunes the attenuation of the ultraviolet radiation. A decrease of a factor of 3 in metallicity heightens both the ionization and the extent of the Röntgen radius approximately one order of magnitude. Any increase in the depletion factor leads to higher dust extinctions which decrease the density of the extreme ultraviolet radiation, resulting in an inward shift of the ionization front. As a consequence, X-rays take the control of the gas ionization with higher intensities than in the standard case.

The gathering of a large number of X-ray emitting massive stars might provide a significant contribution to the energetics of the embedding region. An interesting test case is given by the Cygnus OB2 association, one of our Galaxy's most massive star forming regions. Its OB star members, whose number has been estimated to be $\sim$ 200 (Wright et al. 2015b) – see however the much larger value of $\sim$ 2600 given in Knödlseder (2000) – are known to be powerful X-ray emitters. Gredel et al. (2001) derived the lower limit of $Q_{\rm H} = 7 \times 10^{50}$ ionizing photons s^{-1}, able to support a Strömgren sphere of $\sim$ 104 pc at an electron density of $n_e = 34$ cm^{-3} (Downes & Rinehart 1966). Gredel et al. (2001) considered the possibility that strong stellar winds might have cleared out such a large region that the nebula is density-bounded, and thus leaking photons into the surrounding neutral gas, creating a Röntgen sphere. As noted by Drew et al. (2008) the lack of a bright HII region surrounding Cyg OB2 is possible if the clearing has occurred on timescale greater than 5 Myr, consistently with the age distribution inferred from stellar evolutionary models (Wright et al. 2015b). According to our calculations, the configuration needed to provide an X-ray ionization larger than the cosmic-ray level at 100 pc is a gas number density lower than $n_{\rm H} = 20$ cm^{-3}, and an aggregate X-ray luminosity of 3×10^{38} erg s^{-1}, corresponding roughly to an average single star luminosity $\langle L_{\rm X} \rangle \geq 1 \times 10^{35}$ erg s^{-1}, depending on the number of sources in the association. This value is larger than X-ray luminosities inferred for this region ranging between 10^{30} and 10^{31} erg s^{-1} for intermediate-mass and low-mass stars, and between 2.5×10^{30} and 6.3×10^{33} erg s^{-1} for OB stars (Albacete Colombo et al. 2007). This would support the possibility that the region was cleared out by stellar winds (e.g., Gredel et al. 2001), or other dynamical processes (see the discussion in Wright et al. 2015b). The energy deposited by X-rays may be estimated through the relation

$$\mathcal{D}_{\rm X} = 4\pi \int_0^{R_{\rm X}} n_{\rm H}(r) H_{\rm X}(r) r^2 dr \tag{3.30}$$

where

$$H_{\rm X}(r) = \frac{L_{\rm X}}{4\pi r^2} \int \sigma_{\rm T}(E)\varphi(E)e^{-\tau(E,r)}dE \tag{3.31}$$

is the local X-ray energy deposition rate per particle (Maloney et al. 1996). Considering a cumulative X-ray luminosity $L_{\rm X} = 3.9\times10^{34}$ erg s^{-1} for the Cyg OB2 association (Flaccomio et al., in preparation), and a gas number density $n_{\rm H} = 20$ cm^{-3}, we find $R_{\rm X} \sim 5$ pc, and finally $\mathcal{D}_{\rm X} \sim 2 \times 10^{34}$ erg s^{-1}.This values is approximatively five orders of magnitude lower than the wind mechanical luminosity (i.e. the energy input rate to the wind bubble) for the Cygnus OB2 association $L_{\rm w} = 1 - 2 \times 10^{39}$ erg s^{-1} (e.g., Anchordoqui et al. 2007). Interestingly, we have derived a similar value for the aggregate X-ray luminosity able to produce a Röntgen sphere with 100 pc radius.

3.6 Pre-main sequence stars

In the previous Section we show that in circumstellar environments of massive stars, the gas ionization is dominated by the extreme ultraviolet fields. X-rays controls the ionization only beyond the edge of the HII region, if their residual flux is intense enough to overcome the background fast particle ionization rate. Such situation radically changes in the regions embedding PMS stars. These objects are particularly interesting in the context of this investigation because they are very active stars, they possess high $L_{\rm X}/L_{\rm bol}$ ratios, with low emission in the ultraviolet band. Furthermore, such stars show strong and frequent flaring activities. PMS stars exhibit X-ray luminosities significantly greater than those of main sequence stars of the same spectral type. Moreover, being very young, they harbor disks and possibly young planets. Thus, their radiation environments may affect prebiotic evolution in the disk (e.g., Ciaravella et al. 2016; Jiménez-Escobar et al. 2016), and possibly impact on biological processes (e.g., Smith et al. 2004).

We initially consider an isolated star representing a reasonable analogue of the PMS Sun, a 1.8 My old K0 T-tauri star of 1.08 $M_\odot$, with both radius and bolometric luminosity approximately twice the solar ones (Preibisch & Zinnecker 1999). The star is located in Upper Scorpius. From the results of Figure 3.3 relevant for the case of modest ultraviolet irradiation, selecting the ratio $L_{\rm X}/\varsigma_{\rm cr} = 1 \times 10^{47}$ erg, and assuming a fractional ionization $n_e/n_{\rm H}$ smaller than 1%, we obtain $R_{\rm X} = 0.19$, 0.041, and 0.006 pc for $n_{\rm H} = 1 \times 10^2$, 1×10^4, and 1×10^6 cm^{-3}, respectively. Such values correspond to volume averaged ionization rates $\langle\varsigma_{\rm X}\rangle/\varsigma_{\rm cr} = 7.7$, 15.3, and 50.5. Exploiting the harder P10 spectral shape, we now get

Table 3.3: Röntgen radii for solar proxies

star†	age (Gyr)	$R_{\rm X}^{\ddagger}$ (pc)		
$\log_{10}(n_{\rm H}/{\rm cm}^{-3})$		2	4	6
K0	0.002	1.9(-1)⋆	4.1(-2)	5.6(-3)
EK Dra	0.1	8.1(-2)	1.6(-2)	3.1(-3)
π^1 UMa + χ^1 Ori	0.3	3.7(-2)	8.3(-3)	1.8(-3)
κ^1 Cet	0.65	2.8(-2)	6.7(-3)	1.5(-3)
β Com	1.6	1.3(-2)	4.2(-3)	9.2(-4)
Sun	4.56	6.7(-3)	2.6(-3)	5.6(-4)
β Hyi	6.7	4.2(-3)	1.9(-3)	4.2(-4)

† K0: Preibisch & Zinnecker (1999), all other stars: Ribas et al. (2005);
‡ $L_{\rm X}/\varsigma_{\rm cr} = 1 \times 10^{47}$ erg;
⋆ $1.9(-1) = 1.9 \times 10^{-1}$

$R_{\rm X}$ = 0.19, 0.035, and 0.006 pc for the assumed gas densities. In this case the volume averaged ionization rates result 11.5, 29.8, and 28.5.

It is instructive to estimate how long a solar-like star maintains an appreciable Röntgen radius. Ribas et al. (2005) presented a selected sample of stellar proxies for the Sun with ages covering most of its main-sequence lifetime. Setting $n_{\rm H} = 100$ cm^{-3} and normalizing to the radius of a 1 $M_\odot$ star (see Ribas et al. 2005), $R_{\rm X} = 8 \times 10^{-2}$ pc at 0.1 Gyr, and remains within a factor of 3 for a ten times older star. The Sun (4.56 Gyr old) produces a Röntgen radius 30 time lower than during its PMS. $R_{\rm X}$ values for seven representative stars (and age stages) are given in Table 3.3.

We also compute the Röntgen radii for all the stars of COUP program of which the X-ray luminosities have been estimated, and show them as functions of the ratio $L_{\rm X}/L_{\rm bol}$ between the X-ray and bolometric luminosities (Figure 3.7). The values we derive, together with those for solar PMS proxies suggest that young stars formed in clusters may significantly contribute to the overall ionization level. Using the COUP correlation between X-ray luminosity $L_{\rm X}$ and the stellar mass (Preibisch et al. 2005), in combination with the model of star formation in ONC from Palla & Stahler (1999), Adams et al. (2012) derive the expectation value of the X-ray luminosity per star over the whole distribution of stellar masses $\langle L_{\rm X} \rangle = 2.6 \times 10^{30}$ erg s^{-1}. Such luminosity corresponding to a stellar mass of $\sim 1.2 M_\odot$, produces a Röntgen radius $R_{\rm X}^{\rm o} = 0.13$ pc in a gas with $n_{\rm H} = 1 \times 10^2$ cm^{-3}, the mean number density for the Orion molecular cloud, and a volume averaged X-ray ionization $\varsigma_{\rm X}^{\rm o} \sim 6 \times \varsigma_{\rm cr} = 6 \times 10^{-16}$ s^{-1}.

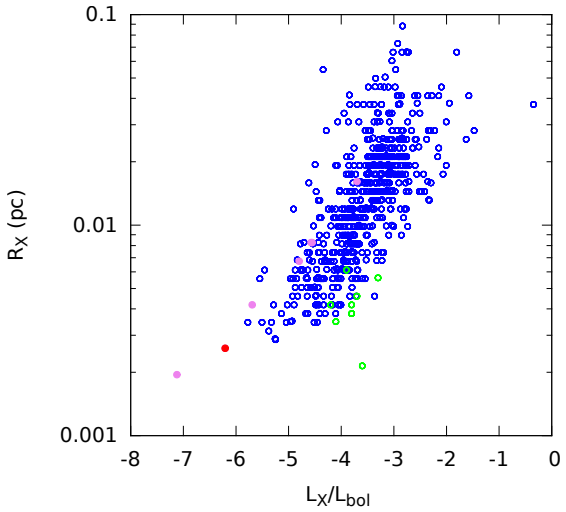

Figure 3.7: Röntgen radii as functions of the ratio $L_{\rm X}/L_{\rm bol}$ between the X-ray and bolometric luminosities in the case of $n_{\rm H} = 10^4$ cm^{-3}. Blue empty circles are COUP stars. Green empty circles label COUP brown dwarfs. Violet filled circles are the solar proxies of Table 3.3, the red filled circle labels the Sun.

Thus, the minimum number of PMS stars filling a cubic-parsec volume nedded to provide an average ionization $\varsigma_{\rm X}^{\rm o}$ is $\mathcal{N}_\star \sim (1 \text{ pc}/R_{\rm X}^{\rm o})^3 \sim 500$, a value consistent with e.g., Orion B, ρ Oph, and Chamaeleon I, and much lower than the stellar density inferred for Orion A. The numbers of stellar members in the ONC extrapolated from the number of COUP sources at distances of 0.1 and 0.25 parsec from the cluster centre result 22,600 and 4,700 (King et al. 2012), respectively. The mean distance among the stars is then ~ 0.035 and 0.06 pc. At such distances the average ionizations increase to $\varsigma_{\rm X}^{\rm o} \sim 5 \times 10^{-14}$ and 1.3×10^{-14} s^{-1}, respectively. Such widespread diffuse X-ray radiation must be taken into account in the ionization balance.

High X-ray ionization background levels are excluded from regions of much lower stellar density, such as L1495 in Taurus, in which (at most) 10 stars per cubic parsec, are inferred for a distance of approximately 1 pc from the cluster center.

3.7 Discussion

In this chapter we present a detailed model of the interaction of stellar X-rays with circumstellar matter. We test and validate this model studying the formation of regions in which

X-rays are the major ionization channel. Such regions, called Röntgen spheres (Lorenzani & Palla 2001) may have considerable importance in the chemical and physical evolution of the gas embedding the emitting star.

For PMS stars, generally characterized by modest ultraviolet irradiation and appreciable $L_{\rm X}/L_{\rm bol}$ ratios, we find that significant volumes of gas are affected by ionization levels exceeding largely the cosmic-ray background ionization. In clusters arising in regions of vigorous star formation X-rays create an ionization network pervading densely the interstellar medium. Such X-ray background radiation in young embedded clusters is potentially a key factor in star and planet formation (e.g., Feigelson 2010), providing a natural feedback mechanism that may act e.g., as a brake to accelerating star formation, through an increase of the coupling of the magnetic field to the cloud material via ambipolar diffusion (Lorenzani & Palla 2001). Whatever the case may be, doubtless X-rays are an important component of the energy balance and in the chemical evolution.

In regions of massive star formation the radiative transfer feedback appear to be of limited use. The formation of extended volumes with relevant levels of ionization is efficient just in a narrow range of gas volume densities, and only for very high X-ray luminosity and $L_{\rm X}/L_{\rm bol}$ ratios. In the case of Cygnus OB2 association the cumulative extent of the Röntgen spheres suggests that mechanical energy injection from fast stellar winds (and possibly supernovae, see Wright et al. 2015b) played a major role in dispersing dense dusty gas and possibly in driving outflows from the region. Preliminary studies of the the energetics of the Tarantula Nebula (30 Doradus) in the Large Magellanic Cloud give support to this interpretation, suggesting that the total kinetic energy of the nebula is dominated by the turbulent and bulk motions of HII gas (Wang & lim 2016). This is particularly interesting as the Large Magellanic Cloud is a metal-poor galaxy, in which X-rays should be more pervasive than in typical Galactic regions.

In conclusion, our study provides an accurate estimate of the degree of ionization in regions embedding X-ray emitting stars, and quantify the X-ray contribution to the total ionization of the gas. This work is not only a presentation of the basic processes to be considered, but it supports the idea that X-ray could be among the most relevant ingredients in the evolution of a variety of astronomical regions, including star forming regions, and protoplanetary systems. The effects computed in this chapter are likely too weak to be observed with present days x-ray telescopes. Observations with the next generation telescopes, such as Athena, with high troughput and high spatial resolution could allow us to test the real extent of these phenomena.

Chapter 4

Gaseous planet evolution around active stars

4.1 Introduction

X-rays impacting on a gas produce a variety of effects, that depending on the electron content, may provide a significant heating of the illuminated region. In a planetary atmosphere of solar composition X-rays penetrate much deeper than ultraviolet radiation, where they are mainly absorbed by heavy elements. (e.g. Cecchi-Pestellini et al. 2006). In some cases, the upper layers of the atmosphere can be lost (see §1.2). The transiting exoplanet HD 209458b has been the first planet with an observed on going atmospheric hydrodynamic escape (Vidal-Madjar et al. 2003). In this respect, evidences have been obtained by the absorption excess in the Lyman-α line. Such an excess suggests the presence of a extended upper atmosphere beyond the Roche lobe. The rate escape has been estimated to be about 10^{10} g s^{-1} (Vidal-Madjar et al. 2003).

In the last years various authors (e.g Lecavelier Des Etangs 2007; Erkaev et al. 2007) have developed simple models based on the energy-limited approximation first proposed by Watson et al. (1981), in order to estimate the mass loss through hydrodynamic escape. In this Section, using similar methods we shall investigate the effects in time of the atmospheric mass loss on giant exoplanets at several distances from a parent star. The simulation has the initial point located at 10 Myr, where it is supposed that planets have already reached their final orbit through migration. The so-called migration type-I is the main migration mechanism for low mass exoplanet, in which planets exchange angular momentum with the

disc. The planet is completely embedded into the disc and the interaction with the gas internal to the planet's orbit increases its angular momentum, while the interaction with the external disc removes angular momentum. The timescale of the type-I migration is very short, an Earth-like planet can migrate inward in about 10^5 yr, its migration become faster as the mass of the planet increases (Hasegawa & Ida 2013), and can fall into the star before to reach the critical mass core for gas accretion leading to the formation of giant planets (Tanaka et al. 2002). The exact time scale of migration depends on the mass of the planet and the density of the disc. Giant planets that are massive enough, are expected to undergo migration of type-II. In this case the planet is able to open a gap in the disc still through angular momentum exchange; once that a gap has opened, unless the planet is extremely massive, the disc has more angular momentum than the planet, so the planet simply migrate inwards with the disc's viscous accretion flow. The migration rate is typically slower than would be the migration of the planet in the type-I regime (D'Angelo et al. 2003); the timescale is however still smaller than the dispersal time of the disc (about 10 Myr), and it explains the existence of close-in hot-Jupiters that form typically at $5 - 10$ AU. In the present analysis type-III migration has been neglected, since it occurs later, being due to tidal interaction with the hot stars.

In order to estimate the effects on the shape of planetary mass function, we start the simulations assuming an uniform planetary mass distribution. For the planetary radius, numerical simulations by Burrows et al. (1993, 1997) have been exploited. The radius is allowed to change with the time in response to the mass loss induced by the XUV radiation, and the natural contraction of the planetary atmosphere due to the decrease of the stellar insolation (Burrows et al. 2000). Fressin et al. (2013) using the catalog of more than 2300 candidate transiting planets, released in 2013 February by the mission Kepler (Batalha et al. 2013), have inferred the today distribution of exoplanets around a given star. They take into account five classes of exoplanets and eleven period bins, as reported in Table 4.1. The distribution does not depend on the spectral type of the stars, and is valid for F-G-K-M stars. The current planetary distribution given in Fressin et al. (2013) constitutes the starting of the present simulation. Since recent advances in the techniques of detections exoplanets allow to detect exoplanets around active young T-Tauri stars (Donati et al. 2017), then it would be important to understand both the distribution of giant exoplanets, and the causes that produce it around young stars. Since young stars are know to be strong emitters of high energy photons we shall include in our simulation the effects of the XUV radiation.

In section 4.2 following Erkaev et al. (2007) we derive the formula for the computation of

the radiative mass loss rate, while in the subsequent Section the numerical code is described. In section 4.4 the code is applied to the planet population described above, deriving the mass an the radius evolution, and the effect on the shape of the planetary mass function.

Table 4.1: Average number of planets per star per period bin (in percent) nowadays (Table from Fressin et al. (2013))

Class	period range(days)										
	0.8-2.0	2.0-3.4	3.4-5.9	5.9-10	10-17	17-29	29-50	50-85	85-145	145-245	245-418
Giants	0.015	0.067	0.17	0.18	0.27	0.23	0.35	0.71	1.25	0.94	1.05
Large Neptunes	0.004	0.006	0.11	0.091	0.29	0.32	0.49	0.66	0.43	0.53	0.24
Small Neptunes	0.035	0.18	0.73	1.93	3.67	5.29	6.45	5.25	4.31	3.09	...
Super-Earhts	0.17	0.74	1.49	2.9	4.3	4.49	5.29	3.66	6.54	...	...
Earhts	0.18	0.61	1.72	2.7	2.7	2.93	4.08	3.46	...	...	...

4.2 Mass loss rate

Let's consider a system consisting of a planet with mass $M_{\rm pl}$ and a star with mass $M_{\rm st}$, separated by a distance d, rotating around the common center of mass (CM). The system refers to a non-inertial co-rotating frame of reference. The energy per unit mass of a test particle in the ecliptic plane results

$$\Phi = -\frac{GM_{\rm pl}}{r_a} - \frac{GM_{\rm st}}{r_b} - \frac{G(M_{\rm pl}+M_{\rm st})s^2}{2d^3} + \mathcal{C} \tag{4.1}$$

where s is the distance of the test particle from the CM, r_a and r_b the distances from the planet and the star respectively, G the gravitational constant, and $\mathcal{C}$ an integration constant. The first term accounts for the potential energy of the planet, the second and the third ones for those of the star and the motion of the whole system, respectively. Defining the dimensionless quantities $\lambda = d/r_{\rm pl}$, $\eta = r_a/r_{\rm pl}$, $\delta = M_{\rm pl}/M_{\rm st}$, and $\Phi_0 = GM_{\rm pl}/r_{\rm pl}$, $r_{\rm pl}$ being the radius of the planet, the variation of the potential along the line connecting the planet to its parent star is

$$\Phi(\eta) = \Phi_0\left[-\frac{1}{\eta} - \frac{1}{\delta(\lambda-\eta)} - \frac{1+\delta}{\delta}\left(\lambda\frac{1}{(\lambda+\delta)} - \eta\right)^2\frac{1}{2\lambda^3}\right] \tag{4.2}$$

There are some points in which the sum of all forces is equal to zero and therefore these points (called *Lagrangian points*) are saddle points for the potential (see Figure 4.1 for a stellar binary system). The equipotential surface that contains the point L_1 defines the Roche lobes: the matter that crosses this surface loses its gravitational bound with the planet. The location of the Lagrangian point L_1 is given by

$$r_{Rl} = \left(\frac{\delta}{3}\right)^{\frac{1}{3}} \left[1 - \frac{1}{3}\left(\frac{\delta}{3}\right)^{\frac{1}{3}}\right] d \tag{4.3}$$

Since $\delta \ll 1$, defining the quantity $\xi = r_{Rl}/r_{pl}$ we obtain

$$\xi \approx \left(\frac{\delta}{3}\right)^{\frac{1}{3}} d. \tag{4.4}$$

The difference between the potential at the Roche boundary $\Phi(\eta = \xi)$, and the potential at the planetary surface $\Phi(\eta = 1)$ is given by

$$\Delta\Phi = \Phi_0 \frac{(\xi - 1)}{\xi} \left\{1 - \frac{1}{\delta}\frac{\xi}{\lambda^2}\frac{\left[\lambda(1+\xi) - \xi\right]}{(\lambda - 1)(\lambda - \xi)} - \frac{(1+\delta)\xi(1+\xi)}{2\delta\lambda^3}\right\} \tag{4.5}$$

Supposing $d \gg r_{Rl} > r_{pl}$, $\lambda \gg \xi > 1$ and $\delta \ll 1$, after some algebraic manipulation equation (4.5) becomes

$$\Delta\Phi = \Phi_0 \frac{(\xi - 1)}{\xi} \left[1 - \frac{1}{2}\frac{(1+\xi)}{2\xi^2} + O\left(\frac{1}{\lambda}\right)\right] \tag{4.6}$$

Expanding equation (4.6) with respect to $1/\xi$, we finally obtain

$$\Delta\Phi = \Phi_0 \left(1 - \frac{3}{2\xi} + \frac{1}{2\xi^2}\right) = \Phi_0 K \tag{4.7}$$

where $K = 1 - 3/2\xi + 1/2\xi^2 < 1$.

Considering a steady-state hydrodynamic escape from a spherical atmosphere, and integrating the 1D equation of the energy conservation from the base of the thermosphere $r_0 \simeq r_{pl}$ up to the Roche lobe boundary r_{Rl}, we obtain an equation for the mass loss rate:

$$\frac{dM}{dt} = \frac{4\pi Q}{\Delta\Phi + \frac{v_{Rl}^2}{2} + c_p(T_{Rl} - T_0)} \tag{4.8}$$

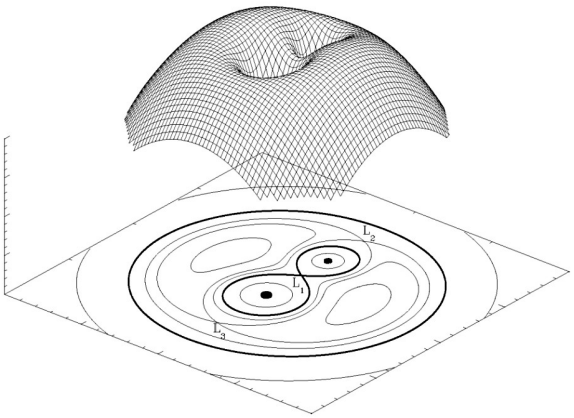

Figure 4.1: 3D representation of the potential energy of a binary system (two stars with mass ratio 2:1) as a function of the position in the orbital plane. In the picture is also showed the section of the equipotential surface on the orbital plane. L_1, L_2 and L_3 are Lagrangian points.

where $4\pi Q$ is the net radiative power due to balance between the high energy incoming radiation due to the parent star and the radiative low frequency loss due to the atmospheric cooling, v_{Rl} the gas flow velocity at the Roche lobe boundary, c_p the specific heat at constant pressure per unit mass of gas, T_{Rl} and T_0 the temperature of the gas at the Roche lobe boundary and the planetary radius, respectively. In the energy-limited loss approximation the kinetic and thermal energy terms are assumed to be negligible. The net radiative power per unit of angle solid is given by

$$Q = \int_{r_{pl}}^{r_{Rl}} q r^2 dr \tag{4.9}$$

where $q = q_{\rm XUV} - q_{\rm IR}$ is the net volume heating rate of the atmosphere, with $q_{\rm XUV}$ the heating rate due to absorption of the stellar high energy XUV radiation, and q_{IR} the cooling rate due to emission of infrared radiation by the molecules of the planetary atmosphere. Introducing the planetocentric distance $r_{\rm XUV}$, i.e. the distance at which the bulk of the incoming stellar flux $F_{\rm XUV}$ is absorbed by the atmosphere, and ignoring the radiative cooling infrared flux, we obtain

$$4\pi Q = 4\pi r_{\rm XUV}^2 F_{\rm XUV} \tag{4.10}$$

where

$$r_{\rm XUV} = \frac{\int_{\rm r_{pl}}^{\rm r_{Rl}} {\rm q r^2} dr}{\rm F_{XUV}}. \tag{4.11}$$

Inserting equations (4.7) and (4.10) into equation (4.8) we find the energy-limited equation for the mass loss rate

$$\frac{dM}{dt} = \frac{\pi r_{\rm XUV}^2 F_{\rm XUV}}{\Phi_0 K}. \tag{4.12}$$

In the last equation we have divided for an averaging factor equal to 4, in order to take into account the effective planetary cross-section $\pi r_{\rm pl}^2$.

4.3 Planets atmosphere evolution

We start with a population of giant planets possessing an uniform mass distribution in the $0.2 - 16 M_J$ range. At $t_{\rm in} = 10$ Myr we assign to each planet an initial radius taken from Burrows et al. (1993, 1997), that compute the radius as a function of time for several planetary masses. The exploited Burrows' models of planets are in the $0.5 - 12 M_J$ mass range. For planetary masses outside the available mass range, in the assignment of the radii we increase or reduced the mass to the terminal points of the interval. This is a conservative choice because at both the extremes of the mass intervals the radius computed by Burrows' models tends to increase. Because the mass loss rate increase with the radius – see equation (4.12) – our assumption likely underestimates the mass loss rate. In all other cases when necessary we interpolate linearly. In Figure 4.2 it is shown the adopted initial mass-radius relation. Following Sanz-Forcada et al. (2011) we use the following relation for the calculation of the mass loss

$$\frac{d\rm M}{d\rm t} = \frac{\pi \rm r_{pl}^3 F_{XUV}}{\rm G M_{pl} K}. \tag{4.13}$$

that differs from equation (4.12), because we now assume that the bulk of the XUV radiation is absorbed by materials close to the planet radius. As a consequence $r_{\rm XUV} \backsimeq r_{pl}$. In contrast to Sanz-Forcada et al. (2011) we calculate the factor K that accounts for the Roche lobe losses.

Several works have studied the evolution of the high energy luminosity of solar type stars, showing that the intensity of the XUV radiation drops with the time (e.g. Micela 2001; Ribas et al. 2005). In order to account for this effect in the X-ray band, we use the prescription given in Penz et al. (2008) in case of dG stars, and Penz & Micela (2008) for dM stars

$$L_{\rm X} = \begin{cases} a_1 L_0 \tau^{b_1} & \tau \leq 0.6 \quad \text{Gyr} \\ a_2 L_0 \tau^{b_2} & \tau > 0.6 \quad \text{Gyr} \end{cases} \tag{4.14}$$

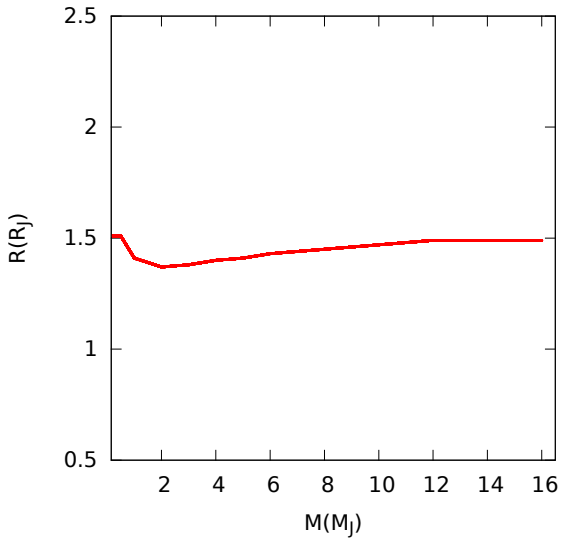

Figure 4.2: Assumed mass-radius distribution at 10 Myr. Data from Burrows et al. (1993, 1997)

where L_0 is the mean luminosity of the star. As reference stars dG and dM stars in the Pleiades have been chosen, because the Pleiades are a young stellar cluster, with an estimate age of 80 Myr. The luminosities result $L_0 = 10^{29.35}$, and $L_0 = 10^{28.75}$ erg s^{-1} (Preibisch & Feigelson 2005), for dG and dM stars, respectively. The coefficients in equation (4.14) are: $a_1 = 0.379$, $a_2 = 0.19$, $b_1 = -0.425$ and $b_2 = -1.69$ for dG stars, and $a_1 = 0.17$, $a_2 = 0.13$, $b_1 = -0.77$ and $b_2 = -1.34$ for dM stars. The luminosities are expressed in erg s^{-1}, and τ is the age in Gyr. The equation (4.14) describes the evolution of the mean value of the X-ray luminosity distribution. We note, however, that the X-ray luminosity of a star is not determined only from the age, but at a given age it follows a distribution, whose mean value is determined by the relation (4.14), with a spread of about one order of magnitude. This distribution function may be represented by a log-normal distribution function, whose cumulative distribution function reads as

$$\mathrm{CDF}[\ln(L_\mathrm{X})] = \frac{1}{2} + \frac{1}{2}\mathrm{erf}\left[\frac{\ln(L_\mathrm{X}) - \mu}{\sigma\sqrt{2}}\right], \tag{4.15}$$

where erf is the error function, μ and σ the mean and the standard deviation of the logarithm variable, respectively. For instance, for the case of G stars $\sigma = 1.1$ and $\mu = 67.58$ (Penz et al. 2008), corresponding to $L_\mathrm{X} = 10^{29.35}$ erg s^{-1}, the mean luminosity of G stars in the Pleiades.

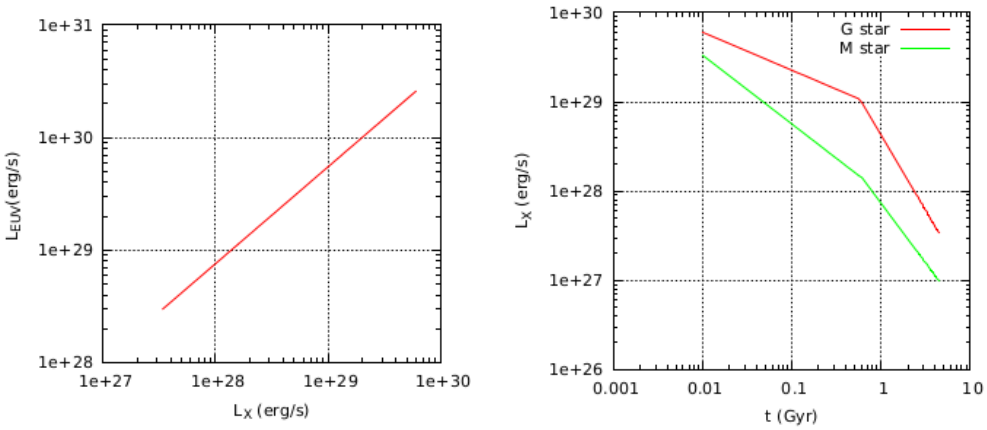

Figure 4.3: Left panel: Relation between X-ray and EUV luminosities for a G star. Right panel: X-ray luminosity as a function of the time for a dG and a dM star, extracted by the log-normal distribution as explained in the text.

Thus, starting from equation (4.15), it is possible to calculate the number of stars with X-ray luminosity inside a given bin. We assign randomly to each star an initial X-ray luminosity $L_{i,0}$ from equation (4.15), that then evolves following equation (4.14) with $L_0 = L_{i,0}$.

In order to estimate the EUV luminosity we use the relation given in Sanz-Forcada et al. (2011)

$$\log(L_{\rm EUV}) = 4.8 + 0.86 \times \log(L_{\rm X}), \tag{4.16}$$

in which the evolution of the EUV radiation follows that of the X-ray band. The flux $F_{\rm XUV}$ is gven by the superposition of the luminosities in the X and EUV bands. In Figure 4.3 we can see the $L_{\rm X}$-$L_{\rm EUV}$ relation for the case of a G star (left panel), and the X-ray luminosity as function of the time for a G and a M star (right panel). The stellar 11/5000 insolation opposes to the natural contraction of the radius of a giant planet under his own weight. The rate at which the radius decreases is determined by the bond albedo, the presence of clouds and their optical depth, the gas-phase abundances and their opacities, and by the intensity of the stellar radiation (Burrows et al. 2000). In our model the mass of the planet changes with the age due to mass loss induced by high energy radiation. As a consequence the planetary radius varies also for this contribution. In order to account for this additional effect we use the model put forward by Burrows and coworkers (Burrows et al. 1993, 1997) as described above, adopting the radius corresponding to the age and the new mass of the planet. In Figure 4.4 we show the planetary radius as a function of the time for 13 exoplanetary masses

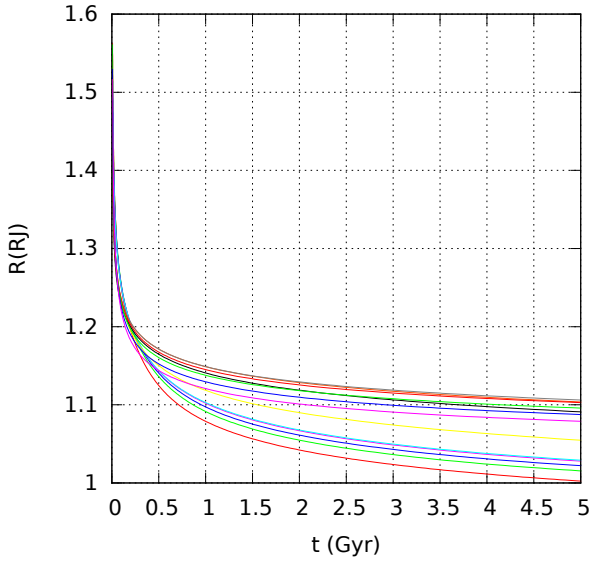

Figure 4.4: Variation of the planetary radius as a function of time for 13 exoplanets. Masses are in the range $0.5 - 12 M_J$.

in the range $0.5 - 12 M_J$ without mass loss. In our simulation we start at $t = 10$ Myr assuming the mass-radius relation shown in Figure 4.2. We then calculate the mass loss of the planet, and derive the new radius (and therefore the density), using the Burrows's tracks, corresponding to the new mass at the time $t + dt$. We iterate until the age reaches $t = 4.5$ Gyr.

4.4 Results

We consider the case of a dG star of 1 $M_\odot$, and a dM star with mass $M = 0.3 M_\odot$. In Figure 4.5, we show the mass-radius relation after 4.5 Gyr for our planet population. We studied the evolution of planets subdividing them into several bins with different distances from the central star corresponding to the Fressin's period bins. Inside each period bin we randomly assign a period at each planet. We find that, as expected, distant planets are less affected by mass loss, with their radius mainly constrained by natural contraction. On the contrary the physical properties of closer, and low mass planets are significantly losing mass.

In Figure 4.6 we show the mass distribution of planets as a function of period bins for

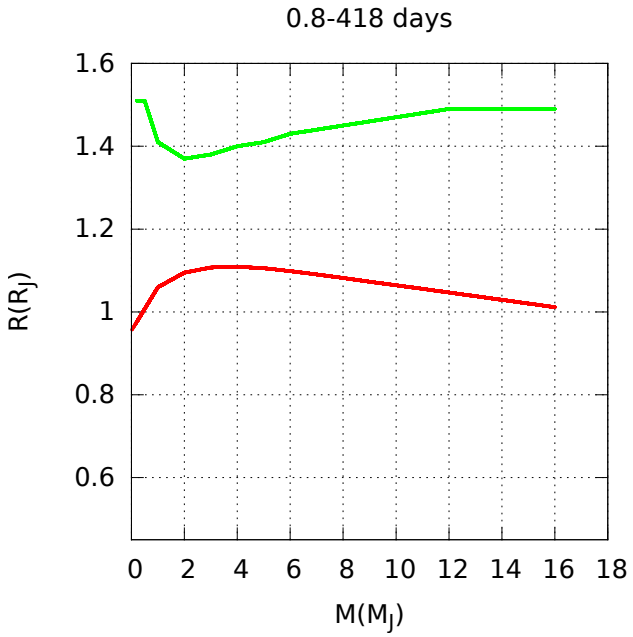

Figure 4.5: Cumulative final mass relation after 4.5 Gyr in the range $0.02 - 1.1$ AU (period $0.8 - 418$ days).

either dG and dM stars. The blue line is the initial planetary mass distribution (flat for both dG and dM stars), while red and green lines represent their final distributions at 4.5 Gyr. Planets subject to mass loss move towards left (low mass) during their evolution. Figures show that low mass Jupiter-like planets, close to the star are strongly affected, with a large fraction of those with $M < 0.7 M_J$ that vaporize. The most affected planets are those with a large radius (low density) and with the host star belonging to the high luminosity tail of the X-ray luminosity distribution. Planets with orbital period greater 17 days survive.

In detail, in the first bin ($P = 0.8 - 2$ days) the percentage of lost planets is 4%, and decreases to 2% in the second bin ($P = 2 - 3.4$ days) to drops to a negligible value at larger periods. However, the number of lost planets is not evenly distributed over the entire range of masses, but is concentrated at low mass. At the shortest orbital period (top left panel), 40% of planets in the $0.2 - 1 M_J$ bin and the 16% in the $0.2 - 1 M_J$ bin are lost. In Figure 4.6 we show how XUV radiation affects the planetary population around dG and dM stars, the effects are comparable, albeit X-ray luminosity of dM stars is less than that of dG star (see Figure 4.3). This is due to the fact that, for a given period, orbital distances from dM stars

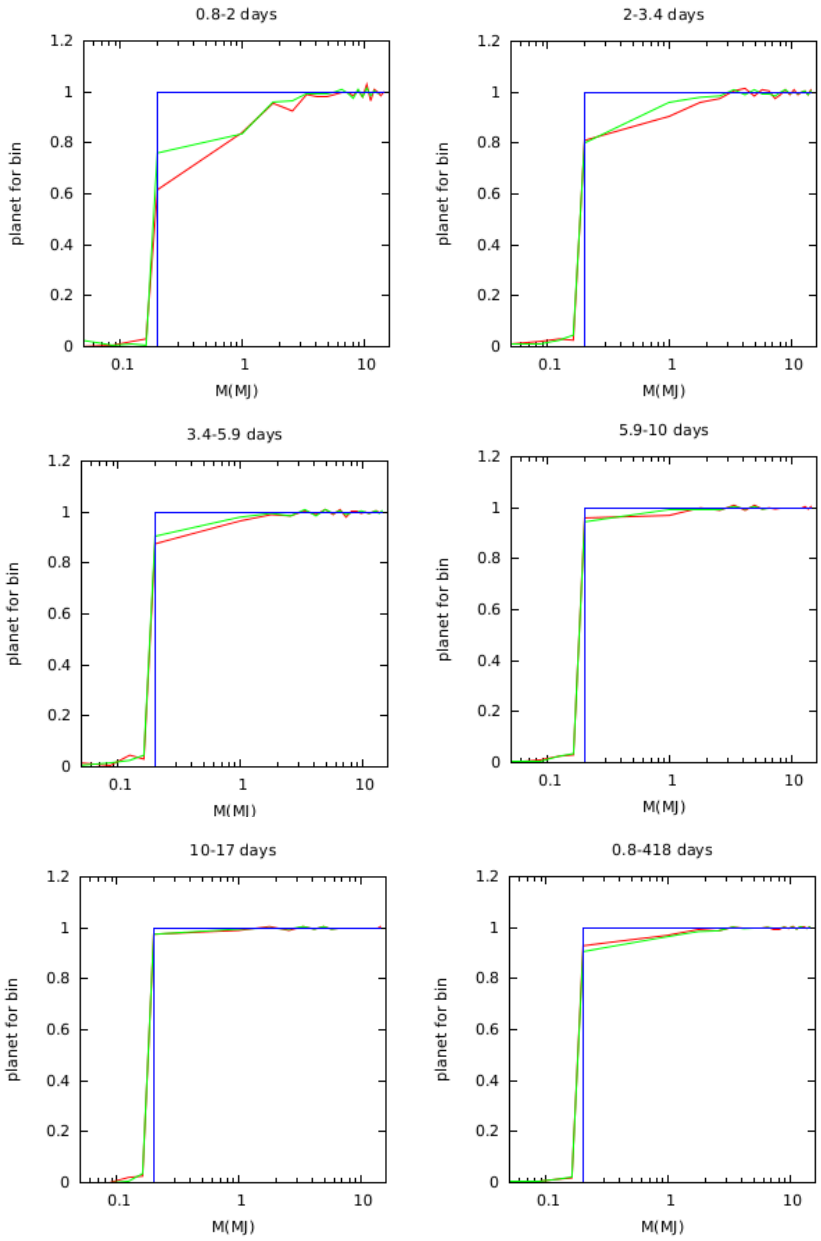

Figure 4.6: Number of planet per mass bin. Each panel corresponds to an orbital period interval. The last panel (right bottom) shows the mass distribution for planets in the period range $0.02 - 1.1$ AU. The blue line is the initial (flat) mass distribution, the red line is final mass distribution for planet around G a star, while the green line is the final mass distribution for planet around a dM star.

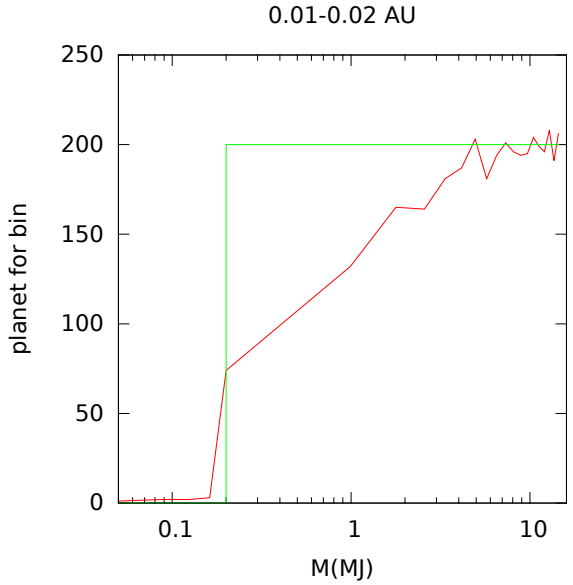

Figure 4.7: Mass distribution in the distance range $0.01 - 0.02$ AU for exoplanet around dG stars. Green line is the initial (flat) mass distribution, while the red line is the final distribution at 4.5 Gyr.

are smaller than for dG stars, while planets orbiting the two class of stars similar levels of high energy irradiation.

In order to investigate the effects of the ionizing flux of much more intensity than those considered up to now around G stars, we apply the present model to the extreme case of planets orbiting in the distance range $0.01 - 0.02$ AU ($0.4 - 0.8$ days). In Figure 4.7 it is shown the final mass distribution at such distances. In this case, 10% of planets are lost in the entire mass range $0.2 - 13 M_J$, 91% of whom are vaporized. We also find that 0.65 and 0.35 are the fraction of lost planets in the $0.2 - 1 M_J$ and $1 - 2 M_J$ mass bins, respectively. In Figure 4.8 it is shown the temporal evolution of radius and mass loss rate for four planets orbiting dG stars with initial mass 0.54, 1.2, 4.8, $12.8 M_J$, semiaxies in the range $0.02 - 0.03$ AU , initial X-rays stellar luminosities $L_{\rm X} = 3.0 \times 10^{28}$, 1.7×10^{29}, 3.5×10^{29}, and 1.9×10^{29} erg s^{-1}. We can see that the two most massive planets experience low levels of mass loss. The planet with initial mass $1.2 M_J$ suffers of an higher level of loss than the planet with smaller initial mass, basically because the radius of the first planet during part of its evolution is larger than that of second one (see Figure 4.8, left panel), while its X-rays luminosity is higher.

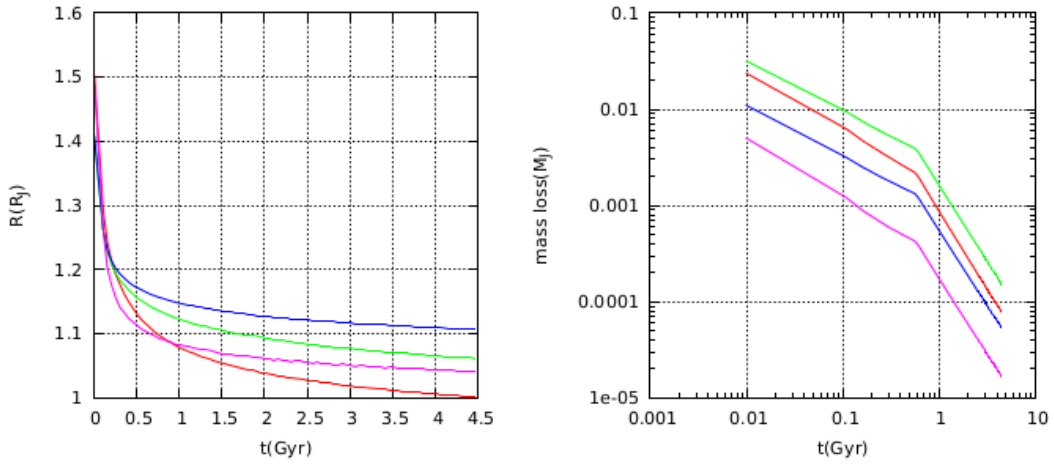

Figure 4.8: Left panel: evolution of the planet radius as a function of time for four selected planets. Right panel: mass loss as a function of time for four selected planets. In both panels, red lines refer to planets with initial mass of $0.54M_J$ ($L_{i,0} = 3 \times 10^{28}$ erg s^{-1}), green lines show the evolutionary histories of planets with initial mass of $1.2M_J$ ($L_{i,0} = 1.7 \times 10^{29}$ erg s^{-1}), the blue line of a planet with initial mass of $4.8M_J$ ($L_{i,0} = 3.5 \times 10^{29}$ erg s^{-1}) and the violet line planet with initial mass of $12.8M_J$ ($L_{i,0} = 1.9 \times 10^{29}$ erg s^{-1}). All planets are in the period range $0.02 - 0.03$ AU.

In Figure 4.9, we report the mass-radius relation for two different orbital distances around a dG star for planets of various ages. In the figure the black lines are the evolutionary paths followed by three planets with initial masses of 0.43, 1.2 and $1.36M_J$, orbiting a star with initial X-ray luminosity $L_X = 8.2 \times 10^{28}$, $1. \times 10^{30}$ and 1.36×10^{30} erg s^{-1} respectively. The two less massive planets vaporize before 0.5 Gyr, the smaller one because of its low density (although it orbits around a star with a low level of high energy radiation), while the other whose mass is $1.2M_J$ because its parent star has a very high value of $L_{i,0}$. The two more massive planets survive, despite their host stars have high values of $L_{i,0}$, ending up with a final mass much smaller than the initial one. The mass-radius relation is independent on high energy radiation, and follows Burrows' models, but the path followed by a planet in this diagram during its evolution do depend on the received X-ray flux. Figure 4.9 suggests that the position in the mass-radius relation for real exoplanets is the final result of different effects acting on exoplanets of different ages. Figure 4.9 also implies that the first 1.5 Gyr represent the period in which the radius and the mass suffer most of the variations. In presence of a population of planets with an age spread, we expect a spread in the mass-radius relation, with younger planets laying in the higher radius part of the diagram.

The final goal of our study is to estimate the percentage of giant planets per star for each

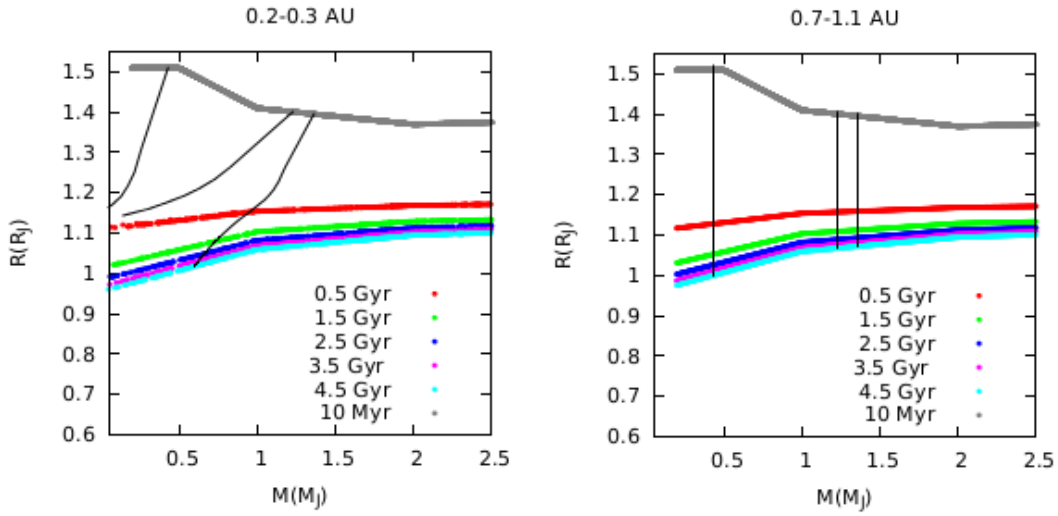

Figure 4.9: Mass-radius relation at different ages, for near (left panel) and far (right panel) exoplanets. In both panels, black lines refer to the evolutionary paths followed by three planets with initial masses $0.43 M_J$ ($L_{i,0} = 8.2 \times 10^{28}$ erg s^{-1}), 1.2 M$_J$ ($L_{i,0} = 1 \times 10^{30}$ erg s^{-1}), and 1.36 M$_J$ ($L_{i,0} = 1.36 \times 10^{30}$ erg s^{-1}).

period bin given in Table 4.1 at the age of 10 Myr. To this aim we use the distributions of Figure 4.6 as a correction function to be applied to the current planetary mass distribution (assumed being dominated by 4.5 Gyr old planets). In this way we derive the frequency of giant planets at 10 Myr. The results are reported in Table 4.2. We expect that at 10 Myr there are 4.5% more giant planets than at 4.5 Gyr in the period bin $0.8 - 2$ days ($0.02 - 0.03$ AU), 2% in the period bin $2 - 3.4$ days ($0.03 - 0.04$ AU), while at larger periods basically we do not expect any differences. In the overall range $0.8 - 85$ days ($0.02 - 0.4$ AU) at early stages of the star in main sequences, we derive 1.2% more planet than at the final stages. For the case of dM stars we obtain only a slightly lower values, because as already said the exoplanets in this case orbits closer to the central star. The derived differences are small and likely unobservable, even with the next future larger samples, however the differences are specifically concentrated in the $0.2 - 2 M_J$ range where the frequency of hot planets around young stars can be of the order of twice the frequency around their old counterparts.

Because the results of Table 4.2 may be sensitive to the precise mass of the stars, we studied also the case in which at each planet we randomly assigned a star with a specific mass. For the case of dG stars the masses are uniformly distributed in the $0.8 - 1.04 M_\odot$

Table 4.2: Derived frequency of planets per star per period bin (in percent) around young dG and dM stars, compared with the nowadays frequency (Fressin et al. 2013).

Star type	period range(days)										
	0.8-2.0	2.0-3.4	3.4-5.9	5.9-10	10-17	17-29	29-50	50-85	85-145	145-245	245-418
G	0.016	0.069	0.172	0.181	0.271	0.23	0.35	0.71	1.25	0.94	1.05
M	0.016	0.068	0.172	0.181	0.271	0.23	0.35	0.71	1.25	0.94	1.05
Fressin et al.,2013	0.015	0.067	0.17	0.18	0.27	0.23	0.35	0.71	1.25	0.94	1.05

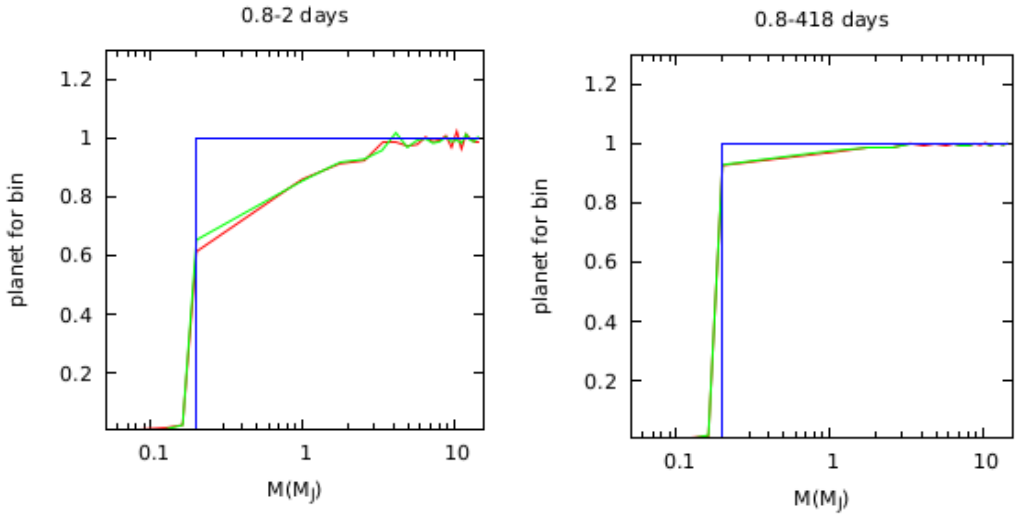

Figure 4.10: Initial and final mass distribution. Left panel: planets around dG and dM stars with short orbital periods. Right panel: cumulative mass distribution for planets around dG and dM stars. The colors of the lines are the same of 4.6.

range, in the case of dM stars the masses run in the $0.1 - 0.45 M_{\odot}$ range. In Figure 4.10 we show the resulting mass distribution in the case of closer planets and the total mass distribution for the case of dG and dM stars. It is clear that the mass distributions of planets around dG and dM stars are very similar, this results is coherent we the fact the distribution of planet around the stars find by Fressin et al. (2013) is independent from the star type.

4.5 Discussion

In this chapter we presented a model to simulate the hydrodynamic escape of a planetary atmosphere in presence of intense high energy flux. The model is based on the energy-

limited approximation. During the simulations the planetary radius changes in response to the mass loss, due to the combined effect of XUV radiation, and gravitational contraction. Two important factors (for evident reasons) are the planetary orbital distance and the time. This latter, other than sampling the evolutionary path, determines the intensity of the stellar flux. A third parameter is the spectral type of the central star, in particular at early evolutionary stage. Stellar radiation affects mostly the evolution of close-in, low mass planets.

The main results of the modeling procedure are as follows

- the history of the mass-radius relation is affected by the illuminating XUV radiation; this is derived from the evolution of X-ray and EUV luminosity functions that account both for the quiescent and flaring components. The initial mass radius relation is based on Burrows et al. (1993, 1997)

- a fraction of low mass Jupiter-like planets orbiting with periods lower than 17 days vaporize during the first billion years;

- the planetary mass function is significantly distorted by the high energy radiation. In particular, the frequency of occurrence of planets in the $0.2 - 2M_J$ mass range around young star can be twice than the planetary occurring frequency around older counterparts;

- the results are weakly dependent on stellar spectral types.

Chapter 5

Stellar XUV excitation of planetary H_2

5.1 Introduction

The atmospheric composition of the giant planets in the Solar System is dominated by hydrogen species. Molecular hydrogen is the most abundant gas in the upper atmosphere of these planets. Thus, almost all auroral emissions observed on the giant or outer planets (Jupiter, Saturn, Uranus, and Neptune) result from particle impact excitation of H_2. Some of the processes occurring during electron impacts are (*i*) vibrational excitations, cascading down to the ground state through infrared emission, (*ii*) Lyman ($B^1\Sigma_u^+ \rightarrow X^1\Sigma_g$) and Wener ($C^1\Pi_u^+ \rightarrow X^1\Sigma_g$) band emissions in the ultraviolet; (*iii*) dissociative excitation producing H-Lyman α ($n = 2 \rightarrow 1$) at 1216 Å, H_α ($n = 3 \rightarrow 2$) and H_β ($n = 4 \rightarrow 2$) in the visible; (*iv*) ionization of H_2 followed by the reaction $H_2^+ + H_2 \rightarrow H_3^+ + H$ with the resulting emission of H_3^+ in the infrared. Other precipitating particles (e.g. protons and/or heavy ions) would excite somewhat similar emissions, both directly or through secondary electron cascades that they produce.

In the case of hot Jupiters the above scenario must be tuned to the different driver of gas excitation, namely the XUV radiation. Moreover, since such planets are close enough to their host stars, the atmosphere may then go through a long phase of efficient hydrodynamic escape, or even blow-off, which depending on the the planet's atmosphere mass, may or may not significantly affect the planet. In this chapter, we put forward a model of XUV excitation of molecular hydrogen, and we identify, through a parametric analysis the regions of the parameter space able to provide non thermal H_2 emissions. We then provide estimate of the infrared brightness.

The problem we are addressing here is a typical example of non Local Thermodynamic Equilibrium (LTE) process. It arises when the internal temperature (internal energy) of a representative molecule, as determined by the statistics of the relative populations of the vibrational and rotational energy levels, becomes different from the external temperature, as determined by the statistics of the velocity distribution of the many molecules making up a parcel of gas. The existence of such difference depends primarily on the mean rate at which collisions take place between the individual molecules, and thus ultimately on the number density. In other words non LTE effects in a gas rely upon pressure and temperature. Since the pressure dependence usually dominates, non-LTE effects in a static atmosphere are mainly of importance only at the higher altitudes, e.g. in the stratosphere and above on Earth. In the present case, since the atmospheres of close-in planets are vented outwards, they may be very extended, and, therefore of lower densities than in more quiescent situations.

5.2 The H_2 level system

In statistical equilibrium the $\mathcal{N}$ populations n_i, $i = (v, J)$, of vibro-rotational levels of the H_2 electronic ground state are solutions to the set of algebraic equations (Cecchi-Pestellini et al. 2005)

$$n_i \left[\sum_{j<i} (A_{ij} + C_{ij} + W_{ij}) + \sum_{j>i} (C_{ij} + W_{ij}) + \beta_i + \varsigma + \mathcal{D}_i + \right.$$
$$\left. + \mathcal{K}_i^- \right] = \sum_{j>i} n_j A_{ji} + \sum_{j\neq i} n_j (C_{ji} + W_{ji}) + \mathcal{K}_i^+ + \mathcal{R}_\mathrm{F} \delta_i \qquad (5.1)$$

In equation (5.1), W_{ij} are the excitation rates from the level i to level j via ultraviolet pumping to electronically excited states, A_{ij} are the Einstein coefficients for spontaneous radiative decay, C_{ij} are the temperature–dependent collisional rates, β_i is the rate of photodissociation out of the level i, $\mathcal{D}_i$ is the rate of additional destruction processes, such as collisional dissociation and ionization, and $\mathcal{K}_i^\pm$ are entry (+) and exit (-) chemical rates. The destruction rate via ionization (to give either H_2^+ or $H + H^+$) is denoted by ς. The last term in the r.h.s. of equation (5.1) describes the formation of H_2: $\mathcal{R}_\mathrm{F}$ indicates the total volume formation rate, and δ_i is the fraction of H_2 formed in level i. This latter quantity is such that $\sum_{vJ} \delta_{vJ} = 1$. The level populations are subjected to the normalization conditions $\sum_{vJ} n_{vJ} = n_{H_2}$, where n_{H_2} is the number density of hydrogen molecules.

In the presence of a source of high energy photons (extreme ultraviolet radiation and X-rays) additional exit channels are provided by secondary electron non-thermal collisions resulting in excitations to the rotational states $J = 2$ and 3, and the vibrational manifolds $v = 1$ and 2. We indicate such excitation rates as $C_{ij}^{(e)}$. While C_{ij} are functions of the gas kinetic temperature, $C_{ij}^{(e)}$ depend essentially on the residual stellar XUV luminosity $L_{\rm H}$, and the electron fraction in the gas n_e (e.g. Locci et al. 2018).

In the case of modest continuous vacuum ultraviolet illumination both W_{ij} and β_i decline sharply, and the problem may be significantly simplified. Summing up both members of equation (5.1) over i, at the chemical equilibrium we obtain $n_{\rm H_2}(\varsigma + \sum_i \mathcal{D}_i) \approx \mathcal{R}_{\rm F}$; equation (5.1) now reads as

$$n_i \left[\sum_{j<i} (A_{ij} + C_{ij}) + \sum_{j>i} \left(C_{ij} + C_{ij}^{(e)} \right) \right] = \sum_{j>i} n_j A_{ji} + \sum_{j \neq i} n_j \left(C_{ji} + C_{ji}^{(e)} \right) \tag{5.2}$$

The radiative transfer code includes inelastic collisions with H, He and ortho– and para–H_2, with fully quantum mechanical calculations of collisional rates; for levels where quantum calculations are not available, some existing extrapolation schemes have been exploited (for details see Islam et al. 2010 and references therein). Quadrupole radiative decays and energies of vibro-rotational levels of the ground electronic state were taken from Wolniewicz et al. (1998). Electron impacts rates are computed following the prescriptions of Dalgarno et al. (1999), $C_{ij}^{(e)} = \eta_{ij} \times \varsigma_{\rm H}$ where η_{ij} are the entry efficiencies from the state i into the state j, and $\varsigma_{\rm H}$ the total ionization rate (Locci et al. 2018). The entry efficiencies may be computed as functions of the energy of the primary photoelectron for a mixture of H, He and H_2 exploiting the numerical code described in Cecchi-Pestellini et al. (2006). The chain of discrete energy deposition events is followed using the method put forward by (Cravens et al. 1975). We use the electron impact cross-sections for excitation, ionization, dissociation and elastic collisions listed in Dalgarno et al. (1999).

The branching ratios for vibro-rotational excitations by electronic impacts are estimated

from the Hönl-London factors for $\Sigma \rightarrow \Sigma$ electric quadrupole transitions

$$\mathcal{S}_{J'J"} = \begin{cases} \dfrac{J"(J"-1)}{2J"-1}, & O(J") \\ \dfrac{2J"(J"+1)(2J"+1)}{3(2J"-1)(2J"+3)}, & Q(J") \\ \dfrac{(J"+1)(J"+2)}{(2J"+3)}, & S(J") \end{cases}$$

taken in the tabulation of Kovacs (1969). In the present case the Hönl-London factors are normalized according to the rule $\sum_{J'} \mathcal{S}_{J'J"} = 2J"+1$ (Thorne et al. 1999). Other choices for the three rotational branches ($\Delta J = J" - J' = 0, \pm 2$) have been adopted in the literature (see e.g. Gredel & Dalgarno 1995), but the differences are quite modest. Summing over the level distribution we obtain

$$\sum_{J"} \sum_{J'} n_{(0,J")} \eta_{(0,v')} \varsigma_{\rm H} \frac{\mathcal{S}_{J'J"}}{2J"+1} = n_0 \eta_{(0,v')} \varsigma_{\rm H} \tag{5.3}$$

with $n_0 = \sum_{J"} n_{(0,J")}$. The corresponding vibro-rotational non thermal collision rates then read as

$$C^{(e)}_{ij} = \varsigma_{\rm H} \eta_{(0,v')} \frac{\mathcal{S}_{J'J"}}{2J"+1} \tag{5.4}$$

where $i = (0, J")$ and $j = (v', J')$.

5.3 XUV induced excitation of H_2: a parametric study

We solve the statistical equilibrium equations (5.2), for the first $\mathcal{N} = 300$ levels of the ground electronic state ($X^1\Sigma^+_g$) assuming constant gas number density and kinetic temperature. We also assume that the electron fractional content $n_e/n_{\rm H_2}$ is small enough that Coulomb dissipation does not dominate the energy loss of the secondary electron cascade. Within such constraints, the H_2 excitation depends on 3 free parameters, the XUV ionization rate $\varsigma_{\rm H}$, the H_2 number density $n_{\rm H_2}$, and the gas kinetic temperature T_k. The entry efficiencies per ionizing event η do not vary much with the energy of the secondary electrons (e.g. Tiné et al. 1997), and thus we adopt electrons with energy of 100 eV. The resulting entry efficiencies are reported in Table 5.1. In the table we also show the entry efficiencies in the case of high

Table 5.1: Entry efficiencies for 100 eV electrons in a gas composed of molecular hydrogen and 10% of helium.

transition	entry efficiency	
electron fraction	low ($\lesssim 10^{-3}$)	high ($\gtrsim 10^{-2}$)
$(0,0) \rightarrow (0,2)$	10.4	0.24
$(0,1) \rightarrow (0,3)$	16.8	0.44
$v" = 0 \rightarrow v' = 1$	6.2	0.14
$v" = 0 \rightarrow v' = 2$	0.4	0.02

electron concentration. This latter case corresponds to a decrease in a factor of ~ 40 in the excitation rates.

Secondary electrons populate preferentially vibrational excited states, the first of which, $(v, J) = (1, 0)$ is located at about 6000 K over the ground state. For this reason XUV-induced excitations may compete with thermal collisions at the high temperatures attained in close-in exoplanets. To quantify the relevance of XUV pumping we define the thermalization parameter

$$Y_{\rm th} = \frac{n^{\rm th}_{(1,0)}}{n_{(1,0)}} \tag{5.5}$$

where $n^{\rm th}_{(1,0)}$ is the population of level $(v, J) = (1, 0)$ in the thermal regime (no radiative pumping). For a H_2 gas either close to LTE or scarcely illuminated $Y_{\rm th} \approx 1$. It is important to note that $Y_{\rm th}$ does not map the shape of the spectrum. To this aim we should rely on line ratios, in particular the one between the transitions $(1-0)\ S(3)$ and $(1-0)\ Q(1)$, and therefore the population ratio $n_{(1,5)}/n_{(1,1)}$. Unfortunately, such ratio reaches the thermal regime for densities much lower than those expected in the planetary case (see Section 5.4).

We explore the parameter space reported in Table 5.2 for a total of 120 models. In Figure 5.1 we show $Y_{\rm th}$ versus the competing factors thermal pressure $P_{\rm th} = (1+2Y) \times n_{\rm H_2} T_k$ for six values of the ionization rate, $\varsigma_{\rm H}$, Y being the helium fractional abundance. It is important to note that the ratio R of this two factors is not an effective control parameter because it does not determine the behaviour of evolutionary trends in the spectrum, as it is clear from the results shown in Figure 5.1.

Table 5.2: Model grid

parameter	range	step	models
n_{H_2} (cm^{-3})	$1 \times 10^8 - 1 \times 10^{12}$	$\times 10$	5
T_k (K)	$500 - 2000$	$+500$ K	4
ς_H (s^{-1})	$1 \times 10^{-3} - 1 \times 10^{-8}$	$\times 10$	6

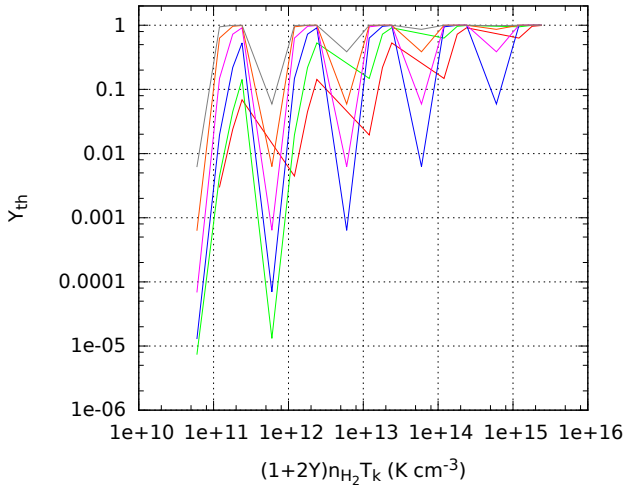

Figure 5.1: The thermalization parameter $Y_{\rm th} = n^{\rm th}_{(1,0)}/n_{(1,0)}$ versus the thermal pressure, $P_{\rm th}$. The various curve are parametrized with respect to the ionization rate, ς_H. Red line labels the spectrum computed with the XUV ionization rate $\varsigma = 10^{-3}$ s^{-1}, green line with $\varsigma = 10^{-4}$ s^{-1}, blue line with $\varsigma = 10^{-5}$ s^{-1}, the violet line with $\varsigma = 10^{-6}$ s^{-1}, the orange line with $\varsigma = 10^{-7}$ s^{-1} and the gray line with $\varsigma = 10^{-8}$ s^{-1}.

5.4 Emission spectra

The infrared emission spectra are computed as follows

$$\varepsilon_{\rm iR}(\nu) = \frac{h}{4\pi} \sum_i n_i \sum_{j<i} \nu_{ij} A_{ij} \varphi_{ij}(\nu - \nu_{ij}) \frac{N_{\rm H_2}}{n_{\rm H_2}} \tag{5.6}$$

where the summation is made over the levels i (upper) and j (lower), the level populations n_i are the solution to the system (5.2), ν_{ij} the central frequency of the transition, $N_{\rm H_2}$ the H_2 column density along the emission path, and φ_{ij} the line profile resulting from the convolution of many effects including the instrumental response.

In Figure 5.2 we show infrared spectra normalized to their maximum values for increasing gas number densities, for the case of $T_k = 1000$ K and $\varsigma_{\rm H} = 1 \times 10^{-5}$ s^{-1}. Since the spectra are normalized, we are actually comparing spectral shapes. As it evident from the Figure, that with the exception of isolated pure rotational transitions with $\lambda \gtrsim 5$ μm, such as $(0-0)S(5)$, the infrared spectrum approaches the LTE shape for gas densities larger than $n_{\rm H} \approx 10^4$ cm^{-3}. XUV pumping can provide direct rotational excitations only to levels with $J \leq 3$. However, the XUV pumped spectra are much more intense than purely thermal spectra, unless the thermal pressure increases drastically (in that case we end up with the LTE case). It is also evident that ionization rate and density have different relative weights in driving level populations out and into the thermal regime.

We can summarize the current results as follows

(i) planetary densities are always such that the non thermal shape of XUV induced emission is lost;

(ii) up to densities $n_{\rm H} = 10^{10}$ cm^{-3} non-thermal effects dominate; such density limit applies as long as ionization rates are $\varsigma_{\rm H} \leq 10^{-5}$ s^{-1}; for higher ionization rates level population thermalization depends on the effective value of $\varsigma_{\rm H}$, and it may be much higher; spectra are however degenerate with the thermal case;

(iii) out-of-equilibrium spectra do not show the expected pure rotational line pattern;

(iv) the most favourable situations (as it was clear from the beginning) are those with high ionization rates and low densities; however an increase in both density and ionization rate drives level populations out of equilibrium; unfortunately while very high densities are not so peculiar, ionization rates cannot be increased boundlessly;

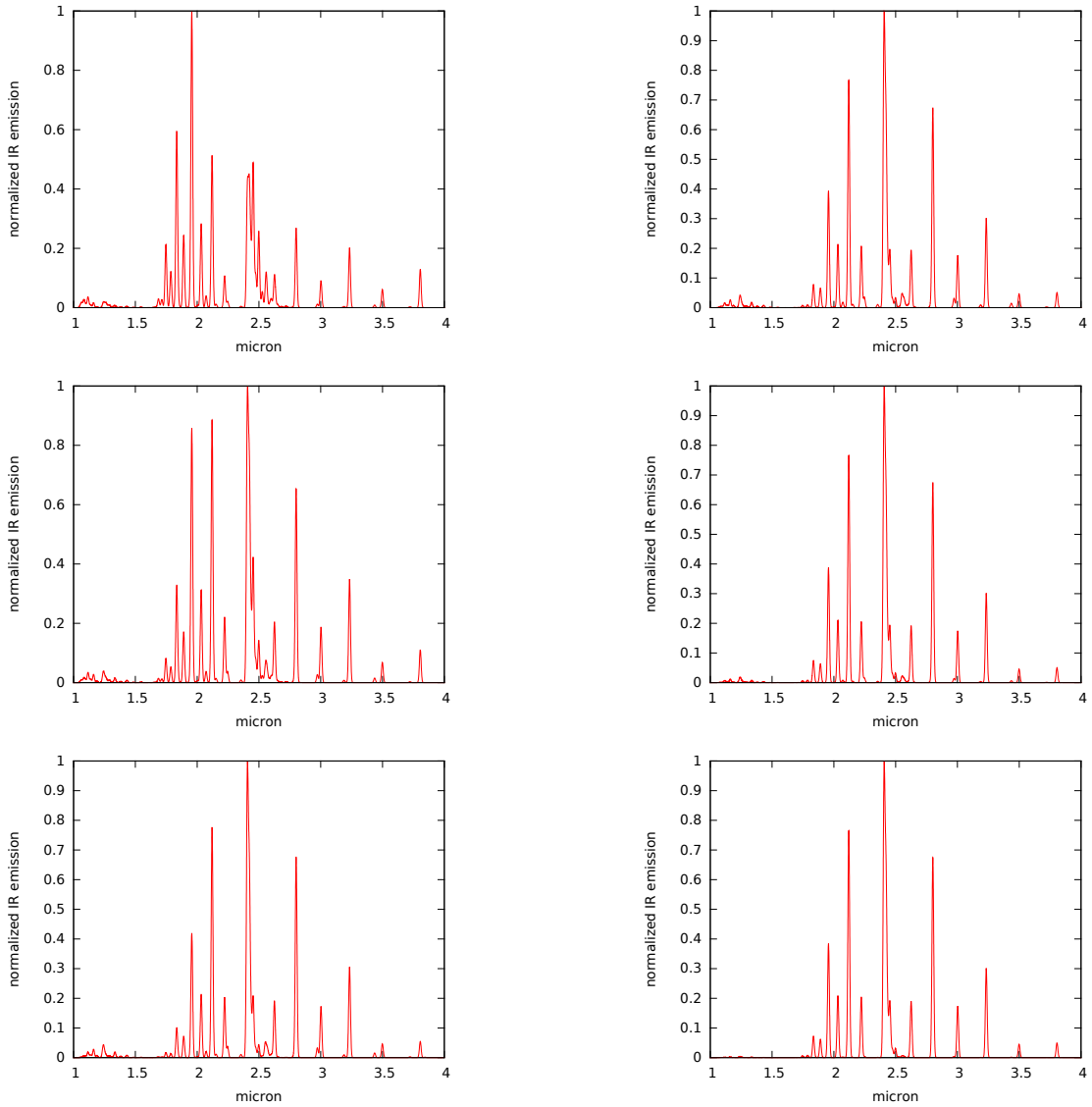

Figure 5.2: Emission spectra normalized to their maximum values as functions of the wavelength (in μm). Gas number density $n_{\rm H}$ (cm^{-3}): 10^2, left upper panel; 10^4, left middle panel; 10^6, left bottom panel; 10^8, right upper panel; 10^{10}, right middle panel; LTE, right bottom panel. The gas kinetic temperature is $T_k = 1,000$ K, while the ionization rate is $\varsigma_{\rm H} = 1 \times 10^{-5}$ s^{-1}. The convolved line shapes have width $\Delta\lambda = 0.01$ μm.

(v) the scenario depicted in item (iv) may be less pessimistic if we consider that close-in exoplanets are sometime terribly close-in; in that case the irradiation may be remarkably high, and so the ionization rate; moreover, since the atmospheres are very extended, pressures should be lower than for static atmospheres; on the other side, in these cases the use of low electron concentration should be justified, and so the excitation rates may be suffering a decrease of a factor 40 (see Table 5.1).

Finally, an interesting effect may be related to the presence of XUV excited H_2. From a visual inspection of the spectra reported in the Figures above, we may note the presence of a small band (at the level of 5 % of the maximum intensity) located between 1 and 1.5 μm. The position of this band falls in the spectral interval that Sing et al. (2016) used for their analysis of the water content in hot Jupiters, inferring the presence of hazes and clouds. This may be worthwhile of further investigation. To this aim, an additional water layer becomes crucial, and thus the calculation would require the incorporation of the transfer results discuss in Chapter 2.

5.5 The case of HD 189733b

We apply the model described above to the remarkable case of the hot Jupiter HD 189733b. HD 189733b is a giant exoplanet with mass and radius slightly greater than those of Jupiter ($M_{\rm p} = 1.142\,M_J$ and $R_{\rm p} = 1.138\,R_J$), discovered in the 2005 by Bouchy et al. (2005). The planet orbits at ~ 0.031 AU ($P = 2.2$ days) from the central star, HD 189733, a young star as old as 600 Myr, the spectral type is $K1-K2$ with an effective temperature of $T_{\rm eff} = 4875$ K. Its X-ray luminosity is $L_{\rm X} = 1.5 \times 10^{28}$ erg s^{-1} (Sanz-Forcada et al. 2010).

5.5.1 The model atmosphere

Because of the proximity of the parent star, we assume that the planetary atmosphere is inflated to fill the Roche lobe. Thus, we consider a stratified atmosphere with the geometry shown in Figure 5.3. We set the upper boundary layer at the Roche lobe radius $R_{\rm R}$, and the lower boundary layer at the planetary photospheric radius, $R_{\rm p}$, where the optical and infrared stellar photons are absorbed. The external gas envelope is supposed to be of solar composition. In this layer we assume that the radiation in the vacuum ultraviolet spectral range (essentially Lyman-α) is strongly attenuated, so that equation (5.2) is appropriate.

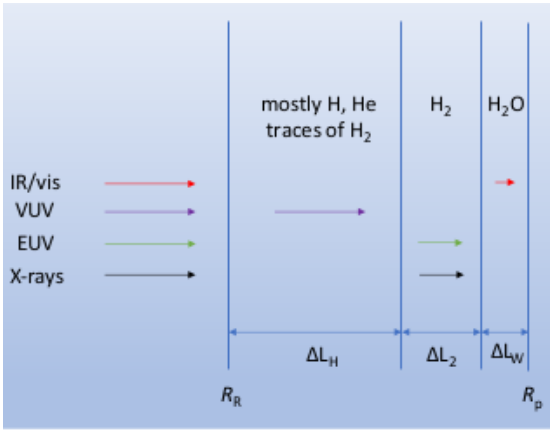

Figure 5.3: Model atmosphere extending from the Roche radius$R_{\rm R}$ to the photospheric radius$R_{\rm p}$. The extension of the external "atomic" layer is $\Delta {\rm L_H}$. The thickness of the H_2 layer is $\Delta {\rm L}_2$, while the additional water layer is $\Delta {\rm L_w}$ wide.

The lower layers are assumed to consist exclusively of molecular hydrogen, with a possible additional final layer of (dirty) water.

5.5.2 Infrared emission of H_2 from HD 189733b

We compute the X-ray induced infrared emission assuming an empty interplanetary medium: the high energy radiation propagates unabsorbed from the star to the Roche radius. Exploiting the theory described in chapter 3, we estimate the mean X-ray ionization rate $\langle \varsigma_H \rangle$ of the atmospheric gas inside the volume delimited by $R_{\rm R}$ and $R_{\rm p}$, with the further reasonable assumption that the photospheric radius is equal to the observed radius. In order to evaluate the size of the Roche lobe we use the approximated equation proposed by Eggleton (1983):

$$R_{\rm R} = d \frac{0.49 q^{2/3}}{0.69 q^{2/3} + \ln(1 + q^{1/3})} \tag{5.7}$$

where d is the distance between the planet and the star, q is the ratio between the mass of the planet and the mass of the star ($q = M_{\rm p}/M_\star$). In the case of HD 189733b, the Roche radius results $R_{\rm R} = 2.6 \times 10^{-3}$ AU. We calculate the emission infrared spectra for three values of the density of the extended atmosphere, 10^6, 10^8, and 10^{10} cm^{-3}. For the lowest value of the density, the emission intensity is negligible, while at highest values the emission spectra approach that of LTE (independently by whatever value of the X-ray ionization

Table 5.3: X-ray mean ionizations for HD 189733b

n_{H_2} (cm^{-3})	$\langle \varsigma_H \rangle$ (s^{-1})
10^6	$7 \cdot 10^{-6}$
10^8	$6.5 \cdot 10^{-6}$
10^{10}	$3.7 \cdot 10^{-7}$

rate). For each density of the gas, we calculate the correspondent value of the mean X-ray ionization $\langle \varsigma_H \rangle$ as reported in Table 5.3. Lecavelier Des Etangs et al. (2008) find that the atmospheric temperature of HD 189733b lies in the range $1340 - 1540$ K. We then perform our simulations for four values of the temperature, from 1250 to 1550 K in steps of 100 K, for a total of 12 models. We assume the thickness of the molecular layer to be $\Delta L_2 = f_2 \times R_{\rm R}$, where f_2 is the fractional H_2 path. We assume as conservative estimate $f_2 = 0.1$. Since $N_{H_2}/n_{H_2} = \Delta L_2 = f_2 \times R_{\rm R}$ the intensity of the emission scales linearly with f_2 (see equation 5.6).

In Figure 5.4 we present the infrared emission spectrum $\varepsilon_{\rm iR}(\nu)$ for some choice of the parameter set.

For the lowest density the emission spectra induced by X-rays are several order of magnitude greater than the LTE emission spectra, for the intermediate value of the density non-LTE spectra are still brighter than LTE spectra, but their intensities approach LTE for increasing temperatures. For instance, at $T_k = 1550$ K the intensity is just twice the LTE intensity, while it is brighter of about one order of magnitude for $T_k = 1250$. At the highest densities the spectra reach LTE for all the values of temperature. Morphological differences from the equilibrium spectra are present for gas densities $n_{\rm H} = 10^6$, and 10^8 cm^{-3}, in particular in the region $1 - 1.5$ μm and around 2.6 μm. Pure rotational lines appear as the density increases well below the critical density for thermalization (see Section 5.4).

5.6 Discussion

The results of the present modeling procedure, although still exploratory show that in close-in exoplanet atmospheres molecular hydrogen may be a diagnostics of stellar high energy emission. In the present chapter we limited our analysis to planetary configuration and geometry left purposely not detailed and averaged. Considering that under the action of the XUV radiation the atmosphere is dynamically expanding, it may be possible that a large fraction of the escaping gas is at much lower densities than that exploited in this work.

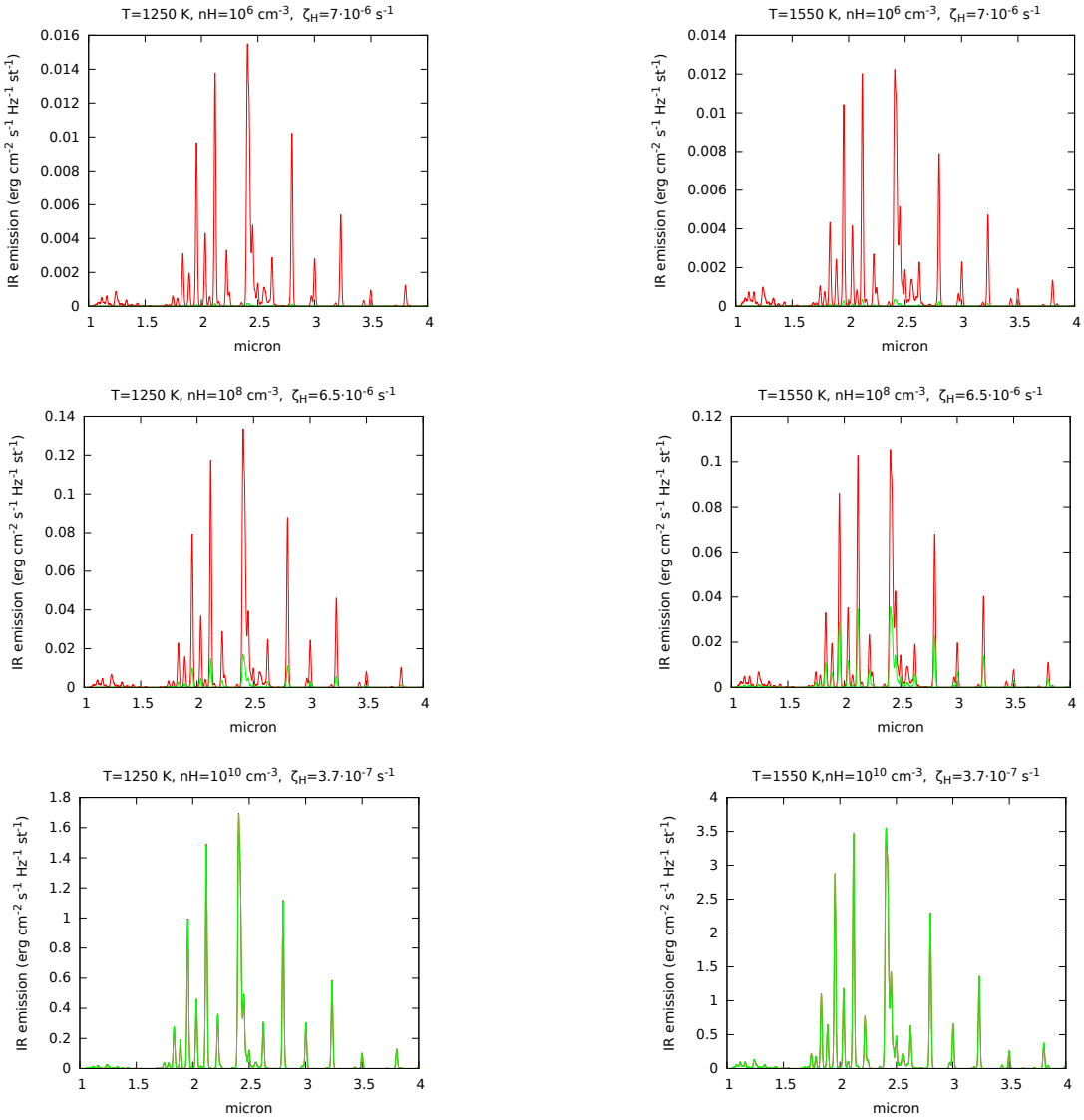

Figure 5.4: Infrared emission spectra of molecular hydrogen induced by XUV radiation (red line), and at thermal regime (green line) for some values of the atmospheric temperature, density and X-ray mean ionization rate (see labels in the panels).

In such a case the H_2 emission spectra may retain the characteristic features of the X-ray pumping excitation.Thus, even if the global integrated brightness is faint, some distinct spectral fingerprint at specific frequency may be exceeding largely the combined planet/star infrared background, and became detectable (at least as infrared excess). Further study are necessary, but the present results are encouraging since in a relevant part of the parameter space the H_2 non equilibrium emission is significantly beyond the thermal level.

Chapter 6

Final Remarks

6.1 Summary

The studies contained in this Thesis revolve around the effects induced by high energy photons of stellar origins, in the region surrounding the star, and beyond in the general interstellar medium. While the host star's optical and infrared radiation is the primary heat source for the surface and lower atmosphere of the exoplanet, shorter wavelength radiation is absorbed in the upper atmosphere where photochemistry and mass loss occurs. Therefore, the impact of high energy radiation on the atmospheric physics and chemistry must be studied in the context of the global irradiation of the atmosphere. For this reason, ancillary to the propagation of XUV radiation is the study of optical and infrared radiative transfer throughout a planet atmosphere. This constitutes the first, introductory work – presented in Chapter 2 – in which we couple a detailed 1D radiative transfer description with a radiative thermo-convective numerical code. 1D models are able to provide global averaged quantities such as the temperature and chemical profiles, although they fail in handling inherently multi-dimensional processes, such as clouds or local conditions at a given time. Nevertheless, they are excellent tools to explore exoplanetary climates (in average sense), and in the definition of the classical habitable zone. Moreover, 1D models are the natural starting point to explore a parameter space too broad for heavy 3D modeling.

The radiative transfer for XUV radiation is presented in Chapter 3, either theory and results of the model applied to parsec scales. A unique feature of X-ray irradiation is that all the relevant processes are dominated by secondary ionizations generated by primary photoelectrons. This is a consequence of the large primary photoelectron energies. Actually, the

secondary processes are far more important than the corresponding ionization, excitation, and dissociation events caused directly by X-rays. In the radiative transfer calculation we use up-to-date photoelectric cross-sections of atomic hydrogen, neutral and ionized helium, and molecular hydrogen. For heavy elements bound in molecules or molecular ions, the X-ray absorption cross-sections can be obtained approximately by adding the atomic cross-sections, for which we adopt relativistic photoionization cross-sections of individual heavy elements and their ions. Since, at high energies Compton ionization is more efficient than photoionization of H and He, we also include non-relativistic Compton ionization cross-sections for H, H_2, and He. Secondary processes are far more important than the corresponding ionization, excitation, and dissociation events caused directly by X-rays. The energy degradation is characterized by the mean energy per ion pair, which is the crucial quantity to be computed. We follow the chain of discrete electron energy deposition events using an accurate Monte Carlo method. As first application of the formalism it has been revisited the concept of Röntgen sphere, defined as the circumstellar regions in which the ionization rate due to X-rays exceeds the background level provided by cosmic rays. On these bases, we find that significant volumes of gas in nearby star-forming regions are affected by large ionization levels. In clusters arising in regions of vigorous star formation, X-rays create an ionization network pervading densely the interstellar medium. Such X-ray background radiation in young embedded clusters is potentially a key factor in star and planet formation, providing a natural feedback mechanism. Such scenario is not found within clusters, richer in massive stars, where the ultraviolet fields generated by such massive stars dominate over the X-ray contribution of lower mass stars.

In the final two chapters we studied the effects of X-ray irradiation on stellar scales. To this aim we explore two effects of the X-ray energy deposition on planetary atmospheres of close-in planets. For planets close enough to the host star, the atmosphere may go through a long phase of efficient hydrodynamic escape, or even bolw-off, which depending on the the planet's atmosphere mass, may or may not significantly affect the planet. In Chapter 4 we put forward a model simulating the thermal hydrodynamic escape of atmospheric gas induced by XUV radiation, that shapes the planetary envelope, setting it onto its final evolutionary path. To recover such a path, we may start from the current mass of the planet, and retrace its evolution back in time, obtaining the mass of the planet when the star was much younger, the so called planetary mass function. The model is based on the energy-limited approximation which provides a simple analytical description of the mass loss rate. We consider planets orbiting around dG and dM stars, but the final results

are weakly dependent on the stellar spectral type. Starting from the nowadays occurring frequency of planets, and using the derived planetary mass function as both prediction and correction factors, we derive the frequency of finding giant exoplanets around dG and dM stars. The impact of XUV induced photo-evaporation increases with decreasing mass of the planet. The observational estimate of the occurring frequency of planets around young stars might confirm the proposed planetary evolution, and therefore the role played by the radiation environments of the host stars. This is currently on going within the ground-based observational project GAPS2.

As a final application we discuss the potential observability of non-LTE effects in close-in exoplanets around stars emitting significant amount of X-ray radiation. Since the atmospheric composition of the Jupiter-like planets is dominated by hydrogen species, molecular hydrogen is probably the most abundant component in the upper atmosphere of these planets. From the study performed in Chapter 3, we learn that secondary electron non-thermal collisions with H_2 molecules result preferentially in the excitations to the rotational states $J = 2$ and 3, and the vibrational manifolds $v = 1$ and 2. This give rise to a characteristic spectrum at low density. This is a typical example of non LTE process, which depends critically by the number density of the gas. Unfortunately, the critical densities for such a process are too low in comparison to the ones characteristic of a planetary atmosphere, even at high altitudes. This means that spectral shapes, and thus typical line ratios cannot give useful information, removing the possibility to perform relative measurements. However, we find that X-rays produce excitation temperatures for the relevant lines in large excess of the inferred temperature of the planet. We apply this analysis to the planet HD 189733b. The results of the present modeling procedure show that molecular hydrogen may be a diagnostics of stellar high energy emission, because in a relevant part of the parameter space the H_2 non equilibrium emission is significantly beyond the thermal level.

6.2 Future developments

As future step we will supplement the radiative transfer code coupled with the described radiative thermo-convective technique with a chemical model. The solutions to these problems, either separately or coupled, describe the thermal balance and pressure profiles within the atmosphere, kinetics, photolysis, vertical mixing and molecular diffusion, leading to an accurate simulation of the atmospheric chemistry. Photodissociations and ionization by the stellar high energy radiation component, and transport/mixing resulting from the dynamics

powered by the intense irradiation, occur on timescales comparable or even shorter than the chemical timescales. Hot/warm planetary atmospheres are thus out of equilibrium systems, in which thermochemistry competes with photolysis and gas dynamics. Modelling of atmospheric chemistry requires the use of a kinetic model, including all relevant individual chemical and photochemical processes, coupled with a detailed radiative transport description. This model naturally evolves towards the thermochemical equilibrium when photolysis and transport decline. Dynamics play a crucial role in redistributing the heat (e.g., from the day to the night side in tidally locked planets) and to homogenize the chemical composition among the different regions of the atmosphere. These effects mark the transitions between 1D and multidimensional (climate) models.

Appendix A

Physical units in this Thesis

It may be useful to clarify the physical units used in this thesis. While most of scientists stick to SI units, astronomers are more relaxed as they use whatever units seem to be convenient. For example, in order to indicate the number density of particles in the interstellar medium, they will express it in cm^{-3} instead that m^{-3}. The reason relies in the fact that the average number density of hydrogen atoms in our Galaxy is about one particle per cubic centimeter, much less cumbersome that to write one million particles per cubic meter. While there is little justification for that, a bit more appropriate is the use of several distance units, as space distances run from planetary scales (thousand of kilometers), through interplanetary scales (Astronomical Units), to interstellar distances (parsec or light year). Another important case regards energy units, that may be expressed alternatively in Joule, Erg, Electron Volt, inverse centimeter or micron, and kelvin. The passage to standards is even slower for wavelengths, and you may find, where appropriate units such as nanometers, microns, millimeters, centimeters, meters, and kilometers. At the same time, in the astronomical literature can be easily found Ångströms. You will never find the hydrogen Lymanα wavelength expressed as 1.215×10^{-7} m instead of the traditional 1215 Å. Planetary and stellar properties (e.g. mass and radius of a planet, or luminosity of a star) are often expressed in terms of the properties of the Earth or Jupiter for planets, and those of the Sun for stars.

Table A.1: Physical units

Physical Quantity	Units used in this Thesis	Symbol	S.I. value
Distance	Parsec	pc	3.086×10^{16} m
Distance	Light Year	l.y.	9.461×10^{15} m
Distance	Astronomical Unit	AU	1.496×10^{11} m
Energy	Electron Volt	eV	1.6022×10^{-19} J
Energy	Kelvin	K	1.38065×10^{-23} J
Energy	inverse centimeter	cm^{-1}	2.0544×10^{-23} J
Stellar mass	Sun mass	$M_\odot$	1.989×10^{30} kg
Stellar radius	Sun radius	$R_\odot$	6.957×10^{8} m
Stellar luminosity	Sun Luminosity	$L_\odot$	3.839×10^{26} W
Planetary mass	Earth mass	$M_\oplus$	5.972×10^{24} kg
Planetary radius	Earth radius	$R_\oplus$	6.371×10^{6} m
Planetary mass	Jupiter mass	M_J	1.898×10^{27} kg
Planetary radius	Jupiter radius	R_J	6.9911×10^{7} m

Appendix B

Discrete ordinate method

In equation (2.1) the source function $S_\nu(\tau_\nu, \mu, \phi)$ is given by the following expression:

$$S_\nu(\tau_\nu, \mu, \phi) = \frac{\omega_\nu}{4\pi} \int_0^{2\pi} d\phi' \int_{-1}^{+1} d\mu' P_\nu(\tau_\nu, \mu, \phi; \mu', \phi') \times I_\nu(\tau_\nu, \mu', \phi') + Q_\nu(\tau_\nu, \mu, \phi) \quad \text{(B.1)}$$

where ω_ν is the single scattering albedo, $P_\nu(\tau_\nu, \mu, \phi; \mu', \phi')$ is the phase function normalized over the solid angle, that represents the probability that a wave incoming in the direction (μ, ϕ) will be scattered in the direction (μ', ϕ'), while Q_ν is the is the actual internal source. At the lower atmosphere in condition of local thermodynamic equilibrium (LTE) the therm Q_ν become:

$$Q_\nu^{\text{th}}(\tau_\nu) = [1 - \omega_\nu(\tau_\nu)] \times B_\nu[T(\tau_\nu)] \quad \text{(B.2)}$$

with $B_\nu(T)$ Planck function at the frequency a ν and at the temperature T. Now if we separate for the direct radiation an for the diffuse radiation so that the term $I_\nu(\tau_\nu, \mu, \phi)$ in the equations (2.1) and (B.1) describes only the diffuse radiation, then into a non emitting medium for a incident ray at the direction (μ_0, ϕ_0) we obtain:

$$Q_\nu^\star(\tau, \mu, \phi) = \frac{\omega_\nu(\tau) I_0}{4\pi} P_\nu(\tau_\nu, \mu, \phi; -\mu_0, \phi_0) \exp\left(-\tau_\nu/\mu_0\right) \quad \text{(B.3)}$$

where $\mu_0 I_0$ is the incident flux. Then we can define the emissivity as follows:

$$Q_\nu(\tau_\nu, \mu, \phi) = Q_\nu^{\text{th}}(\tau_\nu) + Q_\nu^\star(\tau, \mu, \phi). \quad \text{(B.4)}$$

The solution of the problem of the radiative transfer is found by means expanding the

phase function in a series of $2 \cdot N$ Legendre polynomials and the intensity in a Fourier series:

$$I(\tau, \mu, \phi) = \sum_{m=0}^{2\times N-1} I^m(\tau, \mu) cos\, m\,(\phi_0 - \phi) \tag{B.5}$$

where for simplicity we have dropped the index that refer to the frequency. Follows that the equations (2.1) and (B.1) are replaced by a set of $2 \cdot N$ equations, one for each Fourier component (Chandrasekhar 1960):

$$\mu \frac{dI^m(\tau, \mu)}{d\tau} = I^m_\nu(\tau, \mu) - \int_{-1}^{+1} D^m(\tau, \mu, \mu') I^m(\tau, \mu') d\mu' - Q^m(\tau, \mu) \tag{B.6}$$

with $m = 0, 1, 2, \cdots, 2 \times N - 1)$, where

$$\begin{aligned} D^m(\tau, \mu, \mu') &= \frac{\omega(\tau)}{2} \sum\nolimits_{l=m}^{2\times N-1} g^m_l(\tau) p^m_l(\mu) p^m_l(\mu') \\ Q^m(\tau, \mu) &= X^m_0(\tau, \mu) \exp\left(-\tau/\mu_0\right) + \delta_{m0} Q^{\text{th}}(\tau) \\ X^m_0(\tau, \mu) &= \frac{\omega(\tau) I_0}{4\pi} \left(2 - \delta_{m0}\right) \sum\nolimits_{l=0}^{2\times N-1} (-1)^{l+m} \left(2l + 1\right) g^m_l(\tau) p^m_l(\mu) p^m_l(\mu_0) \\ g_l(\tau) &= \tfrac{1}{2} \textstyle\int_{-1}^{+1} p_l(\overline{\mu}) P(\tau, \overline{\mu}) d\overline{\mu}. \end{aligned} \tag{B.7}$$

In the equations (B.7) $\delta_{m0} = 1$ if $m = 0$, zero otherwise, p_l is the Legendre polynomial of order l, p^m_l is the associate Legendre polynomial and $\overline{\mu}$ is the cosine of the scattering angle (i.g. the angle between the direction of incidence and diffusion). The functions g_l are the moments of the phase function, the term g_0 is normalized to the unity while the term g_1 is the so called asymmetry factor and is zero for the isotropic radiation. In this way the equation can be solved through the discrete ordinate method and wrote as follows:

$$\mu_i \frac{dI^m(\tau, \mu_i)}{d\tau} = I^m_\nu(\tau, \mu_i) - \sum\nolimits_{j=-N}^{+N} w_j D^m(\tau, \mu_i, \mu_j) \times I^m(\tau, \mu_j) - Q^m(\tau, \mu_i) \tag{B.8}$$

the terms $j = 0$, e $m = \pm 1, \pm 2, \cdots, \pm N$ are excluded from the summatory, μ_i and w_i are the quadrature points and the weights respectively.

Appendix C

Collision Induced Absorption

Collision Induced Absorption (CIA) refers to events following incoherent collisions between two or more molecules giving rise to characteristic absorption features. CIA become important in dense gases such as planetary atmospheres. CIA spectra involve electric or magnetic multipole moments. CO_2 molecules do not possess a permanent dipole moment, so that they are infrared inactive. However, due to their relatively large quadrupole moment and polarizability, self-collisions induce a temporary dipole moment. Such momentum is responsible for far-infrared roto-translational absorptions (Gruszka & Borysow 1997). At low densities, where collision are mostly binary, CIA intensity is proportional to the square density, while at higher densities when ternary (or more) collisions are more frequent, the intensity depends to higher powers of density. Molecules such as N_2,O_2, H_2 and CO2 can show strong absorption band due to CIA. In Figure C.1 are drawn the absorption features due to CIA for several temperatures in the spectral range $10 - 300$ cm$^-$1 and $1100 - 2000$ cm$^-$1.

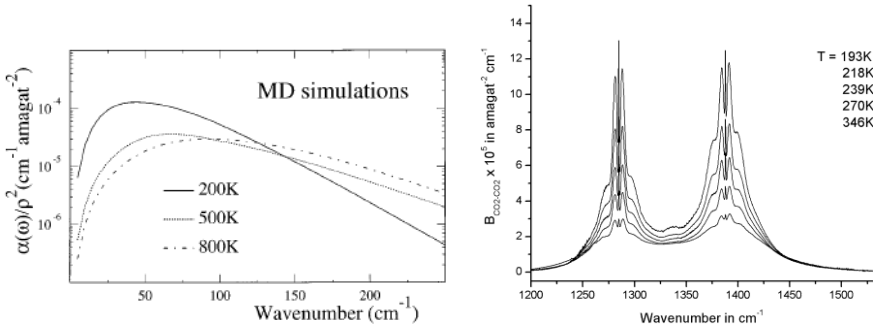

Figure C.1: CIA spectra computed at different temperatures in the region $10 - 300$ cm$^-$1 (Gruszka & Borysow 1997, left panel), and $1100 - 2000$ cm$^-$1 (Baranov et al. 2004, right panel

Appendix D

van Vleck-Wisskopf profile

he Van Vleck-Weisskopf profile is an approximate line shape in case of the pressure broadening. This approximation is valid if the time between collision is longer then the duration of the collisions. Collisions must be strong enough to change randomly the orientation of the dipole moment of the molecule, and weak enough to induce only linear deformations, and that the involved energy levels are sufficiently isolated. The van Vleck-Weisskopf line shape profile is given by the following expression:

$$f_L(\nu - \nu_0) = \left(\frac{\nu}{\nu_0}\right)^2 \left\{ \frac{1}{\pi} \frac{\alpha_L}{(\nu - \nu_0)^2 + \alpha_L^2} + \frac{1}{\pi} \frac{\alpha_L}{(\nu + \nu_0)^2 + \alpha_L^2} \right\} \tag{D.1}$$

where α_L is the width of the pure Lorentzian profile, and is defined by equation (2.8), ν_0 is the central frequency of the transition. The Van Vleck-Weisskopf profile tends asymptotically to a Lorentz profile towards high frequency.

Bibliography

Ádámkovics, M., Glassgold, A. E., & Meijerink, R. 2011, ApJ, 736, 143

Adams, F. C., Fatuzzo, M., & Holden, L. 2012, PASP, 124, 913

Albacete Colombo, J. F., Flaccomio, E., Micela, G., Sciortino, S., & Damiani, F. 2007, A&A, 464, 211

Anchordoqui, L. A., Beacom, J. F., Goldberg, H., Palomares-Ruiz, S., & Weiler, T. J. 2007, Phys. Rev. D, 75, 063001

Anglada-Escudé, G., Amado, P. J., Barnes, J., et al. 2016, Nature, 536, 437

Asplund, M., Grevesse, N., Sauval, A. J., & Scott, P. 2009, ARA&A, 47, 481

Bahcall, J. N., Bahcall, N. A., & Kozlovsky, B.-Z. 1971, A&A, 13, 1

Baranov, Y. I., Lafferty, W. J., & Fraser, G. T. 2004, J. Mol. Spec, 228, 432

Bartlett, P. L. & Stelbovics, A. T. 2004, At. Data Nucl. Data Tables

Batalha, N. M., Rowe, J. F., Bryson, S. T., et al. 2013, VizieR Online Data Catalog, 220

Bolmont, E., Raymond, S. N., Leconte, J., Hersant, F., & Correia, A. C. M. 2015, VizieR Online Data Catalog, 358

Bouchy, F., Udry, S., Mayor, M., et al. 2005, A&A, 444, L15

Bozza, V., Mancini, L., & Sozzetti, A., eds. 2016, Astrophysics and Space Science Library, Vol. 428, Methods of Detecting Exoplanets

Bradford, C. M., Bolatto, A. D., Maloney, P. R., et al. 2011, ApJ, 741, L37

Brogi, M., de Kok, R. J., Birkby, J. L., Schwarz, H., & Snellen, I. A. G. 2014, A&A, 565, A124

Brown, R. A. 2014, ApJ, 788, 192

Bruno, G., Lewis, N. K., Stevenson, K., et al. 2017, in American Astronomical Society Meeting Abstracts, Vol. 230, American Astronomical Society Meeting Abstracts, 402.02

Burch, D. E., Gryvnak, D. A., Patty, R. R., & Bartky, C. E. 1969, JOSA, 59, 267

Burrows, A., Guillot, T., Hubbard, W. B., et al. 2000, ApJ, 534, L97

Burrows, A., Hubbard, W. B., Saumon, D., & Lunine, J. I. 1993, ApJ, 406, 158

Burrows, A., Marley, M., Hubbard, W. B., et al. 1997, ApJ, 491, 856

Carson, J., Thalmann, C., Janson, M., et al. 2013, ApJ, 763, L32

Cecchi-Pestellini, C., Cacciola, A., Iatì, M. A., et al. 2010, MNRAS, 408, 535

Cecchi-Pestellini, C., Casu, S., & Dalgarno, A. 2005, MNRAS, 364, 1309

Cecchi-Pestellini, C., Ciaravella, A., & Micela, G. 2006, A&A, 458, L13

Cecchi-Pestellini, C., Ciaravella, A., Micela, G., & Penz, T. 2009, A&A, 496, 863

Chandrasekhar, S. 1960, Radiative transfer

Ciaravella, A., Chen, Y.-J., Cecchi-Pestellini, C., et al. 2016, ApJ, 819, 38

Cravens, T. E., Victor, G. A., & Dalgarno, A. 1975, Planet. Space Sci., 23, 1059

Crossfield, I. J. M. 2015, PASP, 127, 941

Dale, J. E. & Bonnell, I. 2011, MNRAS, 414, 321

Dalgarno, A., Yan, M., & Liu, W. 1999, ApJS, 125, 237

D'Angelo, G., Kley, W., & Henning, T. 2003, ApJ, 586, 540

Donati, J.-F., Yu, L., Moutou, C., et al. 2017, MNRAS, 465, 3343

Downes, D. & Rinehart, R. 1966, ApJ, 144, 937

Draine, B. T. 2003, ARA&A, 41, 241

Drew, J. E., Barlow, M. J., Unruh, Y. C., et al. 2004, MNRAS, 351, 206

Drew, J. E., Greimel, R., Irwin, M. J., & Sale, S. E. 2008, MNRAS, 386, 1761

Driscoll, P. E. & Barnes, R. 2015, Astrobiology, 15, 739

Eggleton, P. P. 1983, ApJ, 268, 368

Elkins-Tanton, L. T. & Seager, S. 2008, ApJ, 685, 1237

Erkaev, N. V., Kulikov, Y. N., Lammer, H., et al. 2007, A&A, 472, 329

Fatuzzo, M. & Adams, F. C. 2008, ApJ, 675, 1361

Favata, F., Flaccomio, E., Reale, F., et al. 2005, ApJS, 160, 469

Favata, F. & Micela, G. 2003, Space Sci. Rev., 108, 577

Feigelson, E. D. 2010, Proceedings of the National Academy of Science, 107, 7153

Feigelson, E. D. & Montmerle, T. 1999, ARA&A, 37, 363

Forget, F. & Leconte, J. 2014, Philosophical Transactions of the Royal Society of London Series A, 372, 20130084

Fressin, F., Torres, G., Charbonneau, D., et al. 2013, ApJ, 766, 81

Fu, Q. & Liou, K. N. 1992, Sci., 49, 2139

Galli, D. & Padovani, M. 2015, ArXiv e-prints

Gaudi, B. S., Stassun, K. G., Collins, K. A., et al. 2017, Nature, 546, 514

Getman, K. V., Flaccomio, E., Broos, P. S., et al. 2005, ApJS, 160, 319

Giacconi, R., Murray, S., Gursky, H., et al. 1972, ApJ, 178, 281

Godolt, M., Grenfell, J. L., Kitzmann, D., et al. 2016, A&A, 592, A36

Gredel, R., Black, J. H., & Yan, M. 2001, A&A, 375, 553

Gredel, R. & Dalgarno, A. 1995, ApJ, 446, 852

Gruszka, M. & Borysow, A. 1997, Icarus, 129, 172

Guarcello, M. G., Drake, J. J., Wright, N. J., et al. 2013, ApJ, 773, 135

Gudennavar, S. B., Bubbly, S. G., Preethi, K., & Murthy, J. 2012, ApJS, 199, 8

Halevy, I., Pierrehumbert, R. T., & Schrag, D. P. 2009, J. Geophys. Res., 114, D18112

Hamaguchi, K., Corcoran, M. F., Russell, C. M. P., et al. 2014, ApJ, 784, 125

Hasegawa, Y. & Ida, S. 2013, ApJ, 774, 146

Heng, K. & Showman, A. P. 2015, Annual Review of Earth and Planetary Sciences, 43, 509

Holden, L., Landis, E., Spitzig, J., & Adams, F. C. 2011, PASP, 123, 14

Holland, H. D. 2002, Geochim. Cosmochim. Acta, 66, 3811

Hollenbach, D. & Gorti, U. 2009, ApJ, 703, 1203

Hu, Y. & Ding, F. 2011, A&A, 526, A135

Hudson, J. E., Vallance, C., & Harland, P. W. 2004, JPhB

Hummer, D. G. & Seaton, M. J. 1963, MNRAS, 125, 437

Islam, F., Cecchi-Pestellini, C., Viti, S., & Casu, S. 2010, ApJ, 725, 1111

Jackson, J. D. 1975, Classical electrodynamics

Jiménez-Escobar, A., Chen, Y.-J., Ciaravella, A., et al. 2016, ApJ, 820, 25

Kalas, P., Fitzgerald, M. P., Clampin, M., et al. 2009, in Bulletin of the American Astronomical Society, Vol. 41, American Astronomical Society Meeting Abstracts #213, 491

Kasting, J. F., Whitmire, D. P., & Reynolds, R. T. 1993, Icarus, 101, 108

King, R. R., Parker, R. J., Patience, J., & Goodwin, S. P. 2012, MNRAS, 421, 2025

Kley, W. & Nelson, R. P. 2012, ARA&A, 50, 211

Knödlseder, J. 2000, A&A, 360, 539

Kopparapu, R. K., Ramirez, R., Kasting, J. F., et al. 2013, ApJ, 765, 131

Kovacs, I. 1969, Rotational structure in the spectra of diatomic molecules.

Lacis, A. A. 2012

Lacis, A. A. & Oinas, V. 1991, J. Geophys. Res., 96, 9027

Lagrange, A.-M., Gratadour, D., Chauvin, G., et al. 2009, A&A, 493, L21

Lammer, H. 2013, Origin and Evolution of Planetary Atmospheres

Lammer, H., Selsis, F., Ribas, I., et al. 2003, ApJ, 598, L121

Lecavelier Des Etangs, A. 2007, A&A, 461, 1185

Lecavelier Des Etangs, A., Pont, F., Vidal-Madjar, A., & Sing, D. 2008, A&A, 481, L83

Liou, K. N. 1980, An introduction to atmospheric radiation.

Lissauer, J. J., Fabrycky, D. C., Ford, E. B., et al. 2011, Nature, 470, 53

Locci, D., Cecchi-Pestellini, C., Micela, G., Ciaravella, A., & Aresu, G. 2018, MNRAS, 473, 447

Lorenzani, A. & Palla, F. 2001, in Astronomical Society of the Pacific Conference Series, Vol. 243, From Darkness to Light: Origin and Evolution of Young Stellar Clusters, ed. T. Montmerle & P. André, 745

Madhusudhan, N., Bitsch, B., Johansen, A., & Eriksson, L. 2017, MNRAS, 469, 4102

Madhusudhan, N., Knutson, H., Fortney, J. J., & Barman, T. 2014, Protostars and Planets VI, 739

Maloney, P. R., Hollenbach, D. J., & Tielens, A. G. G. M. 1996, ApJ, 466, 561

Manabe, S. & Wetherald, R. T. 1967, J. Atmos. Sci, 24, 241

Mayor, M. & Queloz, D. 1995, Nature, 378, 355

Micela, G. 2001, in Astronomical Society of the Pacific Conference Series, Vol. 234, X-ray Astronomy 2000, ed. R. Giacconi, S. Serio, & L. Stella, 143

Micela, G. 2002, in Astronomical Society of the Pacific Conference Series, Vol. 269, The Evolving Sun and its Influence on Planetary Environments, ed. B. Montesinos, A. Gimenez, & E. F. Guinan, 107

Mihalas, D. & Binney, J. 1981, Galactic astronomy: Structure and kinematics /2nd edition/

Mischna, M. A., Lee, C., & Richardson, M. 2012, Journal of Geophysical Research (Planets), 117, E10009

Mlawer, E., Payne, V., Moncet, J. L., et al. 2012, Phil. Trans. R. Soc., 370, 2520

Morita, M. & Yabushita, S. 2008, J. Comp. Chem.

Moses, J. I., Madhusudhan, N., Visscher, C., & Freedman, R. S. 2013, ApJ, 763, 25

Murray, C. D. & Dermott, S. F. 2000, Solar System Dynamics

Nomura, H., Aikawa, Y., Tsujimoto, M., Nakagawa, Y., & Millar, T. J. 2007, ApJ, 661, 334

Osterbrock, D. E. & Ferland, G. J. 2006, Astrophysics of gaseous nebulae and active galactic nuclei

Owen, J. E. & Mohanty, S. 2016, MNRAS, 459, 4088

Palla, F. & Stahler, S. W. 1999, ApJ, 525, 772

Pallé, E., Zapatero Osorio, M. R., Barrena, R., Montañés-Rodríguez, P., & Martín, E. L. 2009, Nature, 459, 814

Penz, T. & Micela, G. 2008, A&A, 479, 579

Penz, T., Micela, G., & Lammer, H. 2008, A&A, 477, 309

Pepe, F. A. & Lovis, C. 2008, Physica Scripta Volume T, 130, 014007

Perrin, M. Y. & Hartmann, J. M. 1989, J. Quant. Spec. Radiat. Transf., 42, 311

Pierrehumbert, R. & Gaidos, E. 2011, ApJ, 734, L13

Preibisch, T. & Feigelson, E. D. 2005, ApJS, 160, 390

Preibisch, T., Kim, Y.-C., Favata, F., et al. 2005, ApJS, 160, 401

Preibisch, T. & Zinnecker, H. 1999, AJ, 117, 2381

Raymond, J. C. & Smith, B. W. 1977, ApJS, 35, 419

Ribas, I., Guinan, E. F., Güdel, M., & Audard, M. 2005, ApJ, 622, 680

Ricchiazzi, P., Yang, S., Gautier, C., & Sowle, D. 1998, Bull. A. Met. Soc., 79, 2101

Rogers, L. A. & Seager, S. 2010, ApJ, 716, 1208

Rothman, L. S. & et al. 2013, J. Quant. Spec. Radiat. Transf., 130, 4

Rybicki, G. B. & Lightman, A. P. 1985, Radiative processes in astrophysics.

Samson, J. A. R. & Haddad, G. N. 1994, JOSA B

Sanz-Forcada, J., Micela, G., Ribas, I., et al. 2011, A&A, 532, A6

Sanz-Forcada, J., Ribas, I., Micela, G., et al. 2010, A&A, 511, L8

Schröter, S., Czesla, S., Wolter, U., et al. 2011, A&A, 532, A3

Seager, S. 2009, Is There Life Out There?

Seager, S. 2010, Exoplanet Atmospheres: Physical Processes

Seager, S. 2013, Science, 340, 577

Seager, S., Kuchner, M., Hier-Majumder, C. A., & Militzer, B. 2007, ApJ, 669, 1279

Shematovich, V. I., Ionov, D. E., & Lammer, H. 2014, A&A, 571, A94

Sing, D. K., Fortney, J. J., Nikolov, N., et al. 2016, Nature, 529, 59

Smith, D. S., Scalo, J., & Wheeler, J. C. 2004, Origins of Life and Evolution of the Biosphere, 34, 513

Snellen, I. A. G., de Kok, R. J., de Mooij, E. J. W., & Albrecht, S. 2010, Nature, 465, 1049

Stamnes, K., Tsay, S.-C., Jayaweera, K., & Wiscombe, W. 1988, Appl. Opt., 27, 2502

Tanaka, H., Takeuchi, T., & Ward, W. R. 2002, ApJ, 565, 1257

Tarawa, H. & Kato, T. 1987, At. Data Nucl. Data Tables

Tarter, C. B. & Salpeter, E. E. 1969, ApJ, 156, 953

Tarter, C. B., Tucker, W. H., & Salpeter, E. E. 1969, ApJ, 156, 943

Thorne, A., Litzen, U., Johansson, S., & Mewe, R. 1999, Space Sci. Rev., 90, 525

Tielens, A. G. G. M. 2005, The Physics and Chemistry of the Interstellar Medium

Tielens, A. G. G. M. & de Jong, T. 1979, A&A, 75, 326

Tiné, S., Lepp, S., Gredel, R., & Dalgarno, A. 1997, ApJ, 481, 282

Toon, O. B., McKay, C. P., Ackerman, T. P., & Santhanam, K. 1989, J. Geophys. Res., 94, 16287

Tramper, F., Straal, S. M., Sanyal, D., et al. 2015, A&A, 581, A110

Tremblin, P., Audit, E., Minier, V., Schmidt, W., & Schneider, N. 2012, A&A, 546, A33

van Vleck, J. & Huber, D. L. 1977, Rev. Mod. Phys, 49, 939

Verner, D. A. & Yakovlev, D. G. 1995, A&AS, 109, 125

Vidal-Madjar, A., Lecavelier des Etangs, A., Désert, J.-M., et al. 2003, Nature, 422, 143

von Paris, P., Gebauer, S., Godolt, M., et al. 2010, A&A, 522, A23

Wang, Q. D. & lim, S. 2016, in American Astronomical Society Meeting Abstracts, Vol. 227, American Astronomical Society Meeting Abstracts, 323.06

Watson, A. J., Donahue, T. M., & Walker, J. C. G. 1981, Icarus, 48, 150

Wells, R. J. 1999, J. Quant. Spec. Radiat. Transf., 62, 29

Williams, D. A. & Viti, S. 2014, Observational Molecular Astronomy

Wolniewicz, L., Simbotin, I., & Dalgarno, A. 1998, ApJS, 115, 293

Wolszczan, A. & Frail, D. A. 1992, Nature, 355, 145

Wordsworth, R. & Pierrehumbert, R. 2014, ApJ, 785, L20

Wordsworth, R. D., Forget, F., Selsis, F., et al. 2010, A&A, 522, A22

Wright, N. J., Drake, J. J., Guarcello, M. G., et al. 2014, ArXiv e-prints

Wright, N. J., Drew, J. E., & Mohr-Smith, M. 2015a, MNRAS, 449, 741

Wright, N. J., Drew, J. E., & Mohr-Smith, M. 2015b, MNRAS, 449, 741

Yan, M., Sadeghpour, H. R., & Dalgarno, A. 1998, ApJ, 496, 1044

Yang, M., Xie, J.-W., Zhou, J.-L., Liu, H.-G., & Zhang, H. 2016, ApJ, 833, 7